Flame Propagation in Complex Geometries

Dissertation
zur Erlangung des akademischen Grades

**Doktoringenieur
(Dr.-Ing.)**

von M.Sc. Vitor Gabriel Silva
geb. am 11.06.1987 in Nova Iguacu - Brasilien

genehmigt durch die Fakultaet fuer Verfahrens- und Systemtechnik
der Otto-von-Guericke-Universitaet Magdeburg

Promotionskomission: Prof. Dr.-Ing. Eckehard Specht (Vorsitz)
Prof. Dr.-Ing. habil. Ulrich Krause (Gutachter)
Prof. Dr.-Ing. Filip Verplaetsen (Gutachter)
Prof. Dr.-Ing. Kai Holtappels (Gutachter)

eingereicht am: 03.08.2019
Promotionskolloquium am: 06.02.2020

Abstract

The study of premixed flames is vital for process engineering, especially present in scenarios such as fuel gas leaks from accidents as well as engine explosions in cars or turbines. The understanding and therefore the control of the phenomenon has increased in the last years due to improvements in computer calculation capacities and the measure gauges. Nevertheless, major challenges remain in the description and preview of this topic, particularly for complex scenarios. The aim of this work is the experimental and numerical investigation of premixed flame propagation in small scale complex geometries.

The experiments consist of an explosion and flame propagation of premixed flames. T-Pipes with and without obstacles are used to represent complex geometries. The flame propagation is monitored with a high-speed camera in the bent region of the T-Pipes. The pressure is measured during the flame propagation. The images from the high-speed camera are analyzed using image processing techniques. The flame behavior as well the flame front, the region behind the flame front, the flame shape, the flame speed average, the near-wall interactions, the turbulent vortexes, and the flame instabilities are analyzed. The aim is to research the impact of a bent region in premixed flame propagation.

The numerical flame investigation is based on computational fluid dynamic simulations. These simulations use a combustion model that reproduces an explosion and flame propagation. Computational Fluid Dynamics (CFD) simulations are performed to investigate an equivalent scenario like the experimental one. Homogeneous and inhomogeneous mixtures with different boundary conditions in the outlet region of the T-Pipes are simulated. The combustion model and the governing equations implemented in the CFD software are presented in detail. The purpose is to reproduce and understand in details the phenomenon observed in the experiments.

Accordingly, the experimental and numerical simulation results are compared to analyze flame propagation in detail. As a result of the numerical and experimental investigation, other stages of flame propagation based on the investigation of the flame front and the region behind the flame front are proposed. The impact of a bent region in flame propagation for lean, stoichiometric, and rich inhomogeneous premixed methane-air is investigated in detail.

Zusammenfassung

Vorgemischte Flammen sind wichtige Forschungsaspekte innerhalb der Verfahrenstechnik, die vor allem bei der Untersuchung unfallbedingter Gaslecks, sowie bei Verbrennungsmotoren in Autos und Turbinen relevant sind. Infolge von Kapazitätssteigerungen computerbasierter Kalkulationen und Verbesserungen der Messgeräte wuchs in den letzten Jahren das Verständnis und die Kontrolle des Phänomens. Dennoch bestehen weiterhin große Herausforderungen in der Beschreibung und Vorhersage, speziell im Bereich komplexer Szenarien. Ziel dieser Arbeit ist daher die experimentelle und numerische Untersuchung einer vorgemischten Flammenausbreitung in komplexen Szenarios im kleinen Maßstab.

Bei den Experimenten steht die Untersuchung von Explosion und Flammenausbreitung von mager vorgemischten Flammen im Fokus. Im Vorfeld des Experiments hergestellte Luft-Methan-Gemische werden in komplexen Geometrien untersucht. T förmige Rohre mit und ohne Hindernisse werden verwendet um komplexe Geometrien zu imitieren. Die Flammenausbreitung wird mit einer Hochgeschwindigkeitskamera im gebogenen Abschnitt des T-Rohrs aufgezeichnet.

Während der Flammenausbreitung wird der Druck gemessen. Die Bilder der Hochgeschwindigkeitskamera werden unter Vewendung von Bildverarbeitungstechniken ausgewertet. Außerdem werden Flammenverhalten, Flammenfront, Form, Geschwindigkeitsmittelwert, Flamme-Wand-Interaktionen, sowie turbulente Wirbel und Flammeninstabilitäten analysiert.

Die numerische Flammenuntersuchung basiert auf numerischen Strömungssimulationen. Diese Simulationen beruhen auf einem Verbrennungsmodell, welches Explosionen und die Flammenausbreitung reproduziert. CFD-Simulationen werden durchgeführt, um ein ähnliches Szenario wie das experimentelle zu untersuchen. Homogene und inhomogene Mischungen mit unterschiedlichen Randbedingungen am Austrittsbereich der T-Rohre werden simuliert.

Das in der CFD-Software implementierte Verbrennungsmodell und die Navier-Stokes-Gleichungen werden detailliert dargestellt. Ziel ist es dabei ein angemessenes Verbrennungsmodell auszuwählen, welches akkurat mager-vorgemischte und vorgemischte Flammenphänomene im kleinen Massstab numerisch simulieren kann.

Auf Grundlage der experimentellen und numerischen Untersuchungen werden in der hiesigen Arbeit aufbauend auf das Phänomen der „Tulip Flame"andere Stufen der Flammenausbreitung vorgeschlagen. Die experimentellen und numerischen Ergebnisse der Simulation werden verglichen um die Genauigkeit der, in der numerischen Software implementierten theoretischen Modelle zu analysieren. Die Auswirkung einer gebogenen Region bei der Flammenausbreitung für magere, stöchiometrische und inhomogene Methan-Luft-Vorgemische wird in der vorliegenden Arbeit detailliert dargestellt und besprochen.

Contents

List of Figures

List of Tables

Nomenclature

Latin Characters		Units
$a[0, 1, 2, 3, 4]$	temperature coefficients of Janaf coefficients	[1]
$a[5]$	enthalpy temperature offset coefficients o Janaf coefficients	[1]
$a[6]$	entropy temperature offset coefficient of Janaf coefficients	[1]
b	regressive variable	[1]
c	progressive variable	[1]
c'	cubeRootVol's coefficient for LES delta model	[1]
c_i	molar fraction	[1]
c_t	turbulent progressive variable	[1]
C_p	heat capacity	[J/kmol/K]
Co	Courant number	[1]
d	tube diameter	[m]
Da	Damköhler number	[1]
dV	volume element	[m^3]
dS	surface integral	[m^2]
E	wall function parameter	[1]
f	turbulence flow property	[1]
$\overline{f}$	property mean value	[1]
$\overline{f'}$	fluctuation mean value	[1]
ft	fuel mixture fraction	[1]
H	enthalpy from Janaf coefficients	[J/kmol]
h_f^i	heat of formation	[KJ/kmol]
i	chemical specie	[1]
I	intensity	[1]
k	turbulence kinetic energy	[J/kg]
k_w	wall function constant	[1]
Ka	Karlovitz number	[1]
l	length scale	[m]

L	domain size	[m]
L_E	Eulerian length scale	[m]
$L_{E,\parallel}$	longitudinal Eulerian length scale	[m]
$L_{E,\perp}$	transversal Eulerian length scale	[m]
l_t	turbulent length scale	[m]
l_l	integral length scale	[m]
Le	Lewis number	[1]
M	preconditioner parameter	[1]
m_{fuel}	fuel mass concentration	[1]
m_{ox}	oxidizer mass concentration	[1]
n	face unit normal	[1]
N	number of divisions	[1]
$_{fuel}$	fuel moles concentration	[1]
$_{ox}$	oxidizer moles concentration	[1]
P_0	initial pressure	[Pa]
P	pressure	[Pa]
Pe	Peclet number	[1]
Q	full gradient of a property	[1]
r	general eddy size	[m]
R	universal constant gases	[J/mol/K]
Re	Reynolds number	[1]
Re_η	Kolmogorov Reynolds number	[1]
S	flame speed	[m/s]
S_{ij}	symmetric part of velocity gradient tensor	[1]
S_b	reaction progress source term	$[T^{-1}]$
S_L	laminar flame speed	[m/s]
S_t	turbulent flame speed	[m/s]
S	entropy	[J/K]
Sc	Schmidt number	[1]
T	temperature	[K]
T_s	Sutherland temperature	[K]
T_{eq}	equilibrium temperature	[K]
T_{ref}	reference temperature	[K]
T_0	initial fresh gas temperature	[K]
T_{ad}	adiabatic flame temperature	[K]
Ue	internal energy	[J]
$|U|$	magnitude of the local velocity	[m/s]

U	main velocity	[m/s]
u'	RMS turbulent velocity	[m/s]
$u_i = u, v, w$	velocity components	[m/s]
$u'(r)$	RMS turbulent velocity for certain length	[m/s]
u_τ	friction velocity	[m/s]
x	local variable	[1]
Y	mass fraction	[1]
y^+	wall distance dimensionless number	[1]
y	wall distance	[m]
W_g	Gulder's coefficients for laminar	[m/s]
W	wall quantities	[1]
Sc_t	turbulent Schmidt number	[1]

Greek Characters   Units

α	pressure Gulder coefficient	[Pa]
α_{eff}	effective thermal diffusivity	[m^2/s]
β	temperature Gulder coefficient	[K]
δ_L	flame thickness	[m]
ϵ	dissipation rate	[J/kg/s]
η_k	Kolmogorov scale	[m]
Γ	diffusion coefficient	[m^2/s]
$Kappa$	wall function parameter	[1]
κ	strain	[1]
μ	dynamic viscosity	[kg/m/s]
μ_t	turbulent dynamic viscosity	[kg/m/s]
ν	kinematic viscosity	[m^2/s]]
Φ	equivalence ratio	[1]
ϕ	arbitrarily quantity property	[1]
ρ_u	density of unburnt mixture velocity for certain length	[kg/m 3]
σ_l	laminar surface tension	[J/m^2]
σ_t	turbulent surface tension	[J/m^2]
τ_c	chemical time scale	[s]
τ_m	mechanical time scale	[s]
τ_t	turbulence time scale	[s]
τ_w	wall shear stress	[Pa]
τ_η	Kolmogorov time scale	[s]

Superscripts   # Units

i	specie	$[-]$

Subscripts   # Units

$0, 1, 2, 3, 4$	condition	$[-]$
ad	adiabatic	$[-]$
b	burnt	$[-]$
c	chemical	$[-]$
k	flame	$[-]$
E	Eulerian	$[-]$
i, j	specie	$[-]$
l	integral	$[-]$
L	laminar	$[-]$
L	mechanical	$[-]$
η	Kolmogorov scale	$[-]$
P	pressure	$[-]$
p	product	$[-]$
r	reactant	$[-]$
ref	reference	$[-]$
t	turbulent	$[-]$
u	unburnt	$[-]$
w	wall	$[-]$
$\parallel$	longitudinal	$[-]$
$\perp$	transversal	$[-]$

List of Acronyms

BC	Boundary Condition
Bi-CG	Bi-Conjugate Gradient
BML	Bray Moss Libbyt
CFD	Computational Fluid Dynamics
DAQ	Data Acquisition
DES	Detached Eddy Simulation
DIC	Diagonal-based Incomplete Cholesky
DICGaussSeidel	Diagonal based Incomplete Cholesky/GaussSeidel
DILU	Diagonal Based Incomplete
DNS	Direct Numerical Simulation
EBU	Eddy Break Up
FDIC	Faster Diagonal-based Incomplete Choleskt
FPS	Frames Per Second
FVM	Finite Volume Method
GAMG	Geometric Algebraic Multigrid
GNU	General Public License
LEL	Lower Explosion Limit
LES	Large Eddy Simulation
OpenFOAM	Open source Field Operation and Manipulation
PCG	Preconditioned Conjugate Gradient
PBiCGStab	Preconditioned Bi-Conjugate Gradient
PBiCG	Preconditioned Bi-Conjugate Gradient
PDF	Product Density Function
PET	Polyethylene terephthalate
PISO	Pressure-Implicit with Splitting of Operators
PIV	Particle Image Velocimetry
PLC	Programming Logic Controller
RAS	Reynolds-Averaged Simulation

RDT	Rapid Distortion Theory
RMS	Root Mean Square
SGS	Smagorinsky Subgrid Scale
SIMPLE	Semi-Implicit Method for Pressure-Linked Equations
UEL	Upper Explosion Limit

1. Introduction

1.1 Background

Methane is extracted from oil camp productions and largely used in industrial design projects and operations. Methane-air combustion is a fundamental topic for the improvement of combustion systems like combustion engines and a homogeneous and inhomogeneous premixed gas turbine combustor. Additionally, combustion systems with methane-air mixtures have a lower and upper explosion limit which requests attention to remain safety procedures in the manipulation. Many of the methane-air processes happen in complex scenarios whereby it is necessary to understand the gas and flame propagates [11].

Flame propagation belongs to a study conjunct called "Reactive Fluid Dynamics". The numerical modeling of this phenomenon is difficult due to the complexity to implement the reactions in the governing equations and the high gradient variation of the parameters. It is also difficult to be experimentally evaluated because of the adversity to measure and collect data on flame propagation.

Flame propagation in daily complex geometries is difficult to be imitated in the laboratory. Hence T-pipe geometries with and without obstacles are used to imitate complex geometries due to the bent region. The experimental investigation constitutes of an inhomogeneous premixed explosion and flame propagation. The flame front and region behind the flame front crossing a straight and bent region of the T-pipe are analyzed. The methane-air flame propagation is monitored with a High-Speed Camera (HSC) and posterior investigated trough image processing methods. But the flame shows adversities in the visualization due to the complexity to capture a good image quality of the flame propagation. Some techniques are applied to gain better visualization of the flame front and especially of the region behind the flame front. The pressure is likewise monitored during the flame propagation.

The numerical investigation complements the experimental investigation to gain a better understanding of the phenomenon. OpenFOAM offers a packet of codes for a numerical investigation of homogeneous and inhomogeneous premixed flames. As an open-source, the software concedes the possibility to read and modify code details. The governing equations,

their discretization, and the numerical methods to solve them are implemented in the software using the language c++. The governing equations are described in this work because it is important to place the studied phenomenon in the correct model which reproduces with accuracy the phenomenon in CFD simulations.

The experiments are performed with an inhomogeneous methane-air mixture. This mixture shows a high results variation in the experiment and a challenge to implement the inhomogeneous factor in numerical investigations. Nevertheless, it is an important phenomenon to be studied because it enhances another perspective for new theories and numerical methods to preview situations in other scenarios.

This study aims to gain a better understanding of inhomogeneous premixed flame propagation in simple and complex geometries.

1.2   Previous and Related Studies

There exist a variety of publications dealing with a similar topic with experimental and numerical investigations. Clanet and Searby [12] proposed in 1996 four stages of flame propagation where a propane-air mixture was experimentally monitored. The phenomenon observed is largely studied in straight pipes in different scenarios where the initial temperature and/or pressure are increased, and in use of other fuels. Meanwhile, experimental techniques improved, especially regarding the HSC which records with high quality and number of frames per second. Mostly, studies of flame propagation in straight pipes focus on the flame front visualization. Here, new stages based on Clanet's and Searby's work shall be proposed.

In 2016 Xiao [13] investigated the hydrogen flame propagation in a straight pipe also dealing with the "Tulip Flame" phenomenon. In his experimental investigation, he used the Schlieren photography technique to record the flame propagation. Xiao also performed a numerical investigation of premixed flame propagation. In contrast to both previous studies which focus on the investigation of the flame front, this work aims attention at the flame front as well as the region behind the flame front.

Wang [62] studied premixed methane-air propagation in a straight pipe with different obstacles format and outlet polyethylene terephthalate (PET) foil to seal the pipe. Wang exposed the variation of flame speed, format, and pressure for different methane-air concentrations.

The accessibility to the source code improves the understanding of the CFD implementation. The software offers the modification of the source code which allows the user to test new methods. Yasari's [14] work presented a flame propagation simulation where the combustion code *XiFoam* was described. He also performed simulations with and without modification of the source code *XiFoam*. Sempionato [15], on the other hand, clarified the implementation of the governing equation, combustion models, and chemical reactions of the *XiFoam* code. Furthermore, he performed CFD simulations. Both studies improved the preconceptions to perform the CFD simulation in this work.

1.3 Thesis Outline

Chapter 2 presents the assumptions and definitions of homogeneous and inhomogeneous pre-mixed flames for the studied scenario. The focus lays on the description of the methane-air stoichiometric reactions as well as the definition and estimation methods of thermodynamic and transport properties for the numerical investigations.

In Chapter 3 the combustion model is described to gain a better understanding of the model applied in the code and used for the CFD simulations. To establish the studied scenario in the correct combustion model is important for an accurate and realistic CFD simulation.

Chapter 4 describes the Navier-Stokes equations used in the selected combustion model. The governing equations are detailed by code and equations for each parameter that defines a flame propagation in complex geometries. The discretization of the governing equations is presented in detail including the algorithm control for pressure and velocity estimation and the mathematical methods used in the parameter value estimations.

Chapter 5 discusses the applied gauges, the equipment construction, and the methodology of the experimental performance in this work. Furthermore, the experimental results are analyzed. The collected pressure with a piezoelectric pressure sensor is submitted to data analysis. The recorded images with HSC are investigated by image processing techniques. This investigation has the purpose to estimate the flame front average speed as well as the flame stages, behavior, shape and turbulent vorticity.

Chapter 6 describes the procedures of numerical investigation settings. Boundary and initial conditions for the flame propagation simulation in OpenFOAM are defined. Designs of geometries used in the experiments and their representations in the numerical investigation by meshes are likewise discussed. Methods and assumptions about the applied combustion model are set up as well as the thermodynamic, turbulence and discretization of governing equations.

Chapter 7 discusses the simulation results to improve the understanding of the phenomenon observed in the experiments.

2. Premixed Flame

The flame production from gas mixture combustion can happen in the presence or absence of a previous mixture. When fuel and oxidizer are not mixed before to get in the combustion chamber it is defined as a diffusion flame. Corresponding examples for these are a fuel gas oven and a candle. The premixed flames consist of a previous mixture of fuel with oxidizer before getting in the combustion chamber [1, 16].

The previous mixture can be homogeneous or inhomogeneous. The difference between this type of mixtures is how mixed are the fuel and oxidizer. The homogeneous premixed flame is applied for mixtures which have an equal distribution of gas and oxidizer. In the case of an inhomogeneous premixed flame, the flammability limit does not follow precisely the homogenous flammability database [8]. The inhomogeneous mixture is more difficult to be reviewed and investigated experimentally and numerically [2].

Premixed numerical flames simulations are categories of fluid dynamics that consist of fluid dynamics with a chemical reaction. The main difference in comparison with nonreactive fluid dynamics is that the chemical species from the reaction which impact the governing equations [2, 17]. The combustion models for premixed flames are developed out of experiments' data and theoretical suppositions. In this work, the current combustion models in numerical simulations are tested and compared with the experimental results. The simulations are performed to reproduce and understand better the phenomenon observed in the experimental results.

There are several CFD software which can be used to study the phenomenon of premixed flames. Here the software OpenFOAM is used, which is an open-source computational fluid dynamic software based on a finite volume method under the General Public License (GNU) system [7, 10]. The software offers a packet of codes named *solvers* for different phenomena such as incompressible, multiphase, compressible, heat transfer, electromagnetic, combustion, next to others. Inside of the packets for combustion numerical simulations, there are codes for different scenarios of combustion from small until big scale geometries and fast and slow chemical time reactions. Nevertheless, before choosing the combustion *solvers* from the combustion packets possibilities it is necessary to know the parameters which affect

the governing equations and describe accurately the fluid dynamic of the flow.

2.1 Stoichiometry

The description of the reactions and species of the fluid is important to define the governing equation for reactive fluid dynamics. The air used in the experiment is from the environment which is estimated to have a concentration of 78.09 % nitrogen, 20.95 % oxygen, 0.93 % argon, 0.04 % carbon dioxide, and small amounts of other gases [18].

In this investigation, gas fuel methane is used. For the studied scenario, it is assumed that this fuel has a simple molecular structure which does not show multiple and complex reactions. Thus it does not have a high amount of byproduct from the combustion [2, 16].

Following this approach, it is possible to assume that the stoichiometry reaction is one single reaction from fuels to products [1, 16]. The general step of each reaction is described as
$CH_4 + 2(O_2 + 3.76N_2) \rightarrow CO_2 + 2H_2O + 7.52N_2$.
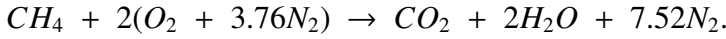
Zeldovich and Frank-Kamenetsky [19] proposed a reaction zone divided into preheating, reaction, and equilibrium. Figure 2.1 presents a reaction structure for a mixture of flame propagation with the same amount and the opposite direction of flow velocity and burning velocity. This sketch reaction shows a reaction rich in oxidizer and the depletion of fuel.
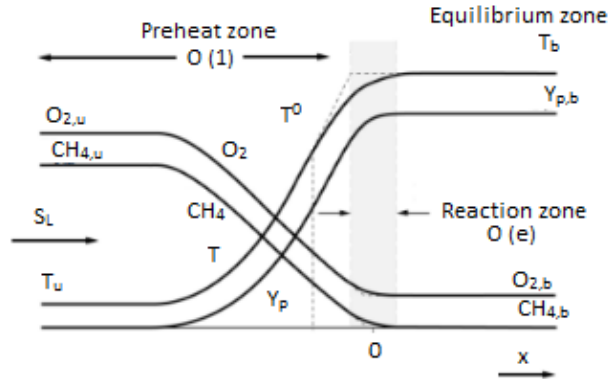
Figure 2.1: Reaction structure of previous mixed flame propagation [1]

In numerical investigations, premixed flames are represented as homogeneous and inhomogeneous mixtures. In a homogeneous mixture, the oxidizer and the fuel are supposed to be mixed perfectly inside the chamber. This mixture is called *Reactants*. The stoichiometric approach is the reaction happening until the depletion of the fuel or oxidizer. This reaction product is called *Products*. The reaction zone is exclusively classified as: *Reactants* and *Products*.

The inhomogeneous mixture supposes that gas and fuel are not perfectly mixed, it has a reaction zone classified as *Fuel*, *Oxidant* and *Burnt Products*. These changes impact directly the numerical simulation codes because more parameters must be put in to describe the phenomenon for the inhomogenous premixed flame [1, 7, 14].

2.1.1 Flammability Limit

The flammability limits are defined based on the fuel-oxidizer mixture ratio. The fuel-oxidizer concentration is defined as lean, stoichiometric, and rich. The methane-air out of the lean and rich limits cannot be triggered even if there is an ignition source [16]. The flammability limit is essential for a safe process. The previous mixture experiments performed in the laboratory and the numerical simulations use the flammability limits illustrated Table 2.1 as a reference for the methane-air ratio.

Table 2.1: Flammability limits of CH_4 [8]

Fuel	LEL	UEL
Methane	5.0 %	15.0 %

2.1.2 Equivalence Ratio

The equivalence ratio method is used in the combustion chemical calculation [2, 18]. This method is based on the stoichiometric balance of the combustion reaction, see Equation 2.1.

$$\Phi = \frac{m_{fuel}/m_{ox}}{(m_{fuel}/m_{ox})_{st}} = \frac{n_{fuel}/n_{ox}}{(n_{fuel}/n_{ox})_{st}} \tag{2.1}$$

The flammability limit range from Table 2.1 of methane is converted into equivalence ratio due to the fact that the initial conditions and experiment results already use this notation.

2.2 Thermodynamics

The thermodynamic of the premixed flames setup is used to solve the governing equations and the experimental setup. The thermodynamic conditions set in the experiment and numerical simulation are in 1 atm for pressure and the ambient temperature of 300 K. During the experiment there is some variation in these values but not expressively.

The Janaf thermodynamic model is used to estimate the thermodynamic properties. The Janaf coefficients [20] evaluate specific heat capacity at the constant pressure C_p, enthalpy H and entropy S by a function based on 7 coefficients and 2 polynomials for a lower and a higher temperature range, see Equation 2.2, Equation 2.3 and Equation 2.4. These functions are valid in cases with temperatures until 6000 K and are used to generate thermodynamic properties data [6, 21].

$$Cp(T) = R\,(a[1] + a[2]\,T + a[3]\,T^2 + a[4]\,T^3 + a[5]\,T^4) \tag{2.2}$$

$$H(T) = R\,(a[1]\,T + (a[2]\,T^2)/2 + (a[3]\,T^3)/3 + (a[4]\,T^4)/4 + (a[5]\,T^5)/5 + a[6]) \tag{2.3}$$

$$S(T) = R\,(a[1]\,lnT + a[2]\,T + (a[3]\,T^2)/2 + (a[4]\,T^3)/3 + (a[5]\,T^4)/4 + a[7]) \tag{2.4}$$

Thermodynamic physical models are used to solve the energy equation for compressible flame fluid dynamic simulations. It enables to calculate the enthalpy for combustion mixture

based on laminar flame speed and regressive variable [6, 22].

OpenFOAM offers as well some useful tools named *thermophysical* to calculate some properties for the initial conditions of the numerical simulations, therefore see Chapter 6. These tools calculate for each fuel-air mass ratio, temperature and pressure the methane-air mixture fraction *ft*, oxygen residual concentration, and Janaf coefficients.

2.3 Adiabatic Flame Temperature

The adiabatic flame temperature T_{ad} is the maximum constant temperature that the flame can reach without heat loss, work production, and reactions changes [2, 16]. T_{ad} is estimated by the software Cantera, see Figure 2.2 [23]. The estimation of T_{ad} of the methane-air mixtures is important to estimate the flame thickness, see Section 3.1. Furthermore, it is also important to know T_{ad} to choose which kind of pipe material will be used because the pipe must support the flame temperature during the experiment performance based on the temperature estimated on Cantera calculations by the equivalence ratio.
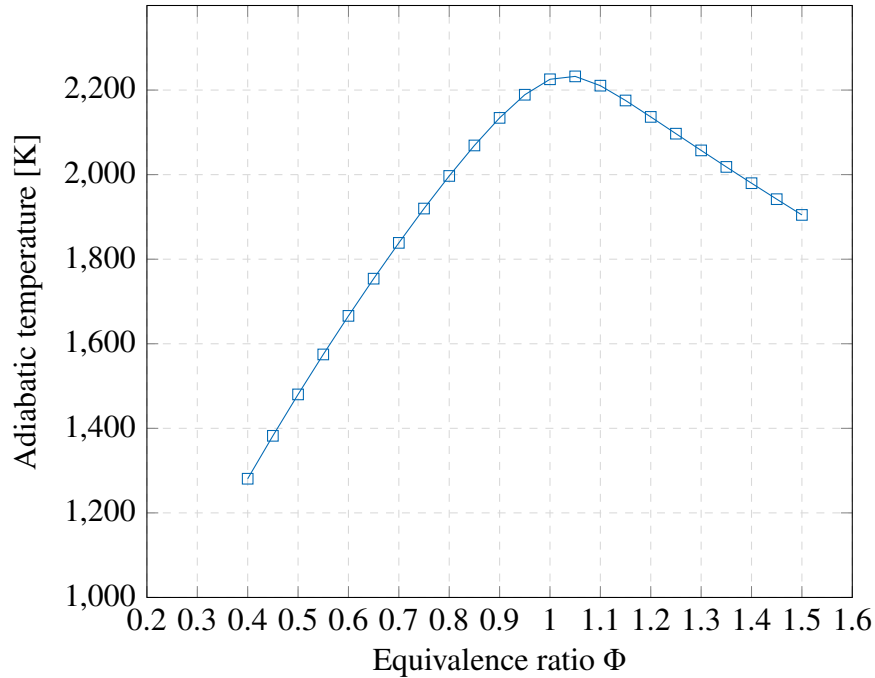
Figure 2.2: Adiabatic flame temperature estimation for methane-air mixtures

2.4   Transport Properties

The transport properties are used to calculate the dynamic viscosity μ for internal energy and enthalpy governing equations. The Sutherland transport model is used to calculate the dynamic viscosity μ as a function of temperature T from a Sutherland coefficient $A_s = 1.675212$ $\times 10^{-6}$) and Sutherland temperature $T_s = 170.672$ K , see Equation 2.5 [6, 22, 24].

$$\mu = \frac{A_s \sqrt{T}}{1 + T_s/T} \tag{2.5}$$

3. Combustion Models

3.1 Laminar Premix Flame

The laminar premixed flame is a stable flame propagation with the flame speed S_L around 20 cm/s until 100 cm/s. There are previous theoretical models to calculate the laminar premixed flame which are used to set up the initial conditions for the CFD simulations. The laminar flame speed is estimated using a model based on the temperature and pressure, see Equation 3.1 [2, 16, 23, 25].

$$S_L(P, T_{ref}) = S_L(P_0, T_0) \left(\frac{P}{P_0}\right)^\alpha \left(\frac{T_0}{T_{ref}}\right)^\beta \tag{3.1}$$

The flame speed increases with the rise of the initial temperature T_0 and decreases with the increase of the initial pressure P_0 [2, 3]. OpenFOAM uses personalized coefficients of the general Equation 3.1 to estimate the laminar flame speed, see Equation 3.2 by equivalence ratio Φ and Gulder's parameters, see Table 3.1.

$$S_L(P, T_{ref}) = W_g \Phi^n exp[-\xi(\Phi - 1.075] \left(\frac{P}{P_0}\right)^\alpha \left(\frac{T_0}{T_{ref}}\right)^\beta \tag{3.2}$$

T_0 is set up as initial condition and T_{ref} is a fixed temperature as reference temperature for Gulder's laminar flame speed equation. The laminar flame speed can be also estimated by a simple 1D flame numerical simulation in the software Cantera. This numerical simulation has a detailed reaction mechanism GRIMech 2.1. The software also estimated the burning velocity, laminar flame thickness and preheat zone thickness for different equivalence ratios. The laminar flame speed by Gulder's coefficients and Cantera is examined, see Section 3.1.

Table 3.1: Gulder's coefficients for flame speed estimation [9]

Parameters	Methane
W_g	0.422
η	0.15
ξ	5.18
α	2
β	-0.5
T_{ref}	300
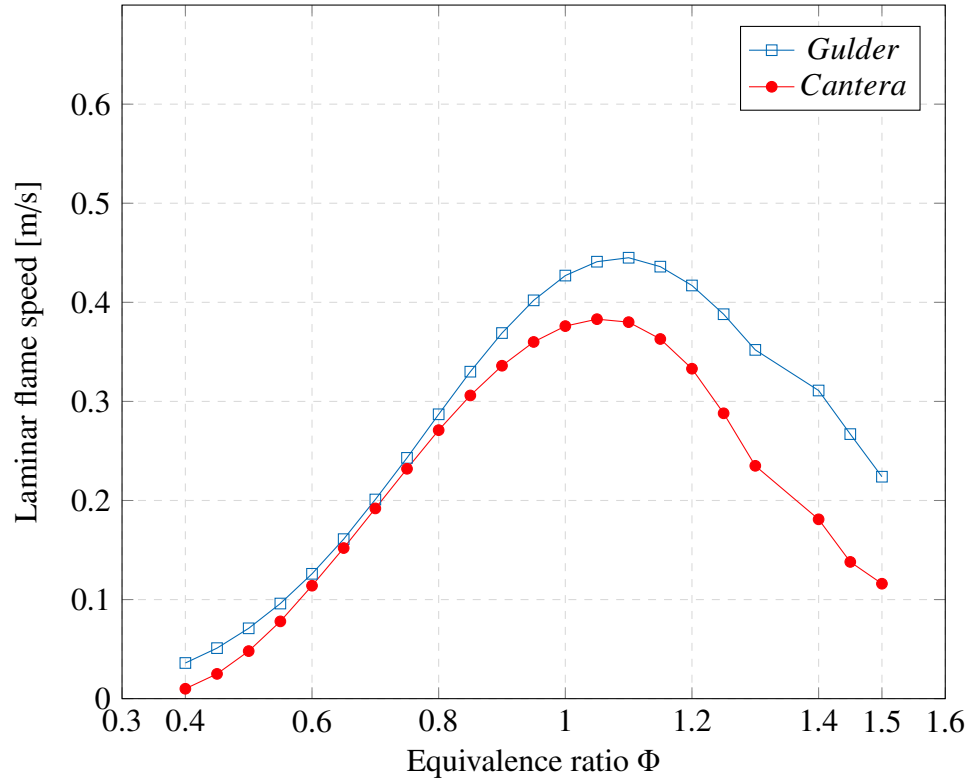
Figure 3.1: Laminar flame speed estimation for methane-air mixture for CH_4

The flame speed is calculated in Cantera because the flame thickness estimated in the next Chapter is also from Cantera. Thus it is necessary to observe if there is a large difference between the Gulder and Cantera laminar flame speed. Although, the Gulder's laminar flame speed is used in the numerical simulations performed in this work because it is the default model implemented in OpenFOAM software.

3.1.1 Laminar Flame Thickness

The laminar flame thickness can be estimated by following the reaction assumption with a single and irreversible reaction scenario. Besides, it is an important parameter because of its use to define the mesh for CFD simulations.

The flame thickness can be estimated by analytic models, scaling laws, and one-dimension CFD simulations of the flame front [1, 23]. One analytic model is the diffusive thickness which shows a relation between the thermal diffusivity and the laminar flame speed, see Equation 3.3. Thermal diffusivity property can be calculated by the software Cantera. However this length scale is too small and it is for DNS turbulence simulation [2, 3].

$$\delta = \frac{\lambda_1}{\rho_1 C_p S_L} = \frac{D_{th}^1}{S_L} \tag{3.3}$$

Another analytic model is the blint thickness method, see Equation 3.4. The blint thickness is calculated by the initial fresh gas temperature T_0 and the adiabatic flame temperature T_{ad}.

$$\delta_L^b = 2\frac{D_{th}^1}{S_L}(\frac{T_{ad}}{T_0})^{0.7} = 2\delta(\frac{T_{ad}}{T_0})^{0.7} \tag{3.4}$$

The thermal flame thickness is another method to calculate the laminar flame thickness, see Equation 3.5. This flame thickness method can be estimated by the software Cantera.

$$\delta_L = \frac{T_{ad} - T_0}{\max | \frac{\partial T}{\partial x} |} \tag{3.5}$$

Clark [26] calculated the flame thickness by experiments with premixed methane-air. The scenario consists of the equivalence ratio varying from 0.8 to 1.4, the ambient temperature of 298 K ± 5K, and a pressure of 100 kPa ± 5 kPa. Yamaoka [28] also estimated the flame thickness for similar conditions.

The thermal flame thickness temperature method is usually smaller than the experimental estimation of flame thickness. This thermal flame thickness is also used as a reference for mesh generation [23, 26, 29]. Figure 3.2 illustrates the flame thickness estimated by the analytic tools and Cantera as well as collected from experiments.
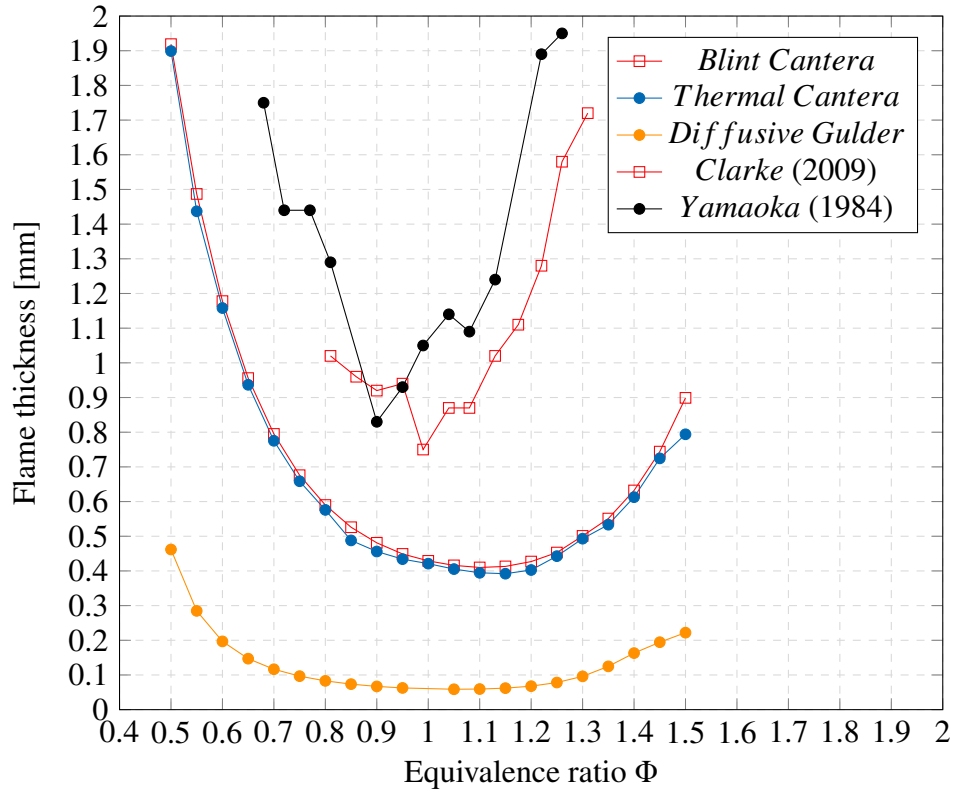
Figure 3.2: Flame thickness for CH_4

The diffusive flame thickness has a small length which is not realistic to implement in the mesh and turbulence models as Large Eddy Simulation (LES). The mesh should be generated having as reference a flame thickness based on a length between the blint or thermal flame and the flame thickness estimated in the experiment from Clark [26] or Yamaoka [28].

3.2   Flame Instabilities

There are several factors to impact flame instability such as heat loss, unbalance of chemical reactions in inhomogeneous mixtures, obstacles, bent geometries, and Boundary Conditions (BC) [30, 31]. Darrieus and Landau [32, 33] showed that the premixed flames tend to be unstable. And the flame propagation deals with thermal and diffusive instabilities, especially at the flame front.

The flame front is an interaction zone between the fresh gas and burned gas, see Figure 2.1. The instability of these zones is provoked by the shear force due to the expansion of the hot gases into the unburnt gas region. The different fluid conditions like temperature, fluid density, as well as velocity, viscosity, and dynamic pressure also provoke instabilities. The dimensionless Lewis number is used to describe the type of instability scenario. This number

is the ratio of thermal and molecular diffusivity. λ is the heat conductivity, D is the molecular diffusivity, ρ is the density and c_p is the pressure heat capacity, see Equation 3.6.

$$Le = \frac{\lambda}{D \rho c_p} \tag{3.6}$$

Lewis number is impacted by the flame front as Figure 3.3 indicates. Le=1 is a stable scenario between molecular transport with a heat loss caused by conductivity in the zone between fresh and burnt gases. Le > 1 is a scenario where the heat conductivity is higher than the molecular transport. Then it provokes a decrease of reactants to feed the flame and increase the heat loss due to conduction. This scenario is not considered an unstable scenario because it tends to decrease the flame speed and the burning rate. Le < 1 is an unstable scenario provoked by the increase of the flame temperature. This scenario has an increment of reactant transport into the flame which impacts the growth of the burning rate.
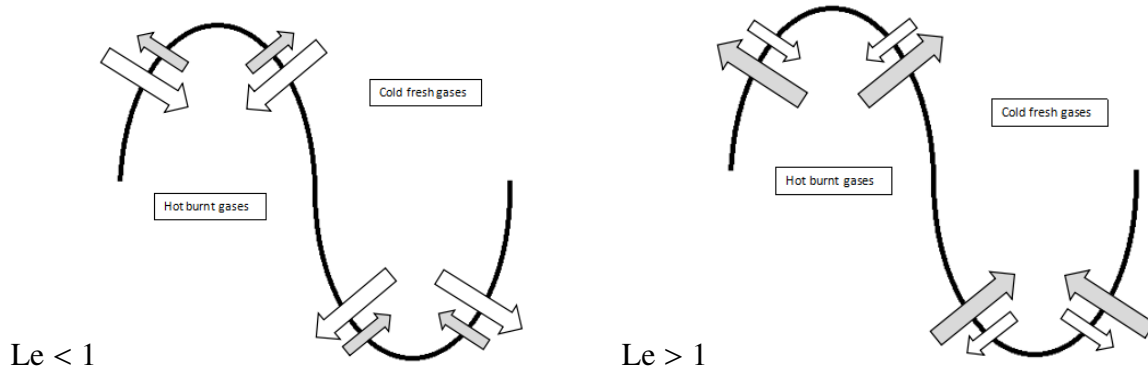
Figure 3.3: Flame instabilities [2]

3.3 Turbulent Flame

Turbulence is a fluid instability provoked by fluctuations of fluid properties. This phenomenon can be defined by the turbulence fluid property f which is equal to the sum of the mean value $\bar{f}$ and the fluctuation contribution $\overline{f'}$, see Equation 3.7 [34, 35].

$$f = \bar{f} + \overline{f'} \tag{3.7}$$

The turbulence has different levels of strength which is characterized by the turbulence intensity I. The intensity is defined as the ratio between the Root Mean Square (RMS) of the fluctuations $\overline{f'}$ and the mean value $\bar{f}$, see Equation 3.8. Usually it has a range from zero as laminar flow until 10% on wall bounded flows [3, 36].

$$I = \frac{\overline{f'}}{\bar{f}} \tag{3.8}$$

Assuming a turbulence model as homogeneous and isotropic [3, 37], it is possible to distinguish the turbulence scenario by the turbulent fluid propagation with different eddies scales

from the turbulence intensity. Eddies represent a scale of energy in a turbulent fluid. Turbulent scales are calculated to enable the analysis of the energy distribution by different length scales and the interaction of these length scales with the flame front [3, 35]. This calculation is based on the instabilities of the flame front which allows the turbulent eddies formations to modify the flame speed, flame thickness, mass consumption rate, and other parameters, discussed in Section 3.2 [2, 16, 38]. Notwithstanding, the turbulent intensity does not give enough information to define turbulent combustion. Experimental and numerical investigations are necessary to understand better the phenomenon [3, 34].

The eddies are represented in a small scale of energy with Kolmogorov length η_k until the largest scale with integral length scale l_t [2, 3, 39]. Figure 3.4 illustrates the length scales based on the assumption that the energy flux is constant and flows from the big eddies as l_t in direction of the small scales η_k [3, 40].
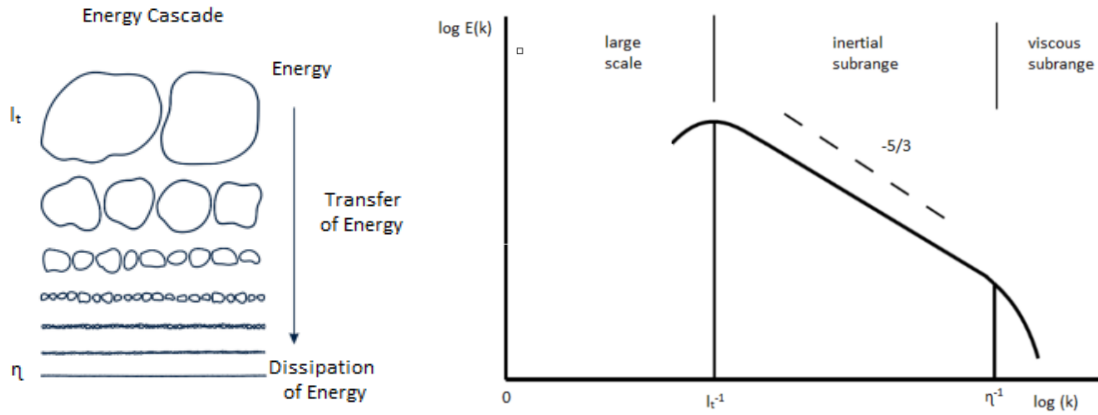
Figure 3.4: Eddies scales: (a) Energy cascade; (b) Logarithmic energy spectrum [1, 3]

Reynolds number is a dimensionless number used to differ the laminar to turbulent fluid flow. This number can be calculated for each scale or eddy size as defined in Equation 3.9 [35, 41]. $u'(r)$ is the characteristic velocity by the length scale with the size r and the flow kinematic viscosity ν.

$$Re(r) = \frac{u'(r)r}{\nu} \tag{3.9}$$

The turbulence dissipation rate ϵ can be defined by the ratio of kinetic energy k with the time scale r/u'(r), see Equation 3.10.

$$\epsilon = \frac{u^2(r)}{r/u'(r)} = C_D \frac{\overline{k}^{3/2}}{L} \tag{3.10}$$

There are several propositions based on experimental results to estimate the length scale r. Shchetinkov proposed Lagrangian and Eulerian length scales, respective Equation 3.11 and Equation 3.12 [42].

$$L_L = 0.02d \tag{3.11}$$

$$L_E = 0.04d \tag{3.12}$$

This work deals with flame propagation in complex geometries with longitudinal and transversal fluid flow scenarios. Shchetinkov and Pope proposed the Eulerian length scales for longitudinal $L_{E,\|}$ which is based on the pipe diameter d, see Equation 3.13 and the transversal $L_{E,\perp}$ which is defined as shown in Equation 3.14 [3, 42].

$$L_E = L_{E,\|} = 0.04d \tag{3.13}$$

$$L_{E,\|} = 2L_{E,\perp} \tag{3.14}$$

The method to estimate the length scales is not fixed and it has some limitations if the length scale L is higher than 0.08d, the $L_{E,\perp} = 2L_L$ and $L_{E,\|}/L_L < 8$ [3, 42]. Pope suggested an estimation of C_D for Eulerian longitudinal length scales, see Equation 3.15 [3].

$$\epsilon = 0.43\frac{\bar{k}^{3/2}}{L_{E,\|}} \approx 0.77\frac{u'^3}{L_{E,\|}} \tag{3.15}$$

Since Reynolds number is the ratio of inertia to viscous forces, the inertia and viscous forces tend to have a unit balance. The energy cascade is illustrated in Figure 3.4. Reynolds number from $Re(l_t)$ until $Re(\eta_k)$ is analyzed to conclude if the fractional rate of the flame front area changes, see Equation 3.16. The largest scales l_t in a turbulence scenario are not affected by the viscous dissipation and are mainly controlled by the inertia [2, 3]. That means for larges scales, the diffusion impacts in the momentum equation are insignificant. And only the non-linearity in the momentum behaves to move the kinetic energy from a large to a smaller scale.

$$Re_t = Re_t(l_t) = \frac{u'l_t}{\nu} \tag{3.16}$$

Kolmogorov Scale is the smallest scale in the turbulence flow. It is defined by the dissipation rate and viscosity, see Equation 3.17 and Equation 3.18 [2, 3, 43].

$$\eta_k = (\frac{\nu^3}{\epsilon})^{(1/4)} \tag{3.17}$$

$$Re_t = Re_t(\eta_k) = \frac{u'\eta_k}{\nu} = 1 \tag{3.18}$$

The relationship between the length scales is important to quantify the flame strain. This is an important parameter to observe the increase of the flame front area by the measurement of the fractional rate. The strains are connected with velocities gradients and can be expressed for general eddy size like Kolmogorov or integral length scales, respectively Equation 3.19, Equation 3.20 and Equation 3.21 [2, 3, 43].

$$\kappa(r) = \frac{u'(r)}{r} = \frac{\epsilon^{1/3}}{r^2} \tag{3.19}$$

$$\kappa(\eta_k) = \sqrt{\frac{\epsilon}{\nu}} \tag{3.20}$$

$$\kappa(l_t) = \frac{\epsilon}{u'^2} \approx \frac{\epsilon}{k} \tag{3.21}$$

The eddies in the dimensions of Kolmogorov have the smallest size as well as velocity. This length scales provoke the highest flame stretch. Equation 3.22 is the ratio between the flame strains.

$$\frac{\kappa(\eta_t)}{\kappa(l_t)} = \sqrt{\frac{l_t u'}{\nu}} = \sqrt{Re_t} \tag{3.22}$$

The time scale can be defined for different eddies by the length scales, see Equation 3.23.

$$\tau_m(r) = \frac{r}{u'(r)} = (\frac{r^2}{\epsilon})^{1/3} = \frac{1}{k(r)} \tag{3.23}$$

3.4　Combustion Diagram

A heuristic method is used to evaluate the premixed flame regime by diagram based on length scales and velocity scales ratios. This method is useful to describe the flame regime by the interaction of the flame front and flame thickness, see Figure 3.5. There are other diagram methods to describe the flame regime [2, 16, 43].
The flame front is estimated by the ratio of the laminar flame speed S_L^0 with fluctuation velocity u'_{rms} which is the square root of kinetic turbulence energy. The turbulence is defined by a ratio of length scale from Kolmogorov η_k until flame length scale l_f, see Equation 3.24.

$$l_f = \frac{\nu}{S_L} \tag{3.24}$$
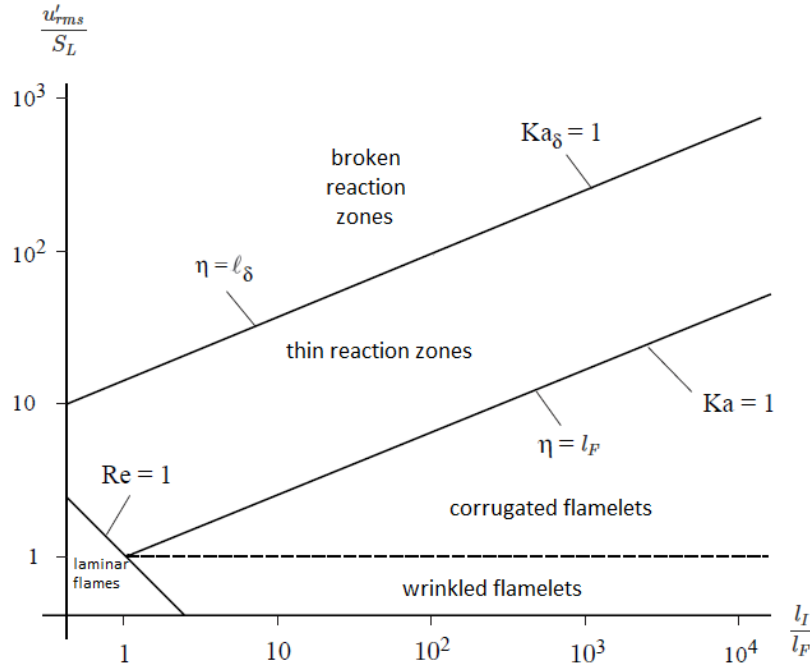
Figure 3.5: Turbulent combustion diagram [2, 3]

The turbulence cascade energy is defined by a local dissipation rate of turbulent kinetic energy. Thus ϵ is estimated for different scales from Kolmogorov u_k until integral ul_t velocities. Due to the assumptions on the turbulence of Section 3.3, it is possible to gain a better understanding of the interaction between turbulent fluid motions in the reaction zone for the reason that it provides velocity estimations and time variations by a length scale r, see Equation 3.25.

$$\epsilon = \frac{u'(r)^3}{r} \tag{3.25}$$

The turbulent time is estimated based on the mechanical time scale $t_m(r)$ with the relation between speed and times variations for a general eddy size r, indicated in Equation 3.26.

$$\tau_m(r) = \frac{r}{u'(r)} = \frac{r^{2/3}}{\epsilon^{1/3}} \tag{3.26}$$

The mechanical time $t_m(r)$ is estimated by the largest eddy structure, whereby an integral scale is applied, see Equation 3.27. The chemical time τ_c is estimated using the flame front thickness, see Equation 3.28.

$$\tau_m(l_t) = l_t/u' \tag{3.27}$$

$$\tau_c(l_t) = \delta/S_L^0 \tag{3.28}$$

The relation between the mechanical time and the chemical time is called Damköhler number $D_a(r)$. The number varies between the length scale values from Kolmogorov η_k until integral l_t where the eddies are described. $D_a \gg 1$ has a flow with small chemical time, thus the eddy from the turbulence does not have time to affect with significance the structure inside the flame. The flow is in laminar conditions and the main burning rate can be estimated by the laminar flame burning rate multiplied by the front flame surface. This scenario is called *flamelet limit*. $D_a \ll 1$ has a flow with high chemical time, hence it is the opposite scenario of $D_a \gg 1$. The chemical time is longer than the mechanical time $t_m(r)$ and the eddies have time to influence the turbulence. The reaction rate hinges on the chemistry between the reactants and the products´mixture by turbulence. This scenario is called *perfectly stirred reactor*. Damköhler for integral length scale is defined by the mechanical time for integral length scale $\tau_m(lt)$ divided by the chemical time τ_c, see Equation 3.29 [2, 3, 43].

$$D_a = \tau_m(r)/\tau_c \Rightarrow D_a(l_t) = \frac{\tau_m(l_t)}{\tau_c} = \frac{l_t/u'(l_t)}{\delta/S_L^0} \tag{3.29}$$

Karlovitz number is used for small eddies. It is the inverse proportion of Damköhler number in Kolmogorov scale η_k, see Equation 3.30.

$$K_a = \frac{1}{D_a(\eta_k)} = \frac{\tau_c}{\tau_k(\eta_k)} = \frac{u'(\eta_k)/\eta_k}{S_L^0/\delta} \tag{3.30}$$

3.5   Wall Flame Scenario

The interaction between wall and flame impacts the efficiency and pollutant generation of the flame, and the lifetime of the material on flame contact [2, 16]. Near-wall layers impact the

fluid behavior but it is a difficult phenomenon to be described and to be modeled in numerical simulations, especially for flame propagation [3, 36].

Flames propagate near the wall but do not necessarily hit the wall. The wall quenches the flame due to the low temperature that inhibits the chemical reactions. Flame near-wall layers can have a size smaller than 1 mm thick and deal with a high-temperature gradient. The flame has a temperature ranging from 1500 K until 2500 K and the wall from 400 K until 600 K [2, 16, 36].

An accurate model to describe the interaction between the flame and the wall for laminar and turbulent remains a challenge for CFD simulation and experiment observation. Nevertheless, exist certain assumptions for this phenomenon: (1) The flame quenches near the wall due to low temperature and it has an enthalpy loss. This contributes to the failure of BML models because it defines the scenario by the progress variable based on the temperature, see Section 3.6; (2) Another assumption represents the wall as adiabatic whereby a problem arises from the high heat transfer to the wall which is usually ignored by combustion models; (3) Supposing the turbulent length scale decreases near the wall while being smaller than flame thickness it provokes an unreal math calculation for models like the flamelet model.

The distance between the flame and the wall is defined as y. Flame thickness models can be used to normalize the distance y to define the Péclet number. Pe is a dimensionless number useful to describe the flame near-wall conditions for simple scenarios such as laminar. It is defined by the ratio of the advective transport rate of a physical quantity to its diffusive transport rate. Equation 3.31 shows the relation of the flame wall distance with the local Pe number [4, 36].

$$Pe = \frac{y}{\delta} \tag{3.31}$$

3.5.1   Wall Functions

Wall functions are applied due to the difficulty to model flame near-wall phenomenon for flame propagation, especially for turbulence scenarios. These wall functions are empirical models that deliver an accurate solution and satisfy the fluid flow physics conditions near the wall. They are used as a connection between the inner region of the wall and the turbulence scenario for the governing equations. Additionally, it saves computing time regarding the inertial force prevalent in the whole region. Schlichting defines the dimensionless distance from the wall y^+, the friction velocity u_τ and the wall shear stress τ_w, respective Equation 3.32, Equation 3.33 and Equation 3.34 [2, 4, 36].

$$y^+ = \frac{y \times u_\tau}{\nu} \tag{3.32}$$

$$u_\tau = \sqrt{\frac{\tau_w}{\rho}} \tag{3.33}$$

$$\tau_{wall} = \mu \frac{y^+}{u^+} \frac{u}{y} = (\mu + \mu_t)\frac{u}{y} \tag{3.34}$$

The wall functions remaining in the first cell center should be placed in the log area region to have an accurate solution, see Figure 3.6.
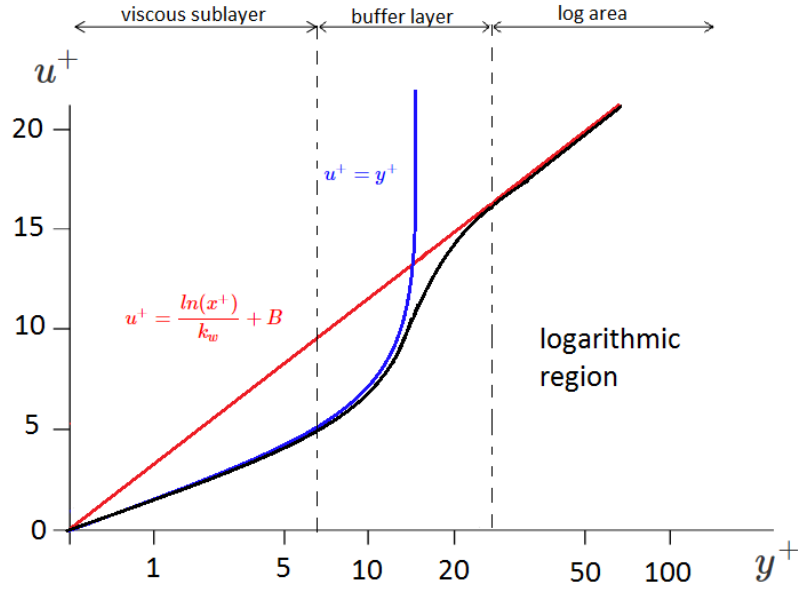
Figure 3.6: Relation between uplus and yplus in three parties of inner region [4]

It is assumed that the shear stress of the fluid is equivalent to the wall shear stress τ_w in the viscous sublayer ($y^+ < 5$), see Equation 3.35. The viscous sublayer is represented as the blue line in Figure 3.6.

$$u^+ = \frac{u}{u_\tau} = y^+ \tag{3.35}$$

OpenFOAM defines the buffer layer region by a linear relation of the viscous sublayer with the logarithmic region. In this region, the viscous and turbulent stresses have equivalent magnitude [4]. The logarithmic area ($30 < y^+ < 200$) is a region where the turbulence stress is predominant and the velocity profile changes slowly with the logarithmic function, see Equation 3.36. The dimensionless velocity estimated by *yplus* where $k_w \approx 0.41$ and B ≈ 5.1. The logarithmic region is represented as a red line in Figure 3.6.

$$u^+ = \frac{ln(y^+)}{Ck_w} + B \tag{3.36}$$

The wall functions are used as near-wall boundaries conditions in the simulation. Open-FOAM has the wall functions which calculates the value on the face of the first cell and another which estimates the value of the center of the cell adjacent to the wall. The parameters *yplus* evaluate the wall function models used in the simulations. *yplus* analysis where the first cell is located, friction velocity, and the wall shear stress [4, 6, 7].

3.6 Premixed Flame Model

The studied scenario consists of the flame propagation of previously mixed fuel-air. These mixtures can have different concentrations of oxidizers and fuel. In the respective literature exist plenty of combustion models for numerical investigations [16]. The combustion model

should deal with chemical reactions, thermodynamic and turbulence assumptions described along Chapter 2 and Chapter 3.

The EBU model proposed by Spalding [44] assumes a high Reynolds number (Re»1) and Damköhler number (Da»1). The fluid in the scenario is separated into unburnt (or fresh) and burnt. The turbulence time scale τ_t is higher than the chemical reaction scale τ_c. It also defines the reaction rate as a simple function based on the turbulent mixing time τ_t and the temperature. Thus the reaction rates are represented by turbulence motions [2, 3, 44, 45].

The BML proposed by Bray-Moss-Libby is a combustion model on the base of the EBU model. The BML model assumes also high Reynolds and Damköhler numbers for the phenomenon, one-step and irreversible chemical reaction, perfect gas stage, and isotropic energy conditions. The main difference regarding the BML is the implementation of the statistical tool Product Density Function (PDF). It is a physical analysis to describe the flame propagation scenario that improves the understanding of previously mixed flames. This model has been improved since its first formulation [2, 3, 43].

The BML model defines the element in the reaction zone by probabilities: α fresh mixture, β burned product and γ burning mixture. The progressive variable c and local variable x at the time t described as statistic parameters the flame scenario, see Equation 3.37 [24].

$$P(x, t, c) = \alpha(x, t)\delta(c) + \beta(x, t)\delta(1 - c) + \gamma(x, t)P_f(x, t, c) \tag{3.37}$$

α, β and γ are the probabilities to find each gas phase in the flame propagation scenario. $\gamma(c)$ and $\gamma (1 \; c)$ are respectively the Dirac delta functions corresponding to progressive variable c which defines the fresh gas ($c = 0$) and fully burnt one ($c = 1$). The burning mixture represented by $\gamma(x, t)P_f(x, t, c)$ is the flame front. If the flame front is too thin ($\gamma(x, t) << 1$) it can be ignored in the studied scenario. The normalization to define the unburnt and fresh by PDF restricts the Dirac function in the scenario, see Equation 3.38 and Equation 3.39.

$$\int_{-\infty}^{\infty} P(x)dx = 1 \tag{3.38}$$

$$\alpha(x, t) + \beta(x, t) = 1 \tag{3.39}$$

The probability is defined without the flame front, as indicated in Equation 3.40 and in Figure 3.7

$$P(x, t, c) = \alpha(x, t)\delta(c) + \beta(x, t)\delta(1 - c) \tag{3.40}$$
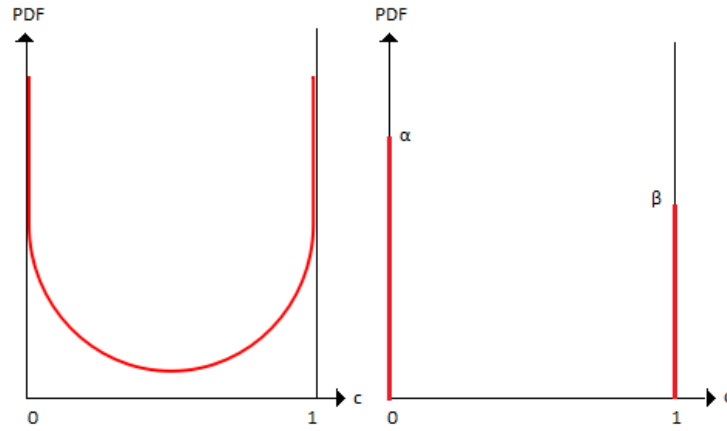
Figure 3.7: Probability density function in turbulent premixed combustion. (a) flamelet regime; (b) the bi-modal approximation in BML approach [2, 5]

Code *XiFoam* uses the regressive variable to set the initial conditions for the governing equation. These parameters can define gas as burnt or fresh by the quantities of reactant mass fraction or the temperature, see Equation 3.41.

$$c = 1 - b = \frac{Y_p + Y_r}{Y_p} = \frac{T - T_u}{T_b - T_u} \tag{3.41}$$

b is labeled as 0 for burnt mixture and 1 for unburnt mixture. The regressive variable in the combustion model *XiFoam* is estimated based on the initial temperature T, the unburnt temperature T_u and the burnt temperature T_b.

4. Navier-Stokes Equations

4.1 Governing Equations

Fluid dynamic simulations are based on the solution of governing equations for mass, momentum, energy, and other specific parameters that depend on the studied phenomenon. The governing equation can be formulated in a differential form for the application in a point or an integral form for the application in a region [22, 34, 46].

The numerical simulation in OpenFOAM and most of the CFD software use the control volume method which follows the Eulerian conservation law to analyze the phenomenon. The transport theorem is used to compute the derivatives of the integrated quantities based on the three-dimensional generalization by Leibniz integral rule. Premixed flames are compressible fluid dynamics. In consequence of the compression or expansion, the mass rate changes inside of the element. This provokes a variation in the density of the element. The integral form of a conserved continuity equation for compressible fluid dynamics is shown in Equation 4.1.

$$\frac{\partial}{\partial t} \int \rho dV = - \oint \rho \vec{U} \cdot n dS \qquad (4.1)$$

This method is conservative and can be applied to each volume as hexahedral, tetrahedral, and prism geometries. The surface integral dS is the balance of the in and outflow of a volume surface [34, 35, 47].

4.1.1 Continuity Equation

The continuity equation describes the general mass conservation, as indicated in Equation 4.2. It is a mass transport by convection or advection through the surface of an arbitrarily small volume control element dV in three dimensions. The mass transport is represented by mass per unit volume. The equation is the general governing equation with an arbitrary quantity ϕ equal to 1 [34, 35, 46].

Mass flux in the x-coordinate has the rate of mass entering and leaving from the element.

Mass flux is the multiplication of density by velocity on the surface area, see Equation 4.2. The rate of mass flowing through the element is calculated by the general continuity equation. [48, 49].

$$\frac{\partial \rho}{\partial t} = -(\frac{\partial(\rho u_x)}{\partial x} + \frac{\partial(\rho u_y)}{\partial y} + \frac{\partial(\rho u_z)}{\partial z}) \tag{4.2}$$

4.1.2 Momentum Equation

The momentum equation describes a phenomenon that is a fluid movement through the volume element with external physical acts. The momentum transport by convection is defined as the forces that flow through the element by the vector quantity $\rho * u$. Due to the vector property these forces act on the six faces of the element. Depending on the velocity gradient the molecular transport is an additional momentum that fluxes through the elements' surface. These fluxes are named stress τ. External forces act on the volume by gravity g and pressure p [22, 50].

As presented in Equation 4.3, the momentum equation is the general governing equation with arbitrarily quantity ϕ equal to density ρ multiplied by the velocity u. The two first terms from the right side of Equation 4.3 represent the momentum transport by convection. These terms depend on the vector quantity and the molecular transport which is represented by the velocity differences. These forces act in the three coordinates [34, 46, 48].

$$\begin{array}{ccccc} \partial(\rho\vec{U})/\partial t & = -\nabla \cdot (\phi\vec{U}) & -\nabla \cdot \mu\nabla\vec{U} & -\nabla p + \rho g \\ \text{Line} \quad 3 & 4 & 6 & 10 \end{array} \tag{4.3}$$

The momentum equation rewritten in the OpenFOAM code, see Table 4.1.

Table 4.1: Momentum equation

Line	Code
1	MRF.correctBoundaryVelocity(U);
2	fvVectorMatrix UEqn
3	(fvm::ddt(rho, U)
4	+ fvm::div(phi, U)
5	+ MRF.DDt(rho, U)
6	+ turbulence->divDevRhoReff(U)
7	== fvOptions(rho, U));
8	UEqn.relax();
9	fvOptions.constrain(UEqn);
10	if (pimple.momentumPredictor())
11	{solve(UEqn == -fvc::grad(p));
12	fvOptions.correct(U);
13	K = 0.5*magSqr(U);}

The turbulence term on line 5 is solved in another code using Favre average, therefore see Section 4.2. The pressure gradient is a complicated term that needs to be solved in a separate

code and as a compressible variable using Favre average. At the beginning of the governing equations' solution, the pressure has an unknown value. Hence a separate solution is necessary because it impacts the scope of the movement. A density field is created by the continuity equation to install a relation with the pressure field. The pressure is solved by Poisson Equation in Equation 4.4 to keep the mass conservation for compressible simulation [7, 34, 50].

$$\nabla \cdot (\nabla p) = -\nabla \cdot [\frac{\partial(\rho \overrightarrow{U})}{\partial t} + \nabla \cdot (\phi \overrightarrow{U}) + \nabla \cdot \mu \nabla \overrightarrow{U} \tag{4.4}$$

The solver *XiFoam* does not have the gravity effects implemented directly in the code. But the software offers the function *fvOptions* which enables the implementation of the gravity effect. The gravity term is applied in the simulations performed in this thesis but leads not in the direction of the flame propagation.

4.1.3   Energy Equation

The energy equation describes the total energy variation with thermal and mechanical energies in an arbitrary volume control dV, see Equation 4.5. It is defined by the first law of thermodynamics for an open and unsteady system with heat sources. The total energy is the sum of kinetic $\frac{1}{2}|U|^2$ and internal energies e [22, 46].

$$\frac{\partial}{\partial t}(\rho e + \frac{1}{2}\rho|\overrightarrow{U}|^2) = -\nabla \cdot \left(\rho \overrightarrow{U}(e + \frac{1}{2}|\overrightarrow{U}|^2)\right) - \nabla \cdot q + \rho(\overrightarrow{U} \cdot g) - \nabla \cdot (p\overrightarrow{U}) - \nabla \cdot [\tau \cdot \overrightarrow{U}] + \rho S \tag{4.5}$$

It is possible to calculate the kinetic or internal energy by calculating one of these energies and subtract it from the total energy. The calculation of kinetic energy is chosen because it is solely the multiplication of velocity in the momentum equation. The mechanical energy equation is defined by kinetic energy $\frac{1}{2}|U|^2$ applied in the governing equation, see Equation 4.6. The energy equation is calculated by the in and out flow of the cell plus the source terms. These terms are the pressure and shear-rate which act on the surface and the gravity that acts on the volume [22, 46].

$$\frac{\partial}{\partial t}(\frac{1}{2}\rho|\overrightarrow{U}|^2) = -\nabla \cdot \left(\rho \overrightarrow{U}(\frac{1}{2}|\overrightarrow{U}|^2)\right) - \nabla \cdot [\tau \cdot \overrightarrow{U}] - (-\tau : (\nabla \otimes \overrightarrow{U})) - \nabla \cdot (p\overrightarrow{U}) - p(-\nabla \cdot \overrightarrow{U}) + (\rho g) \cdot \overrightarrow{U} \tag{4.6}$$

4.2   Reynolds and Favre Average

Fluid flow parameters are calculated in each cell unit from the mesh. The finite volume control method for compressible fluid flows is represented by density. In this case, density is the rate of fluid mass by volume. Therefore it is complicated to solve the governing equations regarding all details which should be applied for physical accuracy. Furthermore, long simulation time is crucial for performance.
The approximation technique named Reynolds average is used for most of the non-reacting

numerical simulations which do not show fluctuations in the flow density. Reynolds average method represents an arbitrary quantity property ϕ by the local variable x at the time t. The quantity value $\phi(x, t)$ is split into the mean value $\bar{\phi}(x, t)$ and a fluctuating part $\phi'(x, t)$, see Equation 4.7 [3, 34].

$$\phi(x, t) = \bar{\phi}(x, t) + \phi'(x, t) \tag{4.7}$$

The main value $\bar{\phi}(x, t)$ can be calculated by three Reynolds averaging techniques: time averaging, ensemble averaging, and space averaging. The method which will be applied depends on the characteristics of the turbulence flow and the flow conditions [3, 47].

Reynolds average is not applicable for combustion simulations because the reactive fluid has a heat release that causes fluctuations in density. To solve the governing equation with a constant density an extra un-closed term generating an error is created. Reynolds average for instantaneous mass conservation is illustrated in Equation 4.8 [2, 3, 17].

$$\frac{\partial \bar{\rho}}{\partial t} + \frac{\partial \overline{\rho u_i}}{\partial x_i} = 0 \Rightarrow \frac{\partial \bar{\rho}}{\partial t} + \frac{\partial \overline{(\bar{\rho} + \rho')(\bar{u}_j + u_i)}}{\partial x_i} = 0 \Rightarrow \frac{\partial \bar{\rho}}{\partial t} + \frac{\partial (\bar{\rho}\,\bar{u}_i + \overline{\rho' u'_i})}{\partial x_i} = 0 \tag{4.8}$$

The unclosed terms $\overline{\rho' u'_j}$ are the correlation between density and velocity fluctuations. They act as mass source terms for the main flow fields $\bar{\rho}'$ and $\bar{u}'_j$. These unclosed terms are unknown and can be only closed by modeling. This causes problems for the CFD codes because it impacts the mass conservation of the governing equations [3, 14, 34].

To solve this problem the mass conservation equation is submitted into the Favre average method, whereby unknown terms are bypassed. The applied procedure for reactive fluid simulations can be called mass-weighted averaging or mass-averaging. Similarly written as Reynolds's average method, Favre average method is separated into time averaging, ensemble averaging, and space averaging. Unclosed terms can be avoided by changing the main value using Favre averaging instead. The quantity value is also split into main value $\widetilde{\phi}(x, t)$ and fluctuation from the main $\phi''(x, t)$, see Equation 4.9.

$$\phi(x, t) = \widetilde{\phi}(x, t) + \phi''(x, t) \tag{4.9}$$

The method represents the arbitrary quantity property ϕ with the density, see Equation 4.10 [2, 3, 46].

$$\widetilde{\phi}(x, t) = \frac{\overline{\rho x}}{\bar{\rho}} \tag{4.10}$$

The difference between Favre and Reynolds lies in the representation of the main value, illustrated in Equation 4.10. The fluctuation term $\phi''(x, t)$ is determined as $\widetilde{\phi''}(x, t) = 0$ for RANS turbulence models and as $\widetilde{\phi''}(x, t) \neq 0$ for LES. The density and the regressive variable are written in Favre method, respective Equation 4.11 and Equation 4.12.

$$\bar{\rho} = \frac{\rho_u}{1 + (\sigma - 1)\widetilde{c}} \tag{4.11}$$

σ is the density ratio ρ_u/ρ_b of the unburnt with burnt gas.

$$\bar{c} = \frac{\sigma\widetilde{c}}{1 + (\sigma - 1)\widetilde{c}} \tag{4.12}$$

The relation between Favre and Reynolds average is complicated and requires modeling. OpenFOAM uses for compressible simulations Favre average to solve the governing equations [7, 10].

4.3 Discretization of Governing Equations

Discretization is fundamental to gain an accurate simulation result, close to reality, and with the smallest possible error [49]. The discretization process from the governing equations is set by dictionaries *fvSchemes*, *fvSolution* and *controlDict* in OpenFOAM. *fvSchemes* sets the numerical discretization of the governing equation terms by the categories: transient, interpolation, gradient, divergent and Laplacian term. *fvSolution* sets the mathematical models, solution tolerance, pressure, and velocity algorithm to solve the governing equations. *controlDict* sets time control as simulation time intervals, start and end. Time control saves the governing equation solution by the time step submitted [6, 7, 10].

4.3.1 Transient Term

The transient term $\partial\rho\phi/\partial t$ is represented as the sub-dictionary *ddtSchemes*. This term defines if the simulation is at transient or steady-state. It is necessary to set a solution method, see Table 4.2 which depends on the running simulation for transient simulations. The term is equal to 0 for a steady-state. Transient terms variation is a parabolic function. The field in time dimension has to be defined, only for the spatial domain. Time discretization is set up in an integral form because OpenFOAM is encoded in the finite volume method [6, 7, 10].

Table 4.2: Temporal discretization methods [6, 7, 10]

Method	Description
Euler	First order; Implicit; Bounded
Crank Nicholson	Second order; Implicit; bounded; Off-centering coefficient ψ
Backward	Second order; Implicit
Steady State	Not solving the transient term

The set up the off-centering coefficient is crucial for the Crank Nicholson option. The coefficient ψ equal to 1 is pure Crank Nicholson and equal to 0 is Euler. OpenFOAM suggests ψ equal to 0.9 for practical engineering problems [6, 7, 10].

4.3.2 Gradient Term

The gradient term $\nabla\phi$ has an important role for an accurate simulation solution because it is used by the convective and diffusive terms from the governing equations. The gradient is represented by the sub-dictionary *gradSchemes*. Table 4.3 shows the discretization options. Tests and evaluations of the CFD simulations are important to find the discretization method with the highest accuracy [6, 7, 10, 34].

Table 4.3: Gradient discretization methods [6, 7, 10]

Method	Description
Gauss <interpolationScheme>	Second order; Gaussian face integration; Unlimited
Least Squares	Second order; Least squares; Unlimited
Fourth	Fourth order; Least squares; Unlimited
Limited <gradScheme>	Second order; Limited

Gauss method needs an interpolation method from the *interpolationScheme*, see Table 4.7 and Table 4.8. This interpolation is defined in a sub-dictionary of the gradient term. *Limited* method is used in the simulation when it is necessary to limit the mesh for the gradient term which does not extrapolate the face value. And the gradient term should be bounded by the neighboring cell values. This method calculates the neighborhood minimum and maximum values for the cell or face, see Table 4.4.

Table 4.4: Bounded for limited schemes [6, 7, 10]

Method	Description
Cell MD Limited	Limiter in each cell direction separately
Cell Limited	Limiter to all components of the gradient
Face MD Limited	Limiter in each cell direction separately
Face Limited	Limiter to all components of the gradient

This limitation keeps the monotonicity condition offering stability and boundedness of the governing equation solution. Usually, this gradient limit is improved in the velocity gradient, but it can be also applied in another gradient property like the dissipation rate ϵ and the turbulence kinetic energy k. The diffusive scale of *Limited* schemes from less to more, respectively: *Cell MD Limited*, *Cell Limited*, *Face MD Limited* and *Face Limited*. The gradient limiter uses the blending factor ψ equal to 0 for accuracy and 1 for stability [6, 7, 10].

Surface Normal Gradient
The surface normal gradient is the gradient term to evaluate the two cells center by the normal vector of the face cell. During the formulation of simulation and discretization, this component has to be set and it has its own component, see Table 4.5. It is also required to evaluate the Laplacian term by the Gaussian integration [6, 7, 10].

Table 4.5: Surface normal gradient [6, 7, 10]

Method	Description
Corrected	Explicit non-orthogonal correction
Uncorrected	No non-orthogonal correction
Limited ψ	Limited non-orthogonal correction
Bounded	Bounded correction for positive scalars
Fourth	Fourth order

In a surface-normal contribution, the full gradient of a property Q at a face and the face unit normal n can be interpolated from the cell-based gradient, see Equation 4.13.

$$\nabla_f^\perp Q = n \cdot (\nabla Q)_f \tag{4.13}$$

The *Limited* method has the coefficient which needs to be set up, see therefore Table 4.6.

Table 4.6: Limited set up option [6, 7, 10]

Method	Description
0	Corresponds to uncorrected
0.333	Non-orthogonal correction ≤ 0.5 orthogonal part
0.5	Non-orthogonal correction orthogonal part
1	Corresponds to corrected

4.3.3   Interpolation

The discretization of gradients, divergent and Laplacian terms of the governing equations require an interpolation. This method is used to transform values of the control volume cell centers to control volume face centers. The interpolation is set up in the sub-dictionary *interpolationSchemes*. The usual interpolation methods for discretization are illustrated in Table 4.7 [6, 7, 10].

Table 4.7: Interpolation methods [6, 7, 10]

Method	Description
linear	Linear interpolation (central differencing)
cubicCorrection	Cubic scheme
midPoint	Linear interpolation with symmetric weighting

There are cases where specific interpolation methods for numerical solutions are necessary, see Table 4.8.

Table 4.8: Interpolation methods [6, 7, 10]

Method	Description
Upwind	First order bounded
linearUpwind	First/second order linear upwind, bounded
skewLinear	Second order, (more) unbounded, skewness correction
limitedLinear	Second order accurate, unbounded
vanLeer	Second order accurate, bounded

4.3.4 Divergent Term

Discretization of the divergent term $\nabla \cdot U\phi$ is set in the sub-dictionary *divSchemes*. Open-FOAM only offers Gauss discretization methods which have to be combined with the interpolation method, see Table 4.7 and Table 4.8 [6, 7, 10].

4.3.5 Laplacian

Discretization of the Laplacian term $\nabla\cdot(\Gamma\nabla\phi)$ is set up in the sub-dictionary *lapalcianSchemes* whereby Γ is the diffusion coefficient. OpenFOAM offers only the Gauss method to solve the Laplacian term. The Laplacian form for a property ϕ is represented in Equation 4.14.

$$\nabla^2\phi = \frac{\partial^2}{\partial x_1^2}\phi + \frac{\partial^2}{\partial x_2^2}\phi + \frac{\partial^2}{\partial x_3^2}\phi \tag{4.14}$$

Gauss discretization method does not solve completely the Laplacian term. Therefore it is necessary to set up in the same sub-dictionary *lapalcianSchemes* the interpolation method for the diffusion coefficient, see Table 4.7 and Table 4.8. Also it is essential to set up the surface normal gradient, see Table 4.5 [6, 7, 10].

4.4 Algorithm Control

OpenFOAM offers the pressure-velocity algorithm SIMPLE, PISO and PIMPLE to receive a better and efficient solution, and decouple problems of the Navier-Stokes equations solution. This algorithm differs in the setup of the loop to solve the equations and to see if the simulation is at transient or steady-state.

These algorithms are important at the beginning of the simulation because of the unknown values pressure and the three velocity components (x,y,z) which are necessary for the solution of the momentum equation, despite it impacts the convergence. The algorithm computes the velocities to satisfy the momentum conservation, see Equation 4.3 and the pressure field, see Equation 4.4 to enforce the mass conservation in a predictor and a corrector strategy until the convergence criteria are reached.

The solver *XiFoam* for transient premixed flame simulation uses as default the algorithm PIMPLE which is executed every time step and is the junction between PISO and SIMPLE

algorithms. The algorithm works as illustrated in Figure 4.1. This algorithm has high stability over PISO because the premixed flame simulations contain large time steps with a maximum Courant number above 1 and the solution is inherently unstable. Even if the PIMPLE loop is entered only once, the algorithm is the same as PISO [7, 34, 46, 50].

The algorithm is set up in dictionary *fvSolution*. The outer corrector is called *nOuterCorrectors* and inner corrector is called *nCorrectors* in the PIMPLE algorithm.
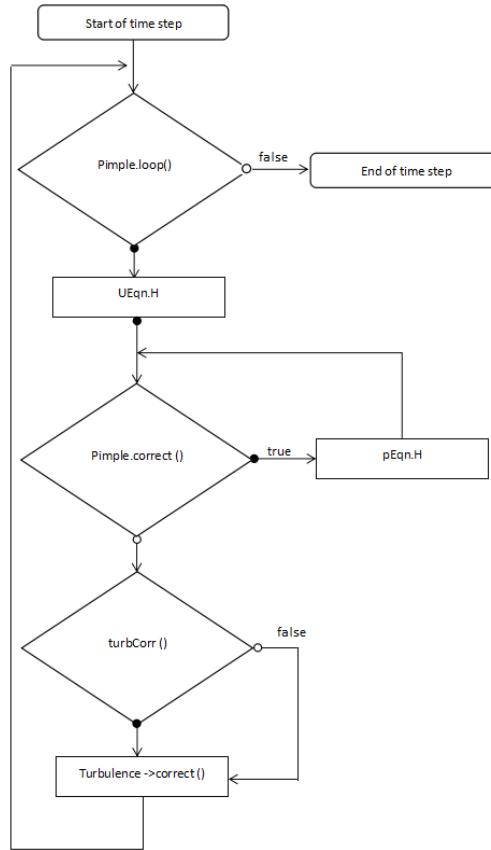
Figure 4.1: PIMPLE algorithm diagram [6, 7]

The outer corrector defines how many outer interactions the algorithm has to perform before moving to the next time step. If the criteria converge is reached before the number of the outer corrector previous set up, the simulation moves to the next time step. In case the criteria do not converge and reach the number of outer correctors defined, the simulation moves to the next time step. The inner corrector defines the number of times where the pressure and momentum correctors are solved within an interaction [7, 10, 46].

4.5   Mathematical Methods

Linear equation systems *Ax=B* of the governing equation are solved by director iterative mathematical methods. Variable *A* represents the matrix results of the linearization of the mesh. Variable *B* is a vector that represents the sources, constants, boundary conditions, and non-linearizable components. Variable x is the unknown variable located in the centroids of the mesh elements. The direct methods have high computational costs to solve the large sparse matrices.

These models like the tolerance solution are set up in the dictionary *fvSolution*, see Table 4.9. Models which specify the linear solution of each discretized equation are set up in the sub-dictionary *solvers* by the variable of the governing equation. The linear model can be for symmetric and asymmetric matrices. The symmetric matrix depends on the terms of the equation that is being solved, the time derivatives, and the Laplacian terms from the coefficients. Asymmetric matrices are used for an advective derivative. To evaluate the result is also important because if an asymmetric matrix is set up for an asymmetric simulation, the software displays a solution error [34, 50–52].

Table 4.9: Gradient discretization methods [6, 7, 10]

Linear Solver	Description
PCG/PBiCGStabd	Stabilized preconditioned (bi-)conjugate gradient, for both symmetric and asymmetric matrices
PCG/PBiCG	Preconditioned (bi-)conjugate gradient, with PCG for symmetric matrices, PBiCG for asymmetric matrices
smoothSolver	Solver that uses a smoother
GAMG	Generalized geometric-algebraic multigrid solver
diagonal	Diagonal solver for explicit systems

Preconditioners solvers resolve $M^{-1}Ax = M^{-1}b$ where M is the preconditioner, see Table 4.10. The preconditioners guide the information faster through the mesh which acts in conjugate gradient solvers. Test the preconditioners is important to choose which one fastens up the simulation [10, 51, 52].

Preconditioners can reduce the number of iterations, but do not reduce the mesh dependency of the number of iterations. Smooth solvers are used to solving this iteration problem, see Table 4.11. Tolerance, relative tolerance, a maximal number of iterations, and other parameters are set up and tested in the same sub-dictionary [34, 50–52].

Table 4.10: Preconditioners options [6, 7, 10]

Linear Solver	Description
DIC	Simplified diagonal-based incomplete Cholesky preconditioner for symmetric matrices (symmetric equivalent of DILU)
DILU	Simplified diagonal-based incomplete LU preconditioner for asymmetric matrices
FDIC	Faster version of the DICPreconditioner diagonal-based incomplete Cholesky preconditioner for symmetric matrices
Diagonal	Diagonal preconditioner for both symmetric and asymmetric matrices
GAMG	Geometric agglomerated algebraic multigrid preconditioner
none	no preconditioning for both symmetric and asymmetric matrices

Table 4.11: Smoothers options [6, 7, 10]

Linear Solver	Description
DIC	Simplified diagonal-based incomplete Cholesky smoother for symmetric matrices
DIC/GaussSeidel	Combined DIC/GaussSeidel smoother for symmetric matrices in which DIC smoothing is followed by GaussSeidel
DILU	Simplified DIC LU smoother for asymmetric matrices
DILU/GaussSeidel	Combined DILU/GaussSeidel smoother for asymmetric matrices in which DILU smoothing is followed by GaussSeidel
GaussSeidel	The GaussSeidel is method base in the Jacobi method

4.6   Numerical Modeling of the Premixed Flame

OpenFOAM offers code packets called *solvers* with different combustion models. There are *solvers* for different combustion scenarios, from small to big scale geometries, and fast and slow chemical time reactions. Before choosing the combustion *solver*, it is necessary to know the parameters which directly affect the governing equations and describe with accuracy the fluid dynamics.

The solver *XiFoam* is an exclusive combustion code for turbulent and laminar fluid dynamic simulations in compressible scenarios. The combustion model is based on BML models with some improvements. Wrinkle combustion models [5] with Gulders [9] correlations are used to define the combustion parameters in the governing equations. The code offers an inside ignition site to trigger the previous mixed reaction. It is developed for single and irreversible reactions. The reaction zone is defined by the mathematical tool PDF. Thermodynamic and kinetic settings support homogeneous and inhomogeneous previous mixed simulations. Additionally, they are able to simulate a phenomenon with high gradients of temperature and

pressure by the Janaf coefficients [6, 10, 14, 53].

XiFoam code offers some options of fuel-air previous mixtures, see Section 2.1. The homogeneous reaction zone defines the *Reactants* and *Products* by the regressive variable b. The inhomogeneous reaction zone defines *Fuel*, *Oxidant* and *Burnt Products* by the regressive variable b and the fuel mixture fraction by *ft*. The governing equation with the regressive variable parameter is shown in Equation 4.15 [6, 14, 15].

$$\frac{\partial(\rho b)}{\partial t} + \nabla(\rho \vec{U} b) \quad - \nabla \cdot \frac{\mu_t}{Sc_t} \nabla b = \quad -\rho S_b$$

$$\text{Line} \quad 2 \qquad 3 \qquad\qquad 6 \qquad\qquad 4 \text{ and } 5 \qquad\qquad (4.15)$$

The regressive transport equation is rewritten in an OpenFOAM code, see Table 4.12.

Table 4.12: Governing equation for progressive variable

Line	Code
1	fvScalarMatrix bEqn
2	(fvm::ddt(rho, b)
3	+ mvConvection->fvmDiv(phi, b)
4	+ fvm::div(phiSt, b)
5	- fvm::Sp(fvc::div(phiSt), b)
6	- fvm::laplacian(turbulence->alphaEff(), b)
7	== fvOptions(rho, b));

The reaction progress source term ρS_b has a negative term on line 5 because this technique helps to converge numerical calculation. The linearization of the equation is important to limit the convective term of the transport equation [6, 15]. The wrinkle factor *Xi* is the relation between the turbulent flame speed and the laminar flame speed as shown in Equation 4.16

$$\rho S_b = \rho_u S_L \Xi |\nabla b| \qquad\qquad (4.16)$$

Wrinkle factor Ξ can be calculated by transport or algebraic equations. The algebraic option calculates with a simple model based on Gulders correlations and a linear correction function, see Equation 4.17 [6, 54].

$$\Xi = \frac{S_t}{S_L} = 1 + 2(1 - b)\left(0.62 \sqrt{\frac{u'}{S_L} Re_\eta}\right) \qquad\qquad (4.17)$$

The transport option has also a linear correction function. It calculates the rate of generation with Gulders correlations and DNS data, see Equation 4.18. The terms in the transport equation are calculated, in Equation 4.18, Equation 4.19, Equation 4.20 and Equation 4.21.

$$\frac{\partial(\Xi)}{\partial t} + S_L \nabla(\Xi) = G(\Xi) - R(\Xi - 1) + (\sigma_l - \sigma_t)\Xi \qquad\qquad (4.18)$$

$$G = 2R\frac{(\Xi)_{eq} - 1}{X_{eq}} \qquad\qquad (4.19)$$

$$R = 0.28(\Xi)^*_{eq}\tau_\eta^{-1}((\Xi)^*_{eq} - 1)^{-1} \tag{4.20}$$

$$(\Xi)^*_{eq} = max[1, 1.28 \sqrt{\frac{u'S_L\,l_t}{\delta^{1/6}}}] \tag{4.21}$$

The inhomogenous mixture has the implementation of the parameter *ft* in the solution of the governing equation, see Equation 4.22 and it is shown on the code line in Table 4.13. *ft* is previously estimated with OpenFOAM's tool *adiabaticFlameT* and it is added as initial condition in the simulation.

$$\begin{array}{ccccc} \frac{\partial(\rho ft)}{\partial t} & + & \nabla(\rho\vec{U}ft) & -\nabla\cdot\,\alpha_{eff}\nabla ft = & 0 \\ \text{Line} \quad 2 & & 3 & 4 & \end{array} \tag{4.22}$$

Table 4.13: Governing equation for fuel mixture fraction

Line	Code
1	fvScalarMatrix ftEqn
2	fvm::ddt(rho, ft)
3	+ mvConvection->fvmDiv(phi, ft)
4	- fvm::laplacian(turbulence->alphaEff(), ft))
5	== fvOptions(rho, ft)

4.7   Numerical Modeling of the Turbulent Premixed Flame

Turbulence models are guided by the velocity gradient because errors increase and decrease due to the calculation of the gradient term. The mesh quality is also an important factor to drive the solution stability of the turbulence terms in the governing equations. The solver *XiFoam* offers the turbulence models Reynolds-Averaged Simulation (RAS) and LES. These models solve the governing equations using the Favre average for compressible simulations. OpenFOAM offers a packet of turbulence models that should be tested and evaluated for the simulated scenarios. Although only some models are discussed in this work.
The RAS turbulence model solves the turbulence terms by the main values of the quantities. The model does an ensemble average of the values for a moment of the balanced equation. It inhabits only the main flow field term and does not calculate eddy variations in small scales. RAS models are recommended for 2D reaction flow simulations. Some RAS models of OpenFOAM are described in Table 4.14 [2, 41].

Table 4.14: RAS turbulence models [6, 7, 10]

RAS Model	Description
LaunderSharmaKE	Low Reynolds number solve by k-epsilon for compressible and combustion flows including Rapid Distortion Theory (RDT) for compression terms
SpalartAllmaras	One equation mixing-length model for compressible external flows
kEpsilon	K-epsilon model for compressible flows including RDT based compression term.
kOmega	k-omega-SST turbulence model for compressible flows

RAS models require some conditions to receive a better solution of the governing equations. The flow with a high Reynolds number should have yplus between $30 < y^+ < 200$ for the first cell region at the logarithmic region, see Section 3.5. The flow with a low Reynolds number requires to resolve the mesh at viscous sub-layers using around 10 until 20 layers [4, 41].

LES models follow the basic concept to separate large eddies (length scales) from small eddies (Kolmogorov scale) in line with the assumption of the energy scale, further discussed in Section 3.3. Large scales are strongly affected by the boundary conditions plus they are instantaneously calculated in the governing equations. Small eddies are represented by subgrid closure rules. SGS implementation increases the accuracy of reaction flow simulations. The main difference between LES and RAS turbulence models is that the LES average operator is not the ensemble average as in RAS. Some LES models of OpenFOAM are described in Table 4.15 [41, 55]

Table 4.15: LES turbulence models [6, 7, 10]

LES Model	
Smagorinsky	Smagorinsky SGS model.
kEqn	One equation eddy-viscosity model
kOmegaSSTDES	k-omega-SST-DES (Detached Eddy Simulation) turbulence model for compressible flows

LES models have a better solution with isotropic mesh and in the viscous sub-layer. The governing equation terms should be solved with high order schemes because it is necessary to satisfy the solution of high energy eddies. The solution method *Limited* is applied in the governing equation terms to reduce the instability, therefore see Section 4.3.2 [41, 56].

LES models require to specify the delta model and its coefficients. OpenFOAM offers a packet of models although only two are discussed. The *cubeRootVol* is a simple cube-root ($\Delta = c' (V_{c'})^{\frac{1}{3}}$) calculation of cell volume delta used in SGS models. c' is a model coefficient determined in the turbulence setting. This model is appropriate for isotropic hexahedral meshes and less valid for cell aspect ratio differences. The Prandtl delta model, see Equa-

tion 4.23 is a mixing-length based damping function for specified geometric delta to improve near-wall behavior or SGS models.

$$\nu_t = l_m^2 \, | \, \overline{S_{ij}} \, |$$

(4.23)

Referring to Poinsot [2], one of the biggest problems for LES turbulence models in premixed flame simulations is the laminar flame thickness δ_L^0 because it has a scale of 0.1 to 1 mm. Due to the length scale, it is difficult to receive an accurate calculation of the flame front in the LES simulation meshes. LES filter help to get a better solution in the flame front thickness estimation.

Some of the linear eddy viscosity models of the RAS turbulence model offered in Open-FOAM are discussed. A common model is the two-equation k-epsilon which solves turbulence kinetic energy k and the turbulence dissipation rate ϵ by governing equations. In the turbulence model, an isotropic system is assumed so that the kinetic energy can be estimated for the initial conditions, see Equation 4.24. The turbulence dissipation rate can be estimated by Equation 4.25.

$$k = \frac{3}{2} \left(I \, | \, \mathbf{u}_{ref} \, | \right)^2$$

(4.24)

$$\epsilon = \frac{C_\mu^{0.75} k^{1.5}}{L}$$

(4.25)

OpenFOAM has some modifications implemented in the governing equations for the RAS *k-epsilon* model. The turbulence kinetic energy equation is described in Equation 4.26 and the dissipation rate, is shown in Equation 4.27. The terms are $C_\rho = 0.09$, $C_1 = 1.44$, $C_2 = 1.92$, $C_{3,RDT} = 0$, $\sigma_k = 1$ and $\sigma_\epsilon = 1.3$.

$$\frac{D}{Dt}(\rho k) = \nabla \cdot (\rho D_k \nabla k) + G_k - \frac{2}{3}\rho \left(\nabla \cdot \overrightarrow{U} \right) k - \rho \epsilon + S_k$$

(4.26)

$$\frac{D}{Dt}\rho \epsilon = \nabla \cdot (\rho D_\epsilon \nabla \epsilon) + \frac{C_1 G_k \epsilon}{k} - \left(\frac{2}{3}C_1 - C_{3,RDT} \right) \rho \left(\nabla \cdot \overrightarrow{U} \right) \epsilon - C_2 \rho \frac{\epsilon^2}{k} + S_\epsilon$$

(4.27)

The dissipation rate governing equation does not have buoyancy contributions and the second term in the r.h.s has the RDT contribution. The turbulence viscosity is obtained as shown in Equation 4.28.

$$\nu_t = C_\mu \frac{k^2}{\epsilon}$$

(4.28)

The *kEq* turbulence model for LES solves the turbulence terms using only the kinetic energy k in the governing equation, see Equation 4.29 where $C_e = 1.048$ and $C_k = 0.094$

$$\frac{D}{Dt}(\rho k) = \nabla (\rho D_k \nabla k) + \rho G - \frac{2}{3}\rho k \nabla \cdot \mathbf{u} - \frac{C_e \rho k^{1.5}}{\Delta} + S_k$$

(4.29)

5. Experimental Investigation of Flame Propagation

A small scale scenario with a transparent pipe is built to represent complex and simple geometries and evaluate flame propagation. The geometries used in this work are the T-pipes with and without obstacles and a straight pipe without obstacles. The flame propagation inside of the geometries is monitored in the experiments for different methane-air concentrations.

Through image processing of the recorded frames, the flame front stages, turbulent vorticity, behavior, and shape are evaluated and the average flame speed from one coordinate is estimated. The flame speed is estimated before and after the bent region of the T-pipes. Several experiments are performed to estimate the flame speed average rate. The pressure is also monitored during the flame propagation.

The geometries are built by a transparent polycarbonate material because it can resist explosion pressure and the adiabatic flame temperature for different methane-air concentrations. The range tested is based on the Lower Explosion Limit (LEL) and Upper Explosion Limit (UEL) of methane-air homogeneous mixtures [8]. The experiments have the same kind of methodology as well as the devices to monitor the flame propagation. The Dioxide of Titania (TiO$_2$) is used to gain better visualization of the flame [57].

5.1 Experimental Setup

Polycarbonate pipes are used to build the T-pipes and a straight pipe to perform the experiments. The pipe has a 60 mm external diameter and 6 mm thickness. The T-pipes have three section of 600 mm length. The bent region of the T-pipes is built with a pipe length of 600 mm which represents section I. This pipe length is glued on a pipe length of 1200 mm that represents section II and III. The T-pipe without obstacles has a system as indicated in Figure 5.1. The T-pipe with obstacles has a similar installation as the T-pipe without obstacles. The T-pipe has eight obstacles walls with an equal distance of 60 mm. These obstacles are

placed in section I and have a format to a half-circle of 27 mm radius and 3 mm thickness. The T-pipe with obstacles has a system as Figure 5.2. The straight pipe has one section of 2000 mm length, see Figure 5.3.

Both T-pipes are closed by polycarbonate foil at the beginning of section I and by PET foils at the end of section II and III. The straight pipe is closed by polycarbonate at the beginning of the pipe and by PET in the end. The flow meter which controls the input gas flow, the T&P, and piezoelectric pressure sensor devices are placed on the polycarbonate foil in section I as well as the straight pipe.
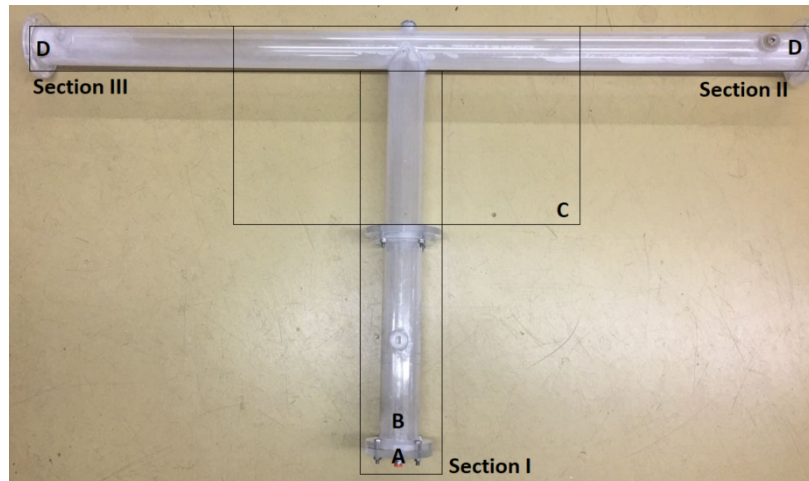

Figure 5.1: Experimental set divided by section: (a) Devices; (b) Conductors; (c) Record region; (d) Outlet PET foils
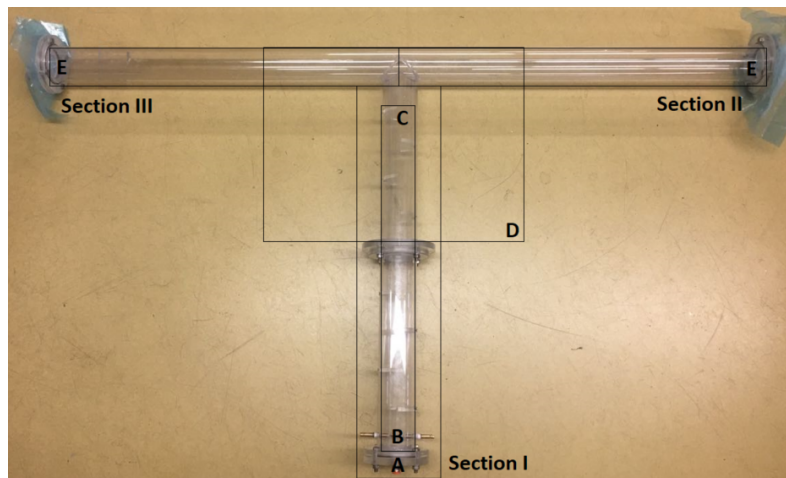

Figure 5.2: Experimental set divided by section: (a) Devices; (b) Conductors; (c) Obstacles; (d) Record Region; (e) Outlet PET foils
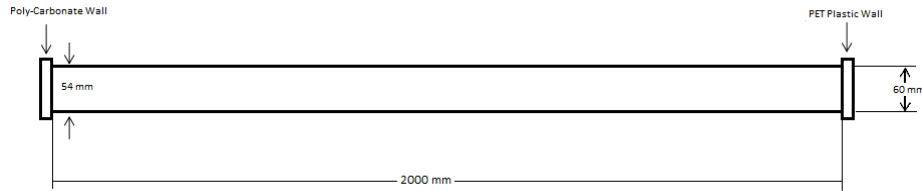
Figure 5.3: Straight pipe design

5.1.1 High-Speed Camera

The HSC is used to monitor the flame propagation inside of the pipes. It is only possible to record 2D frames with a high resolution because only one camera is used in the experiments. The premixed methane-air is triggered and the flame propagates inside of the pipe. It is difficult to record the exact moment the flame propagates in the region where the camera is set to record.

To select the frame rate is important because it enables to record the flame propagation with high image resolution. The frame record is brighter in a small frame rate and darker at a high frame rate. Moreover, the camera offers an open and closed brightness view. This function is important to control image brightness and avoid image saturation. The high-speed recording has physical limitations dealing with the image quality and the number of Frames Per Second (fps) [57, 58].

The camera used in this work is a Photron Mini UX 100. It is a full-frame camera with CMOS sensor, dynamic range ADC with 36-bit color. Furthermore, it has an exposure time from 3.76 us to 1.0 us which depends on the frame and the resolution. The camera is set up with 8000 fps and 1280 x 296 resolution. The lens used to capture the image is a Sigma 17-70 mm 1:2, 8-4, DC Macro OS HSMC [58].

5.1.2 Setup Devices

The T&P device is a Keller Druckmesstechnik, type PAA-33X / 80794, with a pressure range from 0 to 10 bar and output from 0 to 10 Volt. The methane-air concentration is estimated by the partial pressure inside of the pipe which is controlled by the T&P gauge over the ambient pressure previously measured. The methane-air mixture has no external heat. The device converts the pressure and temperature data and transfers it directly via USB connection to the software Control Center Series 30 (CCS30). The software data measure conversion model K-144B RS485 is from the same brand. The flow meter is a Red-Y type GSC-B9KA-BB24 from Vögtlin Instruments and the gauge is controlled by the software Get Red-Y. The flow meter is used together with the T&P device to control the gas fuel flow rate by the input valve. The explosion pressure is monitored with a piezoelectric pressure sensor from Kistler type 4045A4, and with an amplifier type 4765A5 for 0 to 5 bar, the output from 0 to 10 V, and measure a frequency of 40kHz. The amplifier transmits the measured data via board USB-6000 from National Instruments. This board is a USB device that provides eight single-ended analogic input (AI) channels, four digital input/output (DIO) channels, and a 32-bit counter.

To control the devices and reduce the errors in the setting the software, a Programming Logic Controller (PLC) diagram designed in Labview is used to set up the methane-air concentration. NI-Daqmx is a tool from Labview generally used as a data acquisition driver. This is a setup for devices that transmits data a source to sink. The pressure values need to be obtained from the source. The applied sink will be board USB-6000. For its proper operation, one end is grounded and the other end connected to a Kistler Voltage amplifier. A new NI-Daqmx global virtual channel is designed from the list of detected physical channels. In the configuration of the voltage input, the value range is specified with N acquisition samples at a rate of 1000 Hz. The output of Data Acquisition (DAQ) is sent to the function *Write to measurement* file which reads an array of data from the DAQ function. The data is constantly received as long as the loop runs and by defining local and global variables in the loop, the numeric value of pressure and voltage is obtained. The requisite data are written as Excel files for further usage in calculations.

A high-voltage electric spark is used as the ignition source for the fuel-air mixture. The electrical ignition system is built up by two electronic conducts and a Neon Resinblock-2000 model SBE63IT2 transformer. The electronic conducts are placed 1.5 cm distant from the polycarbonate foil, and the tips of the electrode had 6 mm distance, see Figure Figure 5.4.
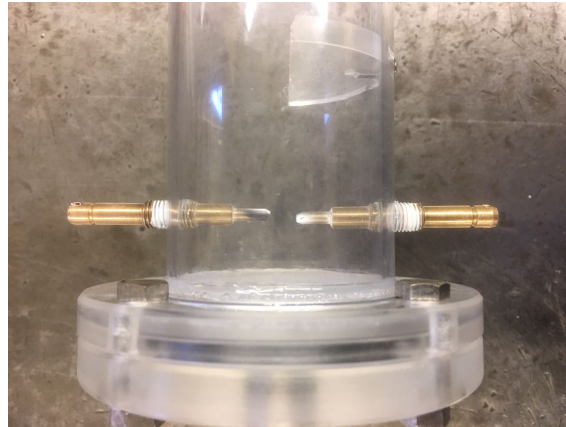
Figure 5.4: Electrical ignition system

5.1.3   Construction

The experimental apparatus consists of a pipe, a flow meter, a compressed air line, a methane cylinder, an electrical ignition, a T&P gauge, a piezoelectric pressure sensor, an HSC, and a computer as indicated in Figure 5.5. The apparatus is placed inside a dark box to avoid any light reflection during the recording. The pipe is fixed on a table so it can not move or shake while the explosions happen.
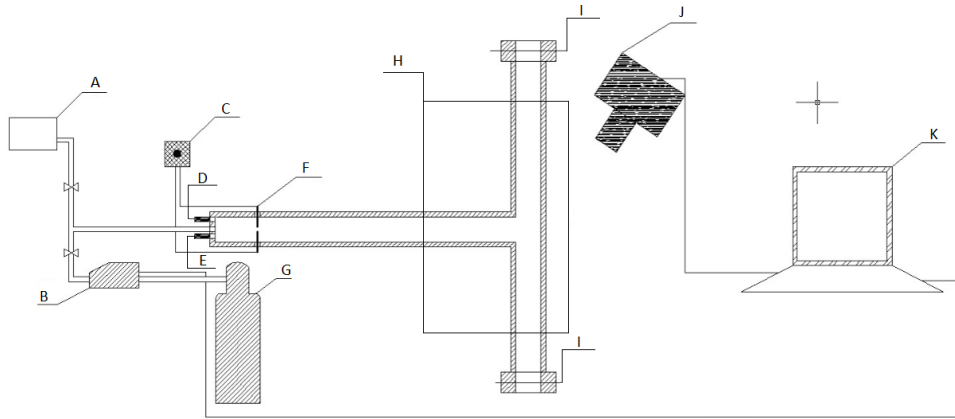
Figure 5.5: Experimental apparatus: (*a*) Compressed air line; (*b*) Flow meter; (*c*) Transformer; (*d*)Piezoelectric pressure sensor; (*e*) T&P gauge; (*f*) Electrical ignition; (*g*) Methane cylinder; (*h*) Record region; (*i*) PET foils; (*j*) HSC; (*k*) Computer

Titanium Dioxide (TiO_2) powder is inserted inside of the pipe to enhance flame propagation so the high-speed camera can collect the frame with high flame image resolution. The TiO_2 is a hydrophobic, thermally stable material, surface treated, and highly insoluble. The product is an ideal seeding material in combustion research due to a nanopowder form with an average size of 4-8 nm and composition $\geq$ 99,9%. The powder is previously dried and a specific amount is inserted into the record region [57, 59]. Tests with Sodium Carbonate (Na_2CO_3) were carried out because these particles have green light emissions, but several tests confirmed that TiO_2 shows better results in this scenario.

5.1.4   Methodology and Limitations

The experiments are planned to be performed in the flammability limit range from lean to rich methane-air concentrations. Each studied equivalence ratio is repeated up to five times. The experimental methodology assures a repeatable experiment performance and results, see Table 5.1. Nevertheless, the methodology is an important pre-condition but does not guarantee identical results [60]. The variation of the parameters monitored on the experiments is expected because it is dealt with inhomogeneous mixtures which contain disordered methane-air mixtures.

Different waiting-times for the methane-air inside of the apparatus are tested and the results remain similar. The minimum waiting-times are 3 minutes for each experiment performed. Several experiments are performed to control the result variation to receive an equivalent result with the same initial setup.

Another challenge of the experiment is the gas leak in the pipe sealer during several explosions. Sometimes the pipe needs maintenance which requires extra time. Despite the limitations, the mixture blended inside of the pipe answers closely to previous calculations with explosion and no-explosion following the limits of flammability. The same methodology is applied to all pipes.

Table 5.1: Laboratory experimental steps

0	For experiments with powder, insert the powder with the specific amount previously calculated at the record region inside of the pipe;
1	Insert compressed air inside of the pipe with the two outlets open to make sure there is only air inside;
2	Install the PET foils in the two outlets section and close the pipe with the scrolls;
3	Insert compressed air to make sure there is no leaking. Visualize the pressure if there is a variation;
4	Release the air until atmospheric pressure;
5	Insert the gaseous methane amount controlled by the flow meter until the equivalence ratio previously calculated;
6	See again if there is any pressure variation to make sure there is no gas leaking;
7	Put the measurement devices in standby and install the ignite conductors;
8	Release the pressure until atmospheric pressure;
9	Initiate the experiment starting respectively the T&P, piezoelectric pressure sensor, HSC and ignite devices.

5.2   Premixed Flame Experimental Results

Image processing techniques from the software ImageJ are used to estimate the flame front average speed and to analyze the flame front stages as well as the turbulent vorticity, behavior, and shape [61]. The flame speed images are separated into section I, II, and III for the two complex geometries. The flame propagation images are analyzed until the outlet PET foils break.

5.2.1   Explosion Maximum Pressure

The piezoelectric pressure sensor is used to monitor the pressure from the explosion until the flame propagation quench. The maximum explosion pressure is the highest pressure during the flame propagation. This pressure varies while the methane concentration increases. The experiments also show variations in the explosion pressure values for methane-air mixtures with the same equivalence ratio. This variation should be caused by the inhomogeneous distribution of the methane-air mixture inside of the apparatus.

An average maximum explosion pressure value is estimated to set the maximum pressure, illustrated in Figure 5.6.
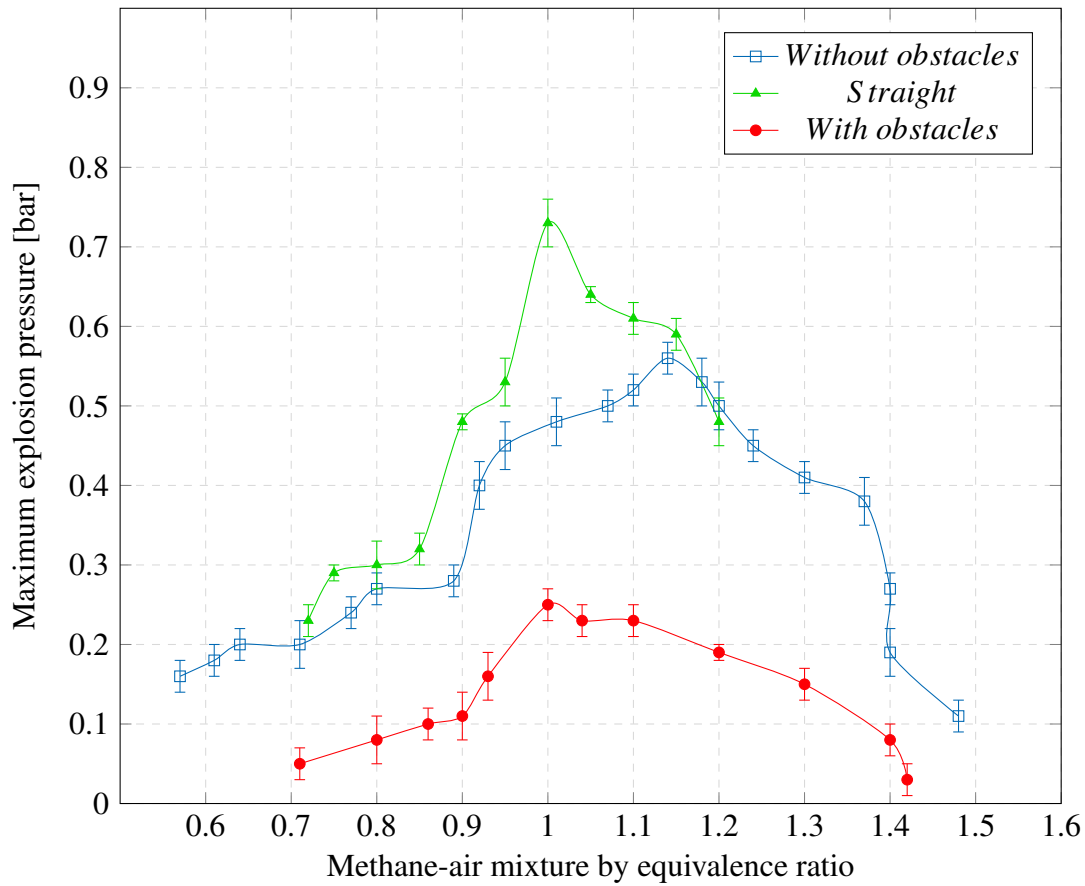
Figure 5.6: Maximum pressure by methane-air concentration

The outlet PET foil is submitted to 5 bar and does not break in this pressure. However, in the experiments, the PET foils break during the flame propagation until the outlet foil even though the maximum explosion pressure is lower than 5 bars.

Wang [62] performed explosion experiments with premixed methane-air with 9.47 % in a half-open tube with 1500 mm length. The system at the outlet was closed by PET foil. Wang analyzed flame propagation in a tube with and without obstacles. Wang's experiment results showed a significant flame speed increase due to the addition of different obstacles. The pressure variation in the experiments without obstacles showed the lowest pressure.

Normally the insertion of the obstacles in a closed system increases the pressure as Wang [62] pointed out. But the scenario exposed in the Figure 5.6 shows the opposite effect where the pressure of the T-pipe with obstacles has lower pressure in comparison to the T-pipe without obstacles.

The highest pressure appears in experiments around the stoichiometric concentration for all three geometries. Mittal und Kund [63, 64] exposed pressure results also with a variation of methane-air concentrations where the highest pressure appeared near the stoichiometric concentration. The explosion pressure of the T-pipe without obstacles had a value scale between the pressure observed for an open system by Guo [65] and for a closed system by Chen

[66], Gieras [67] and Sulaimana [68]. Hong [69] investigated flame propagation with a close system sealed by PET foil. Hong monitored a maximum pressure value between the pressure monitored by the experiments from closed and open outlets of the duct.

The prolonging of the pipes' length increased significantly the maximum explosion. Ajrash [70] experiments dealt with a cylinder tube with 30 m length, an open outlet end, and different active zone as 3, 6, 12, and 25 m. These experiments showed an increase in pressure during the prolonging of the pipe.

The main reason for this phenomenon to appear in a longer pipe is because the propagation needs more time until the flame reaches and breaks the outlet PET foils. Meanwhile, the pressure increases as well. These premixed experiments of a straight geometry do not show explosions over $\Phi = 1.2$ even if the experiments follow the same methodology of the T-pipe. The PET foil provokes a scenario between an open and a closed system because it is closed enough to increase the pressure. But when the propagation reaches the outlet PET foils, the pressure decreases. This is a difficult scenario to be represented in the numerical simulation. The pressure is also analyzed in the numerical simulation results which also show a lower pressure for the simulation using a T-pipe with obstacles.

5.2.2   Premixed Flame Propagation Image Results

The speed is estimated by the flame propagation using the number of frames, the number of fps used in the HSC, and the scale set in the images. The camera records the flame propagation with 8000 fps.

The flame speed is only estimated for some concentrations because the visualization of the flame propagation has not clear image resolution or it does not propagate until the outlet section. The flame speed is estimated based on the flame front which varies during the flame propagation. The speed is estimated for the T-pipes when the flame reached 450 mm until 600 mm in section I. When the flame reaches section II and III, the flame front speed estimation starts from the center region of the T-pipe with a distance of 300 mm for both sides to section II and III. The flame front speed estimation of the straight pipe starts from 100 mm distance of polycarbonate foil and estimation region of 500 mm length of 2000 mm length.

The methane-air reaction happens in the bright region. The unburnt region is represented as the black part in the images. The flame front is the thin region between the bright and black regions. In general, the flame tends to propagate into the direction of the outlet PET foils because it is the region rich in the methane-air mixture. All flame propagation frames results are set up by the time scale $\times 10^{-4}$ s.

5.3   T-pipe without Obstacles

The flame propagation images from the T-pipe experiments are separated by the mixture concentration represented by the equivalence ratio. Based on the resolution of the collected images, a selection of experimental results is taken. The experiments performed with lean mixtures are $\Phi = 0.57$, 0.62, 0.71, 0.80 and 0.89. The stoichiometric mixture is $\Phi = 1.0$. And the rich mixtures are $\Phi = 1.08$ and 1.19. Each concentration is repeated up to five times

to collect flame propagation images with high quality. Some of the concentrations do not support a clear visualization of images recorded with the HSC. Even though an explosion is obtained by the piezoelectric pressure sensor as observed in the maximum pressure, see Figure 5.6.

The flame propagation images of $\Phi = 0.57$, $\Phi = 0.62$, $\Phi = 0.8$, $\Phi = 1.0$, $\Phi = 1.08$ and $\Phi = 1.19$ are improved to gain a better resolution by image processing techniques *brightness*'s and *black-white*. The images of $\Phi = 0.71$ and $\Phi = 0.89$ are exposed as the original image collected by the high-speed camera. Figure 5.7, Figure 5.8 and Figure 5.9 show the flame propagation in section I of the lean mixtures.
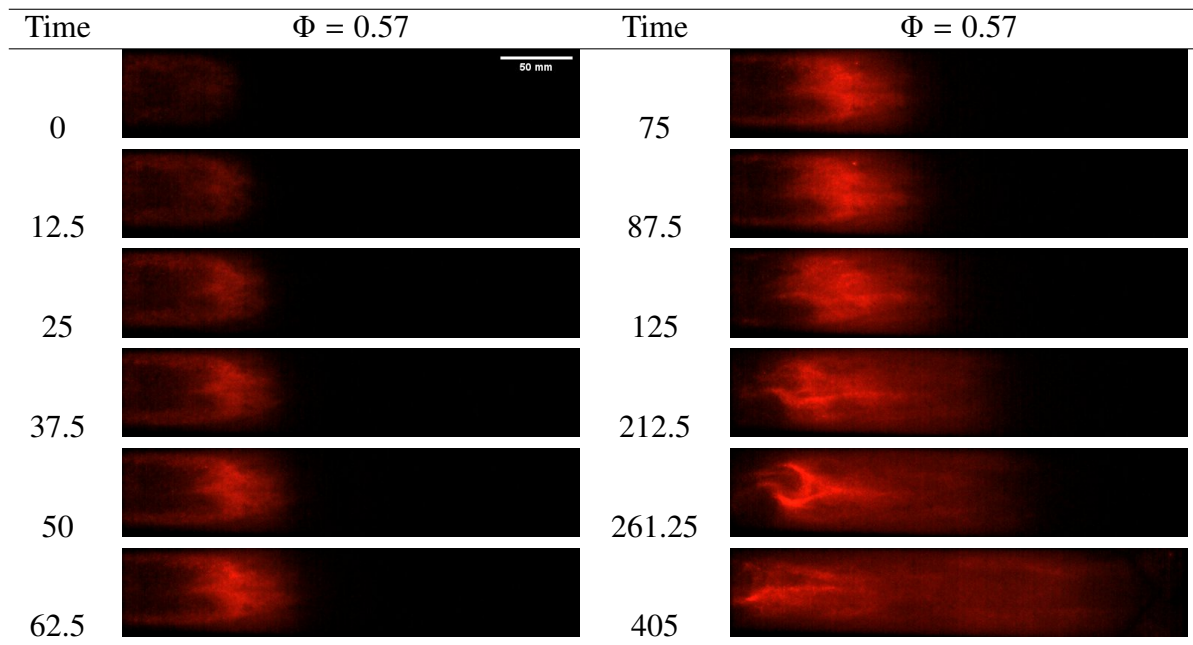
Time	$\Phi = 0.57$	Time	$\Phi = 0.57$
0		75	
12.5		87.5	
25		125	
37.5		212.5	
50		261.25	
62.5		405	

Figure 5.7: Flame propagation images of T-pipe in section I of a mixture with $\Phi = 0.57$

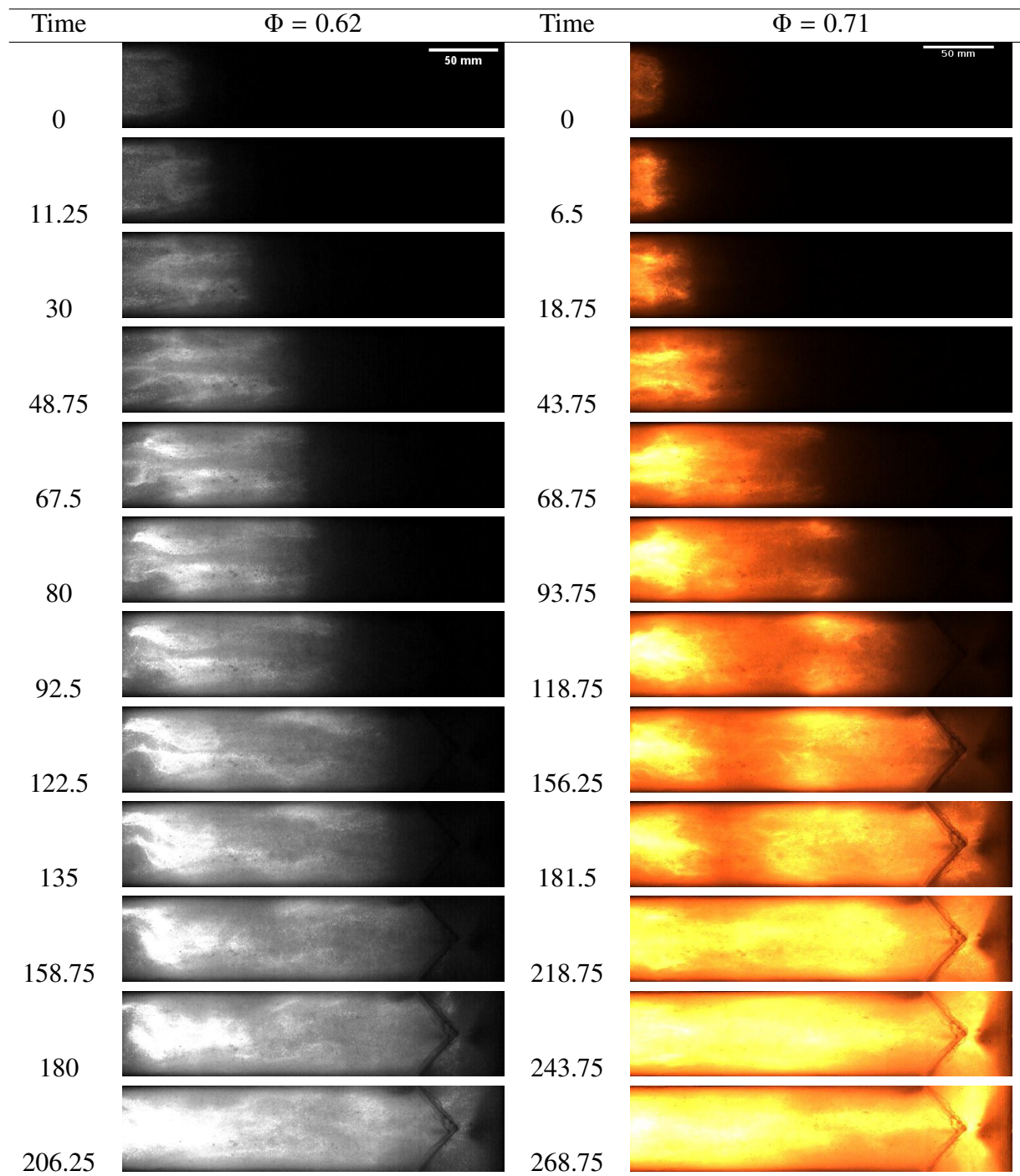| Time	Φ = 0.62	Time	Φ = 0.71
0		0	
11.25		6.5	
30		18.75	
48.75		43.75	
67.5		68.75	
80		93.75	
92.5		118.75	
122.5		156.25	
135		181.5	
158.75		218.75	
180		243.75	
206.25		268.75	

Figure 5.8: Flame propagation images of T-pipe in section I of mixtures with Φ = 0.62 and 0.71
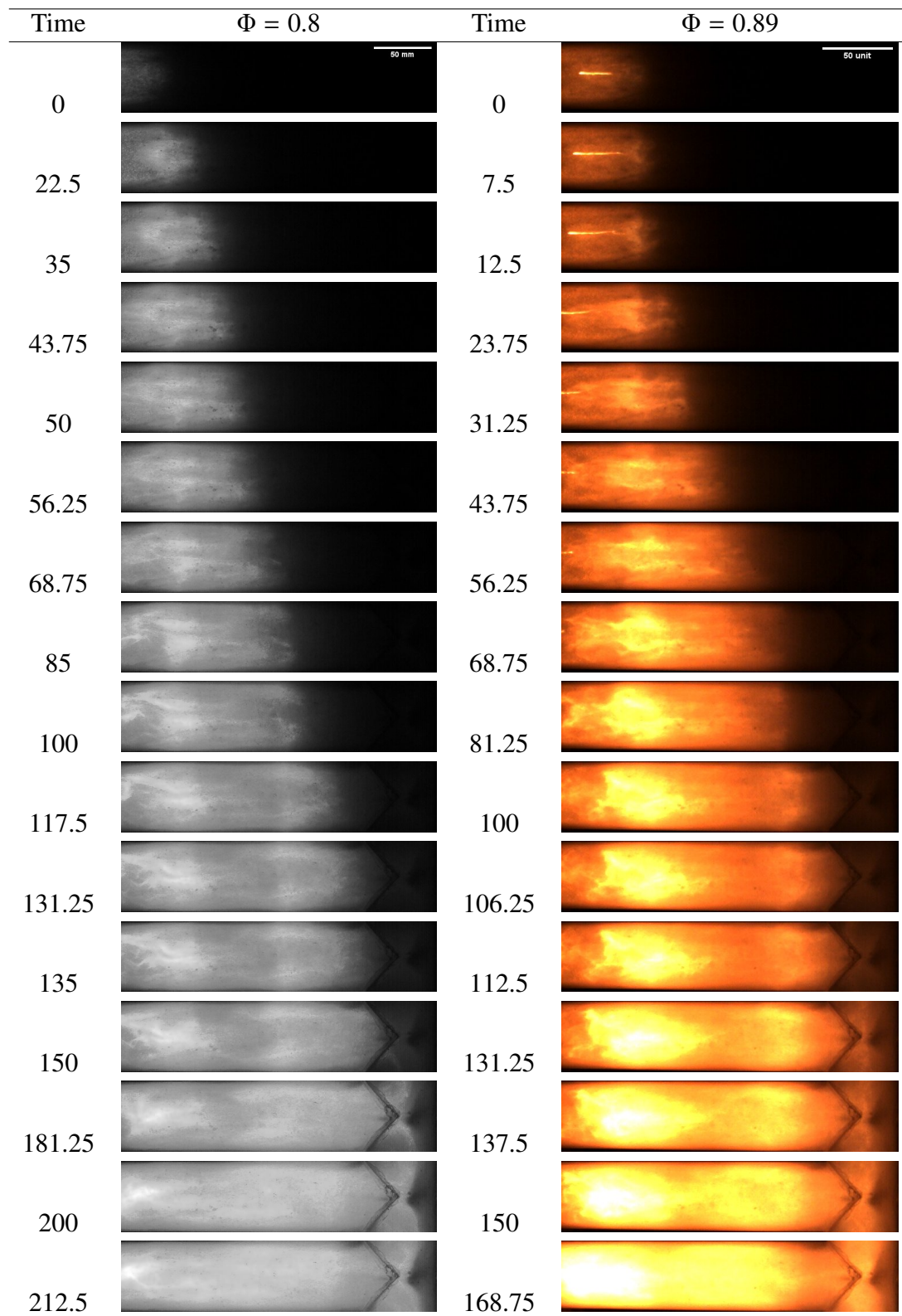
Figure 5.9: Flame propagation images of T-pipe in section I of mixtures with Φ = 0.8 and 0.89

The flame propagation of the lean mixtures presented on the previous in Figure Figure 5.7, Figure 5.8 and Figure 5.9 is detailed by time.

- The selected flame images start with an hemispherical flame front expansion at time 0 s for $\Phi = 0.57, 0.62, 0.71, 0.8$, and 0.89.

- The flame front starts a change from hemispherical to a finger-shaped formation at the time 12.5 s for $\Phi = 0.57$, 11.25 s for $\Phi = 0.62$, 6.5 s for $\Phi = 0.71$, 22.5 s for $\Phi = 0.8$ and 7.5 s for $\Phi = 0.89$. At this moment, reverse propagation occurs in the region behind the flame front.

- An elongation of the finger-shaped starts and the flame front becomes affected at the time 125 s for $\Phi = 0.57$, 48.75 s for $\Phi = 0.62$, 43.75 s for $\Phi = 0.71$, 43.75 s for $\Phi = 0.8$ and 23.75 s for $\Phi = 0.89$.

- The "Tulip Flame" [12] happens at the time 212.5 s for $\Phi = 0.57$, 67.5 s for $\Phi = 0.62$, 93.75 s for $\Phi = 0.71$, 68.75 s for $\Phi = 0.8$ and 43.75 s for $\Phi = 0.89$.

- A reverse propagation continues behind the flame front and observed at the time 405 s for $\Phi = 0.57$, 122.5 s for $\Phi = 0.62$, 118.75 s for $\Phi = 0.71$, 100 s for $\Phi = 0.8$ and 81.25 s for $\Phi = 0.89$.

- The flame propagation with $\Phi = 0.57$ does not support a clear visualization after this time. Although, the experiments with $\Phi = 0.62$, $\Phi = 0.71$, $\Phi = 0.8$ and $\Phi = 0.89$ show a flame front propagation where an elongation by side starts. This elongation closes at the time 135 s for $\Phi = 0.62$, 181.5 s for $\Phi = 0.71$, 131.25 s for $\Phi = 0.8$ and 106.25 s for $\Phi = 0.89$. The flame front formation continues to propagate in the direction of the bent region.

- After the closure of the flame front, the second reverse propagation starts behind the flame front and reaches the first reverse propagation at the time 206.25 s for $\Phi = 0.62$, 243.75 s for $\Phi = 0.71$, 200 s for $\Phi = 0.8$ and 168.75 s for $\Phi = 0.89$.

The flame propagation in section II and III does not have a clear image resolution for the mixture with $\Phi = 0.57$. Figure 5.10 and Figure 5.11 show a flame propagation in section II and III for mixture $\Phi = 0.62$ and $\Phi = 0.71$, respectively.
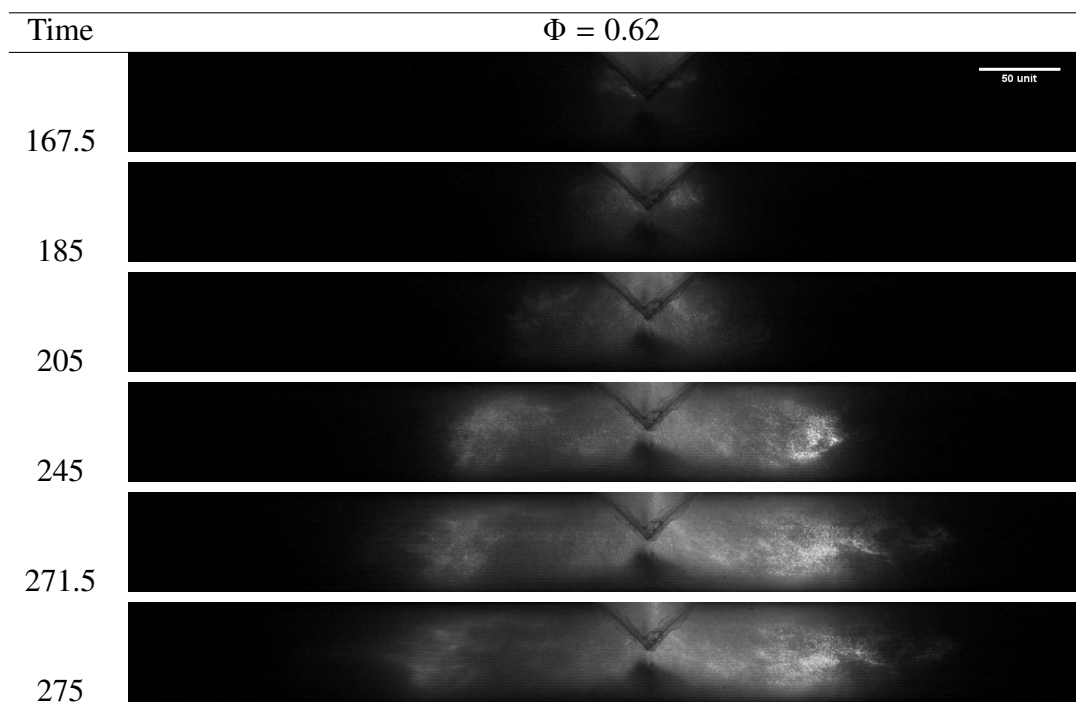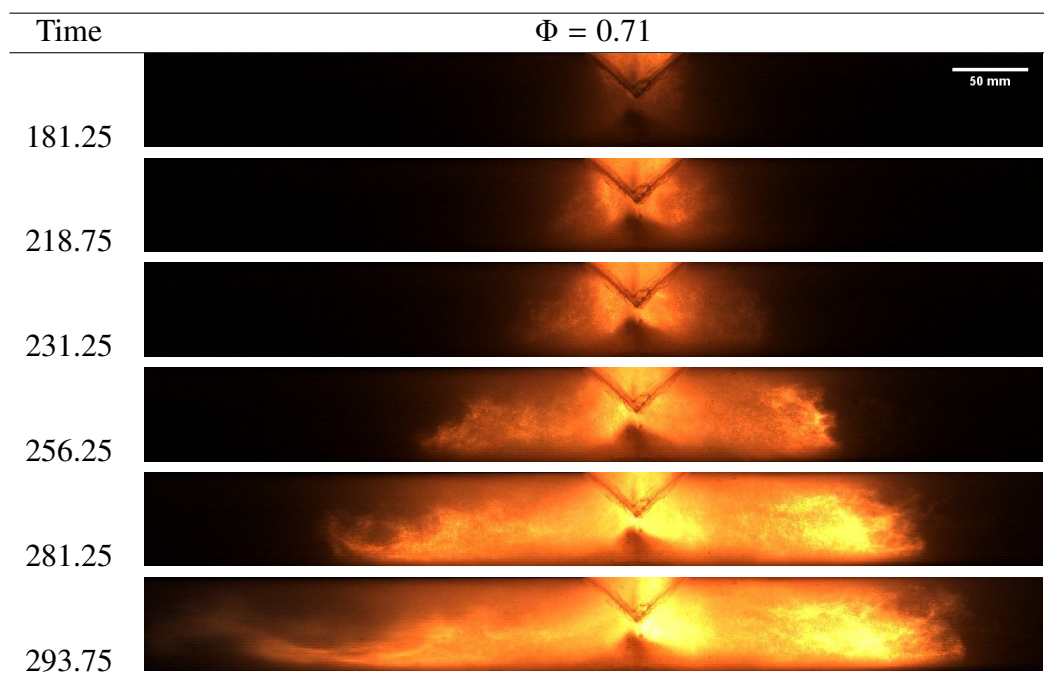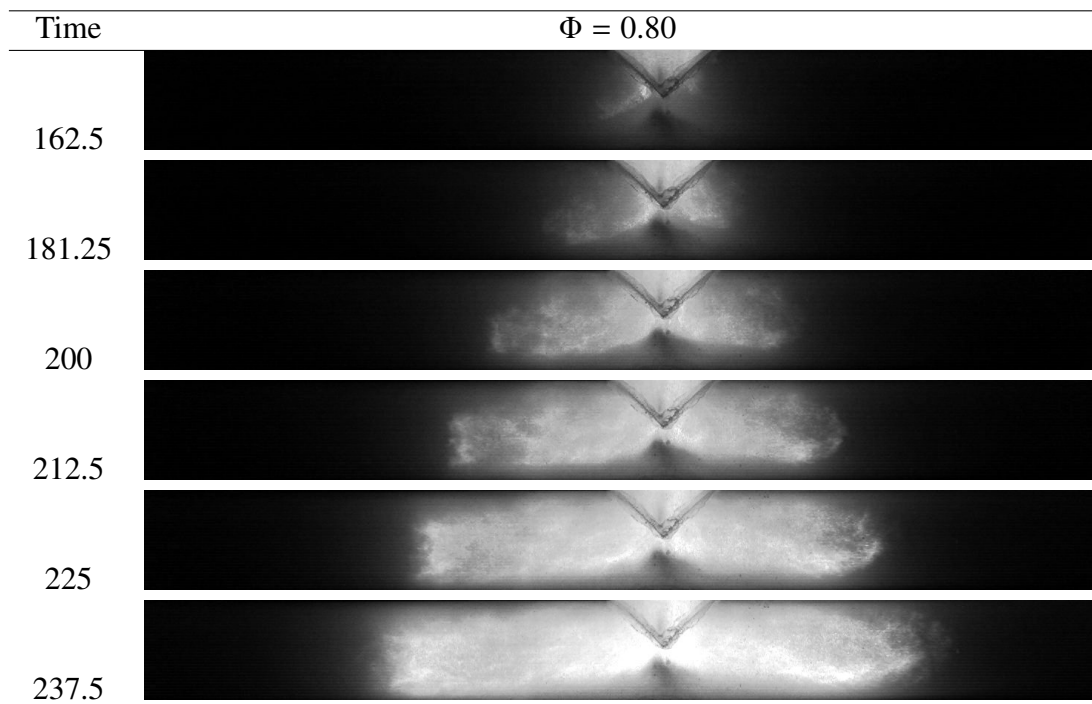
Time	Φ = 0.62

Figure 5.10: Flame propagation image of T-pipe in section II and III of a mixture with Φ = 0.62

Time	Φ = 0.71

Figure 5.11: Flame propagation image of T-pipe in section II and III of a mixture with Φ = 0.71

Time	Φ = 0.80
162.5	
181.25	
200	
212.5	
225	
237.5	

Figure 5.12: Flame propagation images of T-pipe in section II and III of a mixture with Φ = 0.80

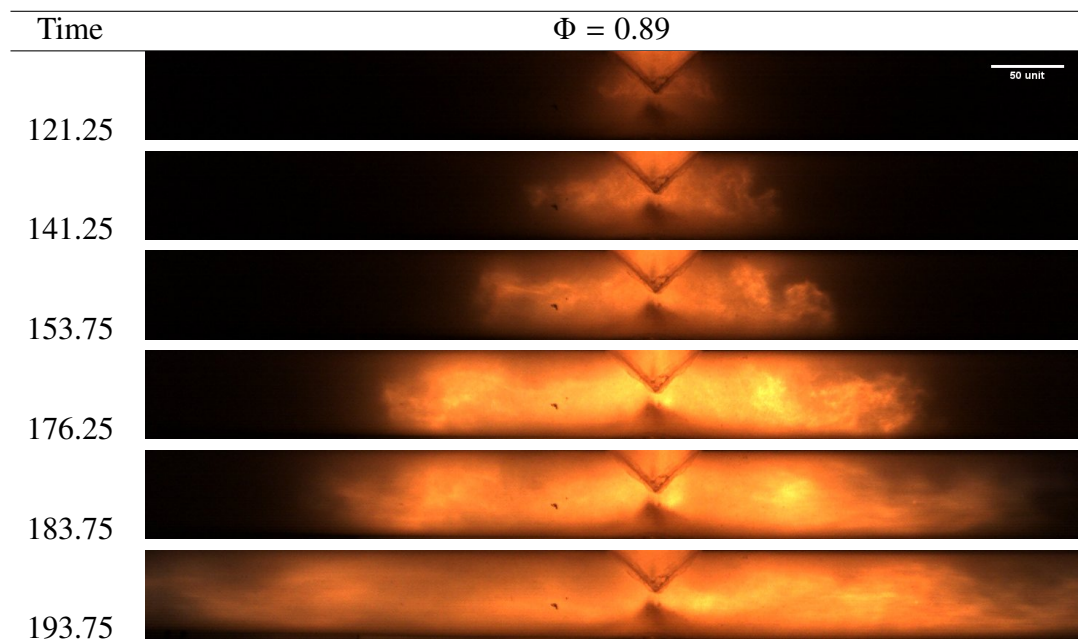| Time	Φ = 0.89
121.25	
141.25	
153.75	
176.25	
183.75	
193.75	

Figure 5.13: Flame propagation images of T-pipe in section II and III of a mixture with Φ = 0.89

The flame propagation has equivalent flame speed for both directions at the bent region until the moment one of the outlet foil breaks. There is a vorticity formation near the bent region which can be observed in the flame front of both sides. The outlet foil breaks at the time 271.5 s for $\Phi = 0.62$, 293.75 s for $\Phi = 0.71$, 237.5 s for $\Phi = 0.8$ and 183.75 s for $\Phi = 0.89$. The pressure is released after the outlet foil breaks and the flame speed propagation increases at the same time.

The outlet foils break before the flame front touches the outlet foil and with a pressure lower than 5 bar. One explanation is the flame heats the unburned methane-air, and this hot mixture melts and breaks the PET foils of the outlet.

The flame front does not have a shape formation and the flame tends to propagate near the lower part of the wall. There is a divided region formed between the left and right sides of the flame at the bent region as shows Figure 5.14. A similar phenomenon happens with further methane-air concentration.
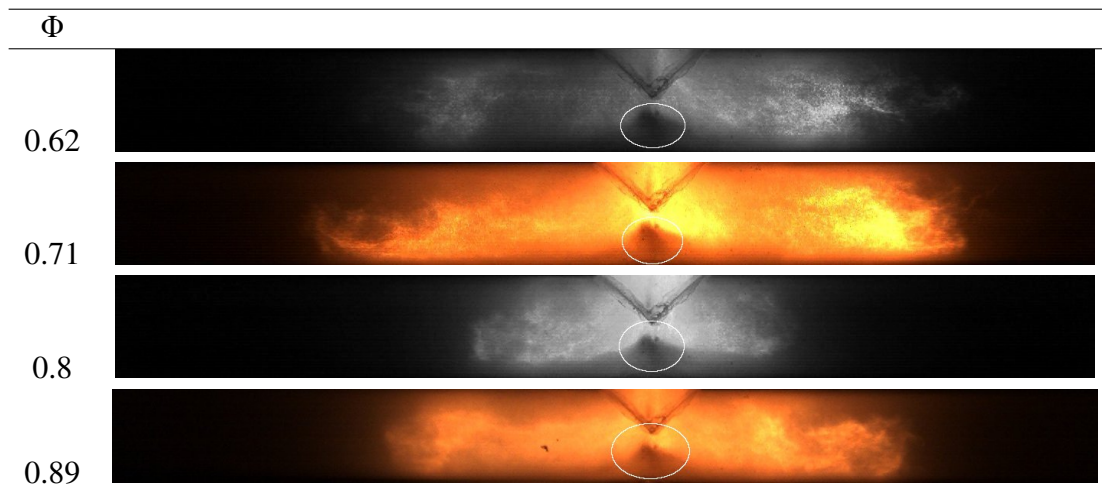

Figure 5.14: Flame propagation image in section II and III

The stoichiometric mixture experiment has a flame propagation as shown in Figure 5.15 for section I and Figure 5.16 for section II and III.
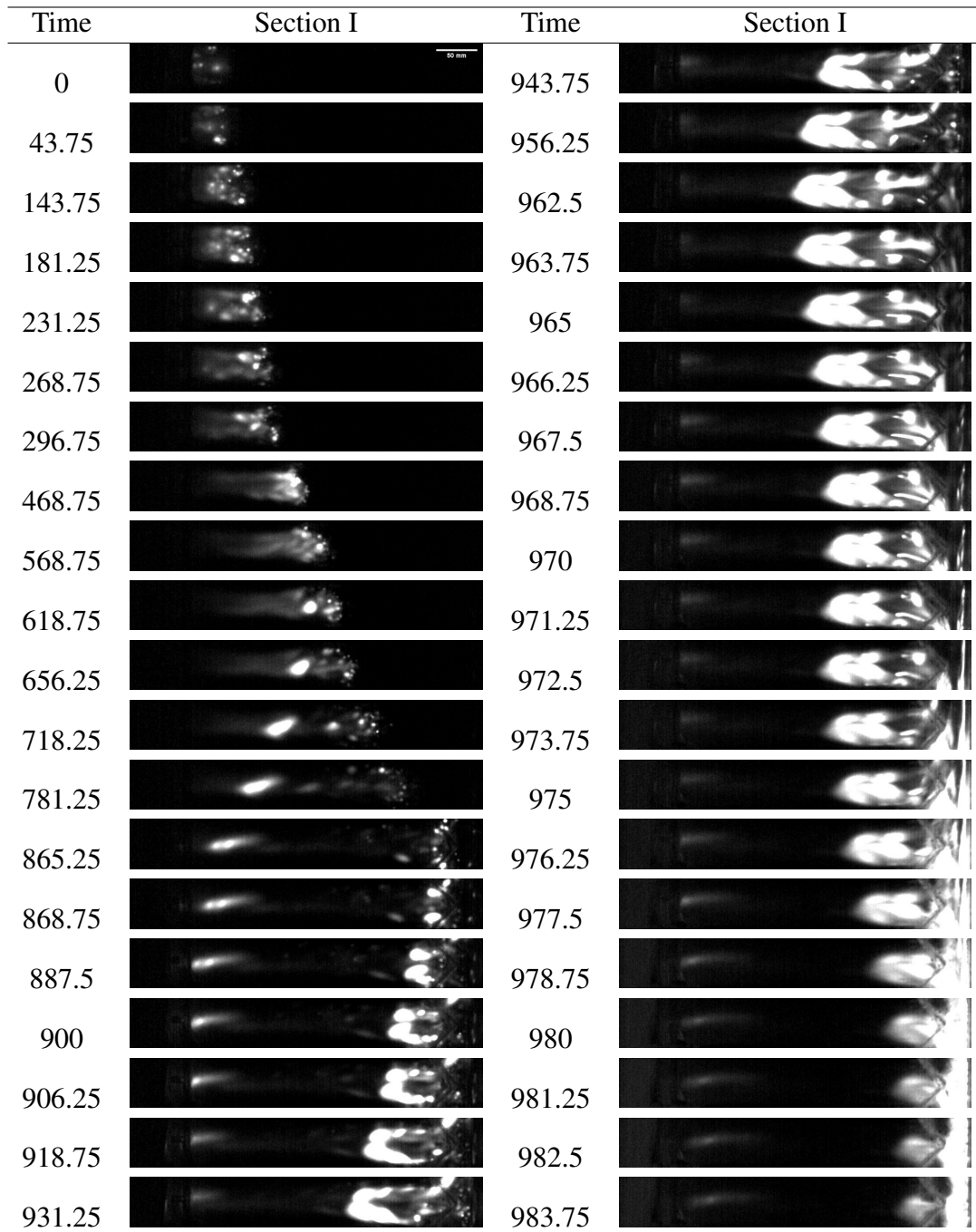
Time	Section I	Time	Section I
0		943.75	
43.75		956.25	
143.75		962.5	
181.25		963.75	
231.25		965	
268.75		966.25	
296.75		967.5	
468.75		968.75	
568.75		970	
618.75		971.25	
656.25		972.5	
718.25		973.75	
781.25		975	
865.25		976.25	
868.75		977.5	
887.5		978.75	
900		980	
906.25		981.25	
918.75		982.5	
931.25		983.75	

Figure 5.15: Flame propagation images of T-pipe in section I of a mixture with $\Phi = 1.0$

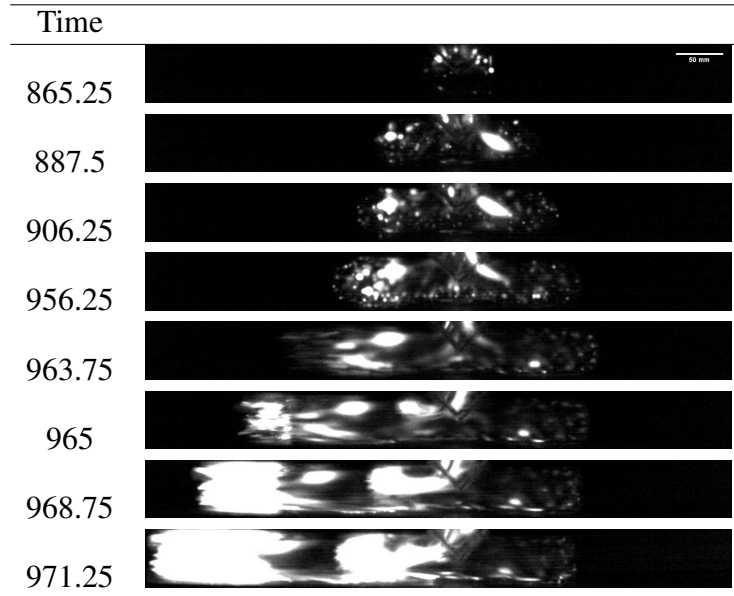| Time |
|------|
| 865.25 |
| 887.5 |
| 906.25 |
| 956.25 |
| 963.75 |
| 965 |
| 968.75 |
| 971.25 |

Figure 5.16: Flame propagation images of T-pipe in section II and III of a mixture with Φ= 1.0

The flame propagation of a stoichiometric mixture presented on the previous in Figure Figure 5.15 and Figure 5.16 is detailed by time.

- The hemispherical flame front expansion starts at time 0 s.

- The flame front starts a change from hemispherical to a finger-shaped formation during the time 43.75 s until 143.75 s. It starts a reverse propagation in the region behind the flame front.

- An elongation of the finger-shaped starts during the time 143.75 s until 268.75 s.

- The "Tulip Flame" [12] happens at the time 296.75 s.

- A reverse propagation continues behind the flame front and observed at the time 656.25 s.

- The flame front propagation starts a second elongation by side during the time 718.25 s until 868.75 s. These elongations close at the time 887.5 s and initiate a second reverse propagation behind the flame front.

- A flame front formation continues the forward propagation in the direction of the bent region. The second reverse propagation propagates in the direction of the first reverse propagation during the time 900 s until 956.255 s. At this time 956.255 s the outlet foil breaks and the reverse propagation changes the direction and propagates forward.

The flame propagation in section II and III is fast and does not have a clear visualization. The flame propagates for both direction with equivalent speed and a vorticity formation is also visualized in the flame front.

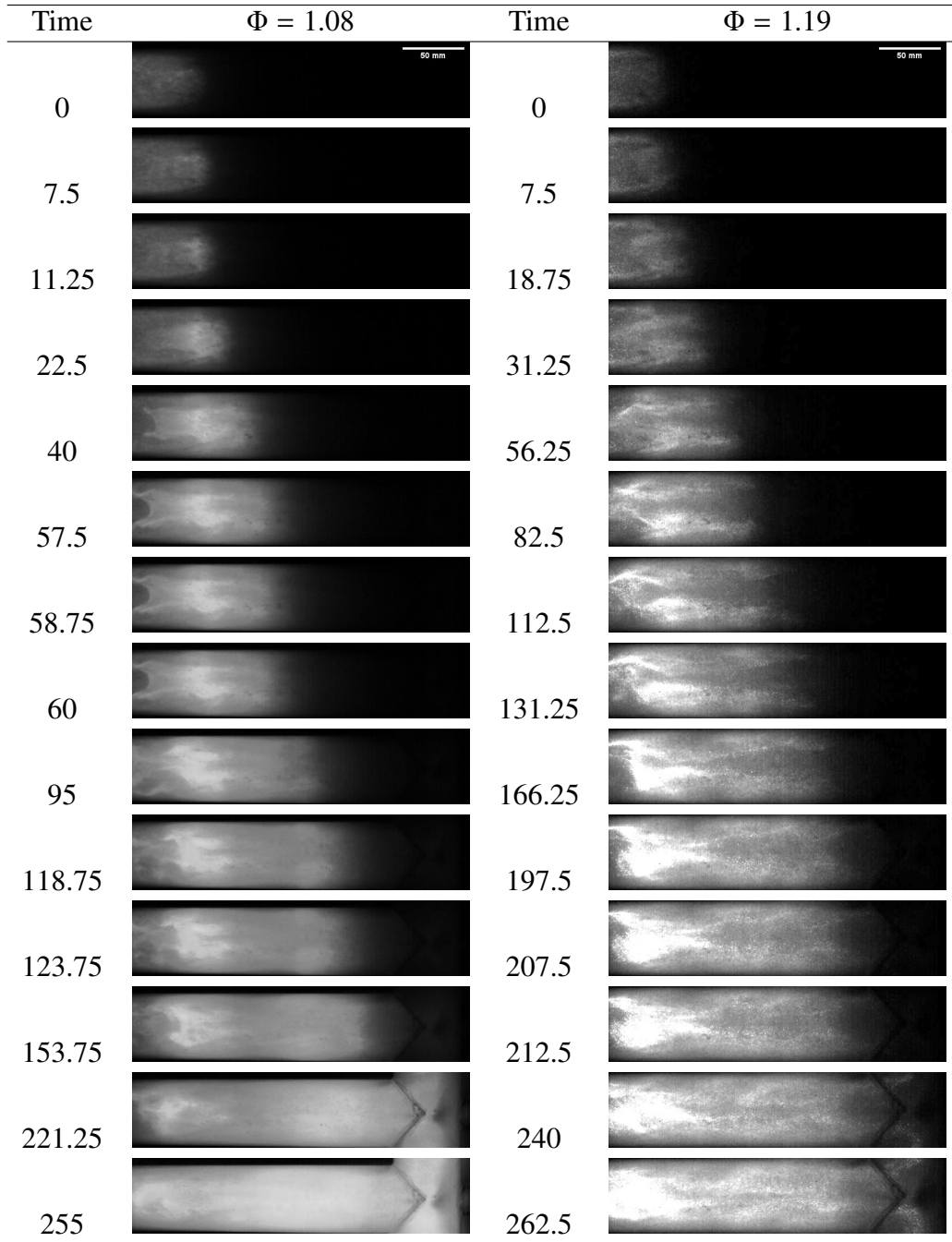Figure 5.17 shows the flame propagation at section I of the rich mixtures.

Figure 5.17: Flame propagation images of T-pipe in section I of mixtures with $\Phi = 1.08$ and 1.19

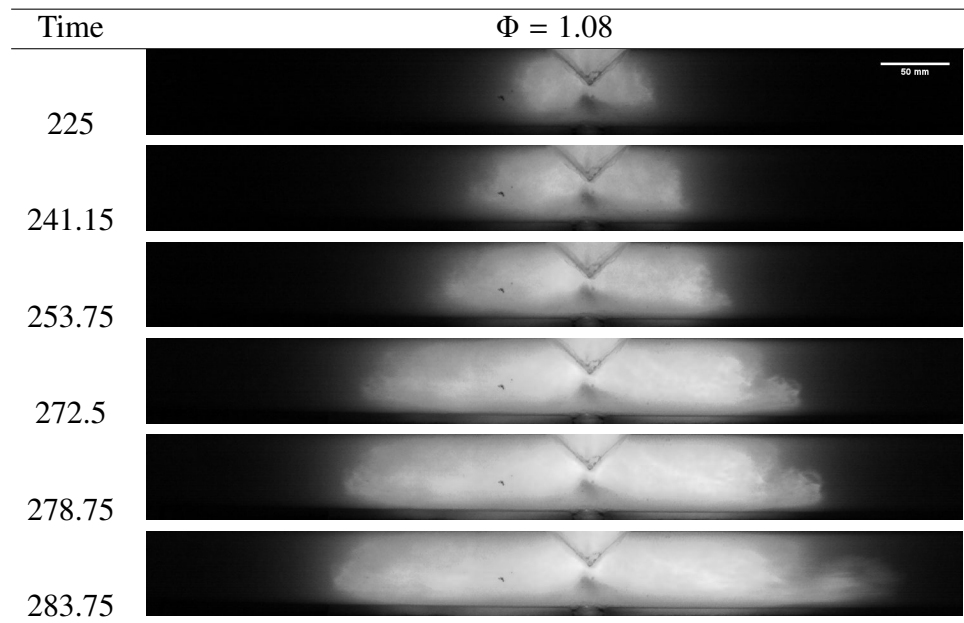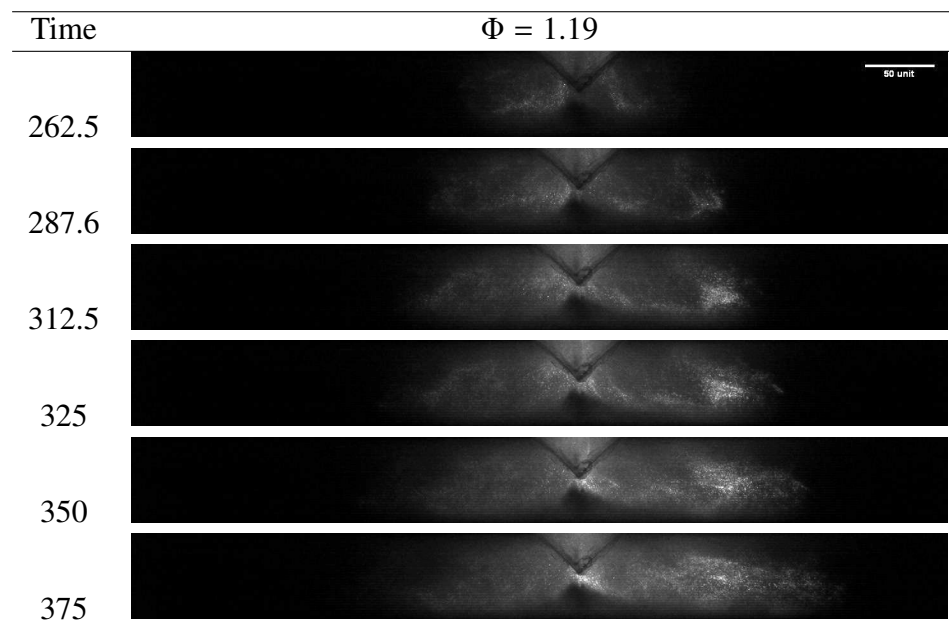Figure 5.18 and Figure 5.19 show a flame propagation in section II and III of the rich mixtures.

Time	Φ = 1.08
225	
241.15	
253.75	
272.5	
278.75	
283.75	

Figure 5.18: Flame propagation images of T-pipe in section II and III of a mixture with Φ = 1.08

Time	Φ = 1.19
262.5	
287.6	
312.5	
325	
350	
375	

Figure 5.19: Flame propagation images of T-pipe in section II and III of a mixture with Φ = 1.19

The flame propagation of the rich mixtures presented on the previous in Figure 5.17, Figure 5.18 and Figure 5.19 is detailed by time.

- The selected flame images start with a hemispherical flame front expansion at time 0 s for Φ = 1.08 and 1.19.

- The flame front starts a change from hemispherical to a finger-shaped formation at the time 11.25 s for Φ = 1.08 and 7.5 s for Φ = 1.19. It starts a reverse propagation in the region behind the flame front.

- An elongation of the finger-shape begins at the time 40 s for Φ = 1.08 and 31.25 s for Φ = 1.19.

- The "Tulip Flame" [12] happens at the time 57.5 s for Φ = 1.08 and 56.25 s for Φ = 1.19.

- A reverse propagation continues behind the flame front and another elongation by side initiating is observed at the time 58.75 s for Φ = 1.08 and 82.5 s for Φ = 1.19.

- This elongation closes at the time 123.75 s for Φ = 1.08 and 207.5 s for Φ = 1.19. And the flame front formation continues the forward propagation near in the direction of the bent region.

- After the closure, the second reverse propagation starts behind the flame front and reaches the first reverse propagation at the time 221.25 s for Φ = 1.08 and 240 s for Φ = 1.19.

- The outlet PET foils break at the time 283.75 s for Φ = 1.08 and 375 s for Φ = 1.19.

Table 5.2 illustrates the flame propagation stages observed in the experiments. The stages are defined by the flame shape and propagation. Stage 1 designates the hemispherical expansion. Stage 2 is called a hemispherical finger-shaped flame and a reverse propagation occurs behind the flame front. Stage 3 describes the elongation of the finger-shape. Stage 4 is called the "Tulip Flame". In stage 5 occurs a new elongation of the flame front. Stage 6 starts the closure of the second elongation and a second reverse propagation initiates behind the flame front. Stage 7 happens when the second elongation closes and the second reverse propagation reaches the first reverse propagation. Stage 8 is not a flame propagation stage, it just indicates the moment the PET foils in section II and III break.

Table 5.2: Flame propagation stages by frame time

Φ	Stage 1	Stage 2	Stage 3	Stage 4	Stage 5	Stage 6	Stage 7	Stage 8
0.57	0	12.5	125	212.5	405	-	-	-
0.62	0	11.5	48.5	67.5	122.5	135	206.5	271.5
0.71	0	6.5	43.75	93.75	118.75	181.5	243.75	293.75
0.8	0	22.5	43.75	68.75	100	131.25	200	237.5
0.89	0	7.5	23.75	43.75	81.25	106.25	168.75	183.75
1.0	0	43.75	143.75	296.75	656.25	887.5	900	956.255
1.08	0	11.25	40	57.5	58.75	123.75	221.5	283.75
1.19	0	7.5	31.25	56.25	82.5	207.5	240	375

The addition of TiO_2 supports a clear flame visualization, especially in the region behind the flame front which presents the flame propagation with more details. The analysis of these stages described in Table 5.2 is discussed in detail in the following sub-chapter.

The bent region provokes a deviation in the flame propagation. The flame loses the flame front shape when it crosses the bent region and propagates faster in comparison to section I. A short reverse propagation occurs near the bent region and an elongation happens near the wall of section II and III. This flame behavior is repeated for several experiments with different and same methane-air concentrations.

The average flame speed collected from the experiments is estimated by image processing tools only in the equivalence ratios where it is possible to visualize the flame propagation, see Figure 5.20. With this technique, a scale is set at the image base in radius size to observe the flame front propagation for each frame time and to estimate the flame speed by a length with the number of frames.
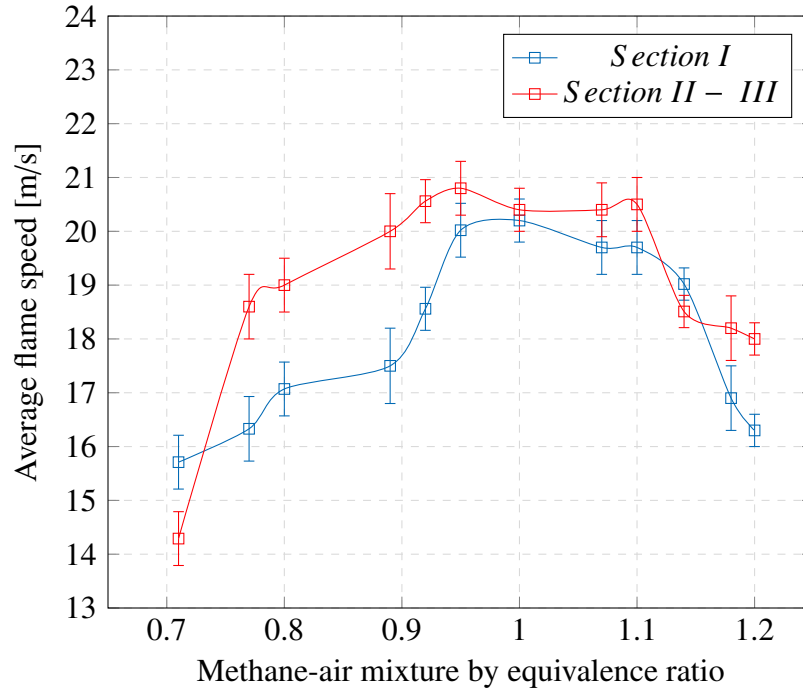
Figure 5.20: premixed flame speed of T-pipe by methane-air concentration

The flame speed increases and decreases during the variation of the methane-air concentrations from lean to rich mixture. The highest flame front speed appears near to stoichiometric concentration. The laminar flame speed collected in cantera and the flame propagation from experiments of Mittal und Kundu [63, 64] show similar flame speed variation during the increase of methane in the premixed.
The bent region provokes an increase of the flame speed as shown Figure 5.20 for most of the methane-air concentrations.

5.3.1 Premixed Flame Propagation Stages

Clanet and Searby [12] proposed four stages for the flame propagation of premixed flames: (a) hemispherical expansion flame unaffected by the side walls; (b) a finger-shaped flame; (c) an elongated flame with the skirt touching the sidewalls; and (d) a "Tulip Flame". Their experiments of flame propagation are carried out in a straight pipe with an open outlet. Premixed propane-air in the range of $0.65 < \Phi < 1.3$ in a tube with 2.5 and 5 cm radius and the lengths ranging from 0.6 m to 6 m is employed.
The premixed flame experiment performed in this work using the T-pipe without powder shows similar stages like the ones proposed by Clanet and Searby, see Figure 5.21. The images of flame propagation without powder do not show clearly what happens in the burnt part behind the flame front.
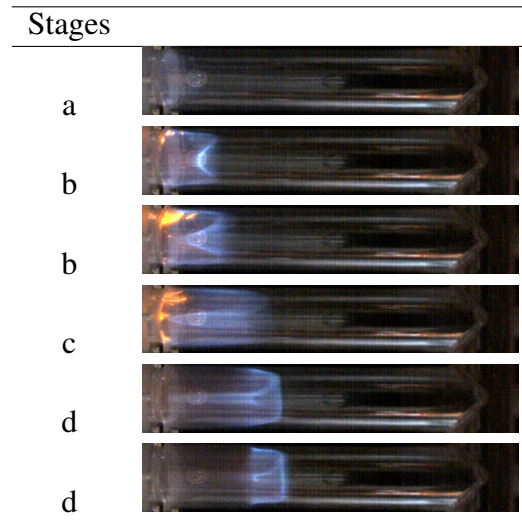
Figure 5.21: Flame propagation of T-pipe of a mixture with $\Phi = 1.2$ without TiO_2 powder

The evaluation of the flame frames from premixed flame experiments with TiO_2 powder shows the flame behavior behind the flame front. Different stages and some modifications are proposed based on Clanet's and Searby's work [12], but for the outlet closed by PET foils. The frames in Figure 5.22 are presented by the frames in Figure 5.8 with $\Phi = 0.71$ using the image processing tool *Find Edges* [61]. This tool is used for a better resolution of the eight proposed stages and it can show the different regions inside of the flame, see Figure 5.22.
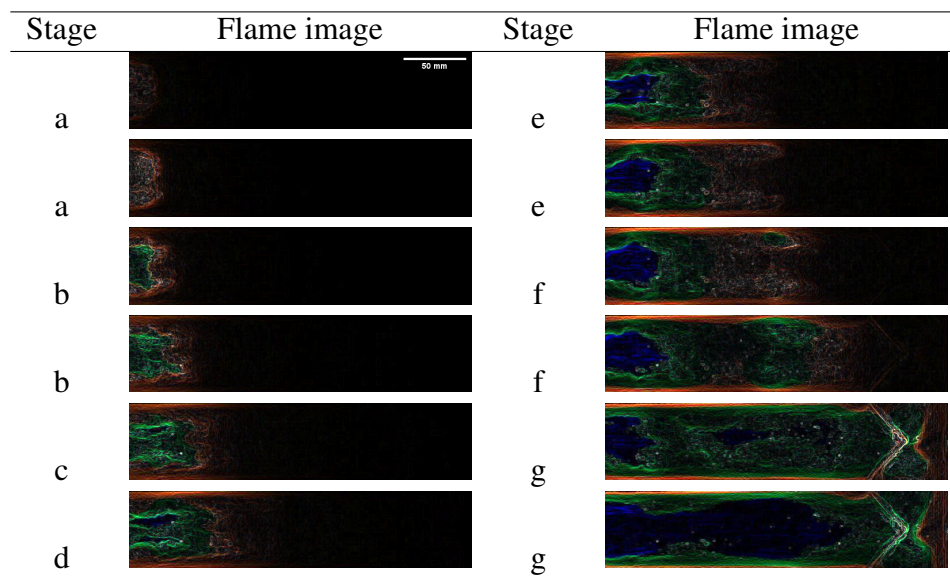
Figure 5.22: Flame propagation of T-pipe of a mixture with $\Phi = 0.71$ with TiO_2 powder

The flame tends to propagate from the left to the right. The green zone propagates in the right direction and the blue zone propagates in the left direction. The bent region is at the end of the right part. The flame propagation shown in Figure 5.22 is divided into seven stages.

(a) The first stage designates the hemispherical expansion.

(b) The second stage refers similarly to the hemispherical finger-shaped flame represented by the green zone. A reverse propagation starts being represented by the blue zone in the region behind the flame front.

(c) The third stage includes the elongation of the finger-shaped flame where the flame front becomes affected. A flame stretches on the sides is represented by the green zone. Illustrated by the blue zone, the reverse propagation continues behind the flame front.

(d) In the fourth stage, "Tulip Flame" occurs and the flame front elongation is represented by the green zone. And a reverse propagation continuing in the region behind the flame front which it is represented by the blue zone.

(e) The fifth stage displays the reverse propagation behind the flame front which is represented by the blue zone. And another elongation by side initiates which can be observed by the green zone.

(f) In the sixths stage, the elongation of the flame is beginning to close, which is demonstrated by the green zone. The beginning of the second reverse propagation behind the flame front can be observed by the blue zone in the center.

(g) The seventh stage designates the time the frame front already closed. The second reverse propagation approaches the first reverse propagation. This reverse propagation is represented by the blue zone. The flame front continues the propagation into section II and III.

The major difference of this work in comparison to Clanet's and Searby's findings concern the region behind the flame front, as well as the flame directions and cycles.

5.3.2   Straight Pipe

The stages proposed in the subchapter before are observed in the experiments performed with a straight pipe. The T-pipe has a short straight section which does not show clearly the two

reverse propagation. Hence a pipe with 2000 mm length is used where a 500 mm section with 100 mm distance of the polycarbonate foil is recorded. The flame speed is estimated from the 500 mm region image. The flame propagation is an extension of the phenomenon from section I of the T-pipe without obstacles as illustrated in Figure 5.23.
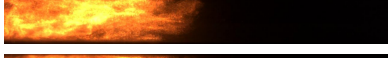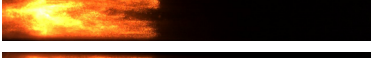
Time	Φ = 0.75	Time	Φ = 0.95
0		0	
12.5		31.25	
28.75		56.25	
37.5		68.75	
53.75		81.25	
62.5		93.75	
75		100	
93.75		118.75	
112.5		125	
125		131.25	
131.25		137.5	
142.5		156.25	
152.5		165	
167.5		171.25	
172.5		182.5	
176.25		187.5	
181.25		193.75	
187.5		200	

Figure 5.23: Flame propagation images in straight pipe of mixtures with Φ = 0.75 and 0.95

During the flame propagation appears the first reverse propagation behind the flame front in the frame time 131.25 s until 167.5 s for Φ = 0.75 and the second reverse propagation in the frames 165 s until 182.5 s for Φ = 0.95, see Figure 5.23. This reverse propagation provokes two different propagation cycles with a different speed which also occurs for different concentrations as for the T-pipe.

The flame speed is estimated for these two cycles shown in Figure 5.24. The flame speed from cycle I demonstrates an increase of velocity in comparison to the T-pipe. After the reverse propagation in cycle I, the flame starts cycle II and the flame speed increases radically.
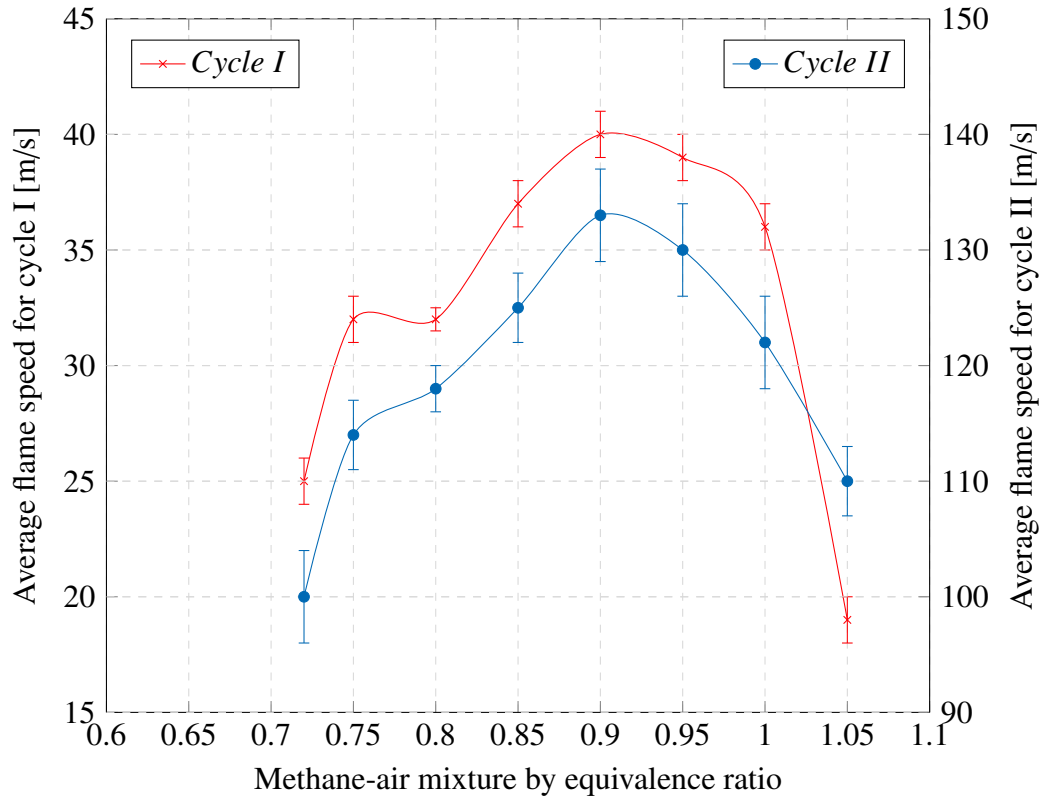
Figure 5.24: Premixed flame speed of straight pipe by methane-air concentration

The flame speed has an increase of around 380% of the flame front speed from cycle I to cycle II for most of the methane-air concentrations. Ajrash's [70] experiments showed the growth of flame speed during the propagation as well. Ajrash's experiment has a 3 m active zone, which shows an increase of the flame speed but the flame speed magnitude is lower in Ajrash's experiments because the pipe is open at the outlet.

5.4 T-pipe with Obstacles

The flame propagation images from the T-pipe with obstacles experiments are also separated by lean, stoichiometric, and rich fuel-air rate concentrations. The images monitored by the HSC are available to estimate the flame speed using image processing techniques. Though the flame propagation does not show a high-quality image resolution for all concentrations. Thus some image processing techniques offer a brightness and color adjustment to have a high-quality image resolution.

The images selected of the lean mixtures are $\Phi = 0.70$, 0.75 and 0.84. The images of concentrations around the stoichiometric mixture are $\Phi = 0.98$ and 1.0. And the rich mixtures are $\Phi = 1.1$ and 1.22.

The lean mixtures are presented in Figure 5.25 and Figure 5.26 for section I. Figure 5.27, Figure 5.28 and Figure 5.29 show the results for section II and III. The images result of $\Phi = 0.84$ has an image processing improvement with the *brightness*'s tool by ImageJ. The results with $\Phi = 0.70$ and 0.75 do not show any improvement.

Figure 5.25: Flame propagation image of T-pipe in section I of a mixture with $\Phi = 0.70$
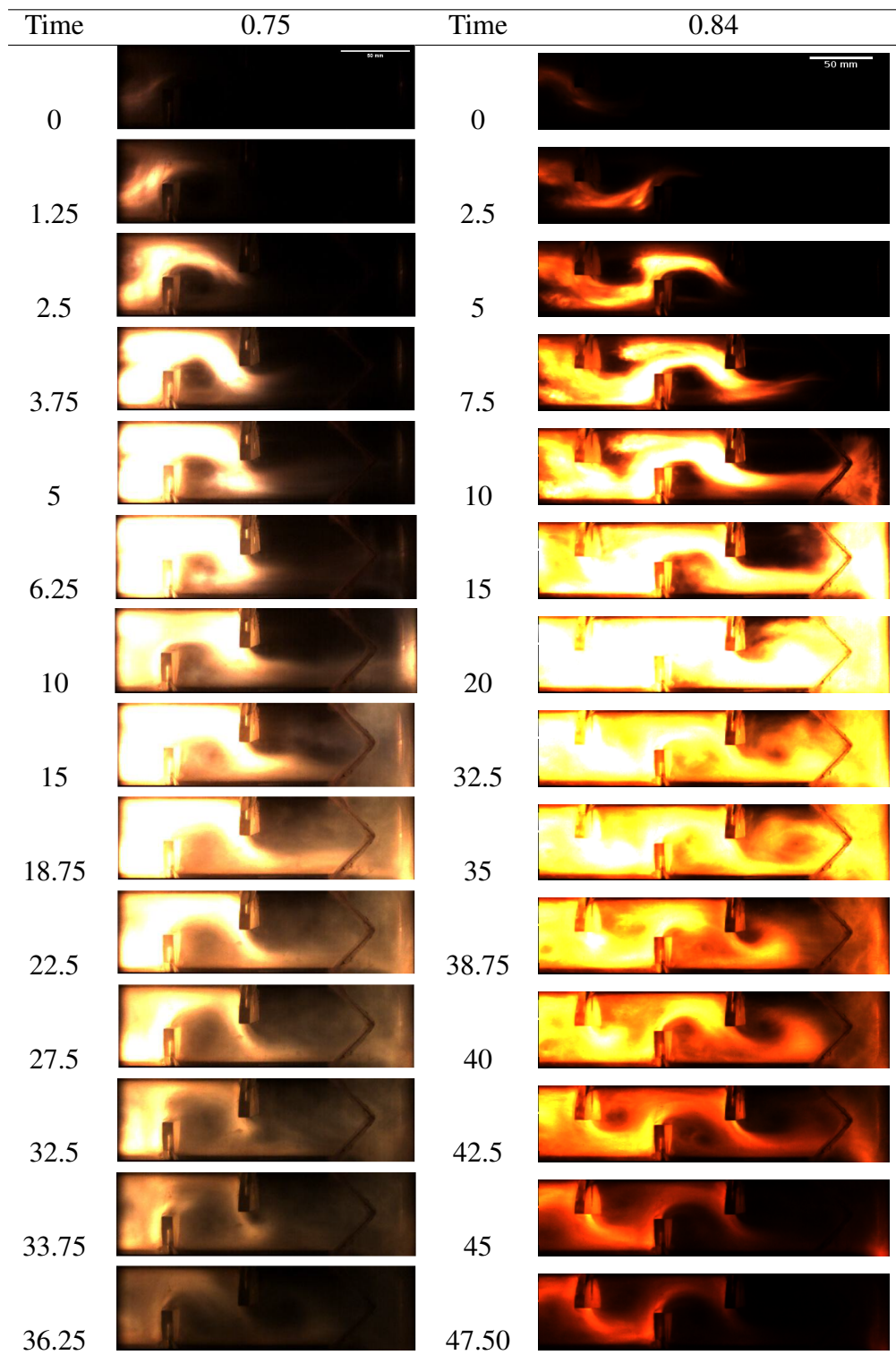
Figure 5.26: Flame propagation image of T-pipe in section I of mixtures with $\Phi = 0.75$ and 0.84

Time	0.70
11.25	
17.5	
20	
22.5	
26.25	
28.75	

Figure 5.27: Flame propagation image of T-pipe in section II and III of a mixture with Φ = 0.70

Time	0.75
6.25	
8.75	
11.25	
13.75	
16.25	
18.75	
22.5	
26.25	
30	

Figure 5.28: Flame propagation image of T-pipe in section II and III of a mixture with Φ = 0.75

Figure 5.29: Flame propagation image of T-pipe in section II and III of a mixture with Φ = 0.84

The flame does not fill the region between the obstacles during the propagation of the flame front. The vorticity formation between the obstacles is observed for all three methane-air concentrations. A flame propagation can be observed in the experiment Φ = 0.84 during the time 38.75 s until 47.50 s.

The flame propagates to both sides in section II and III. But the flame tends to propagate with a higher intensity to section II due to the position of the last obstacles in section I. The flame loses intensity and brightness in section II and III due to the fast propagation in these section which break the outlet PET foils.

The stoichiometric mixture experiment has a flame propagation as in Figure 5.30 for section I. Only Φ = 0.98 for section II and III are exposed in Figure 5.31. The images in section II and III of Φ = 1.0 do not have a good resolution. Both results gained an image processing improvement with the *brightness*'s tool by ImageJ.
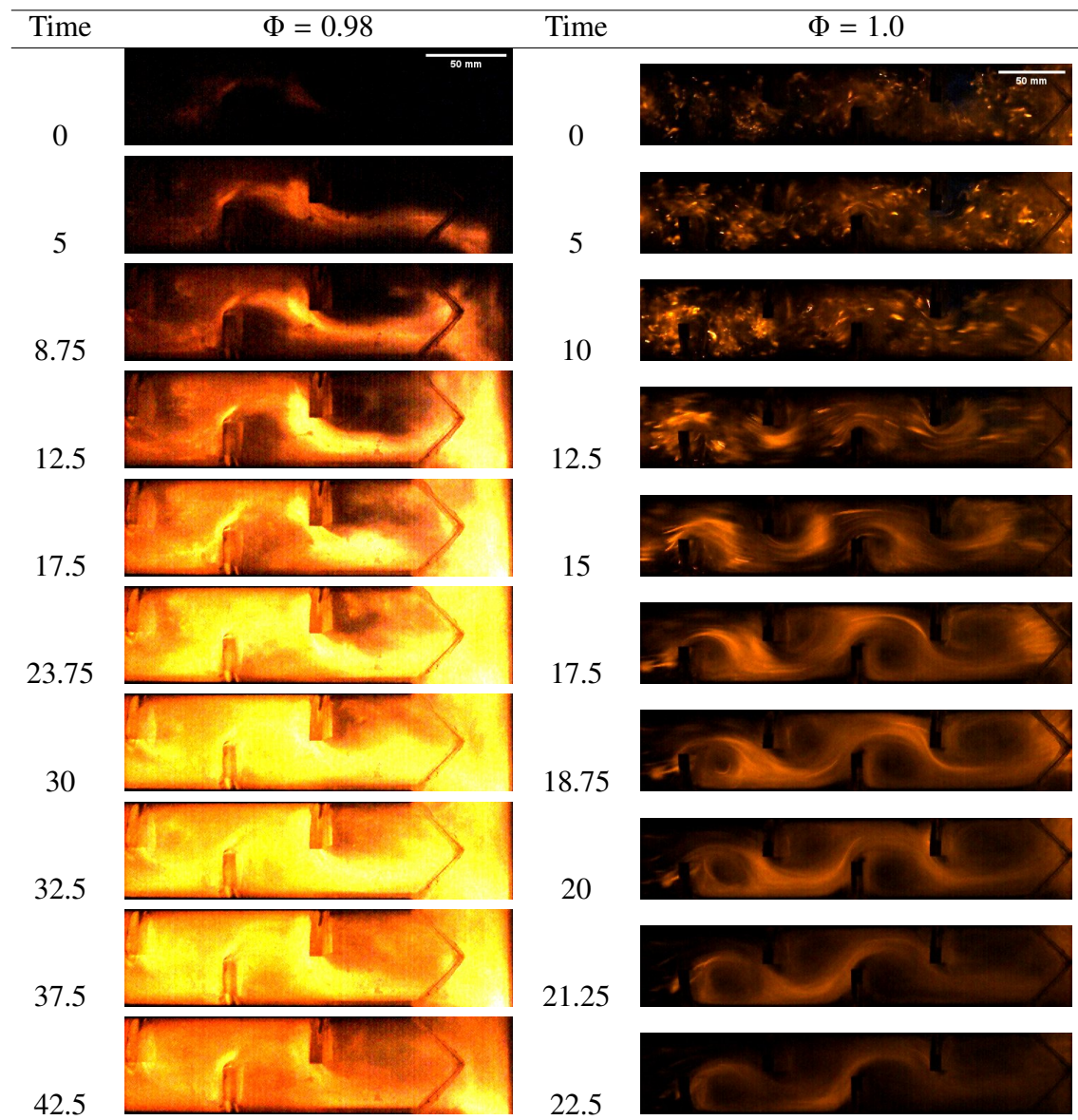
Figure 5.30: Flame propagation image of T-pipe in section I
of mixtures with Φ = 0.98 and 1.0

Time	$\Phi = 0.98$
13.75	
17.5	
23.75	
28.75	
30	
32.5	
36.25	
40	
42.5	
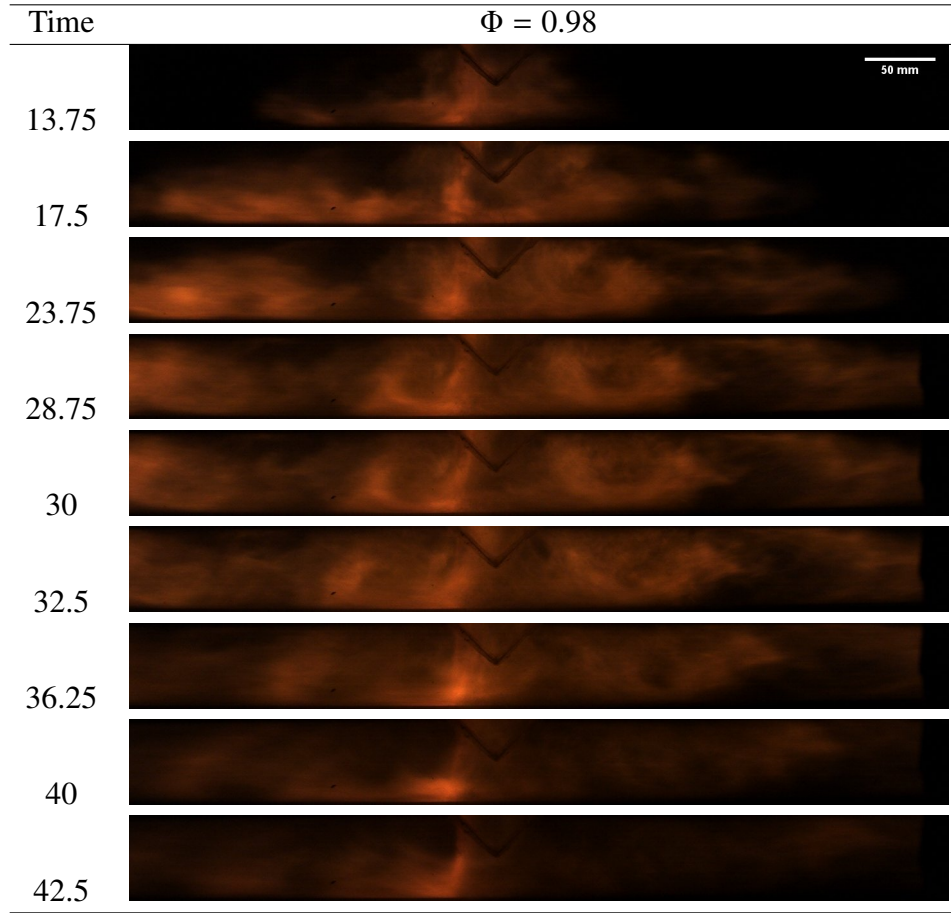
Figure 5.31: Flame propagation image of T-pipe in section II and III of a mixture with $\Phi = 0.98$

The vorticity formation and the reverse propagation can be observed in section I. The flame propagation is similar to observed for lean methane-air concentrations. The flame propagation for these methane-air concentrations does not have a high brightness intensity due to the flame speed in section II and III.

Figure 5.32 shows the flame propagation in section I of a rich mixture. And images in section II and III are exposed in Figure 5.33 and Figure 5.34. Both results have an image processing improvement with the *brightness*'s tool by ImageJ.

Time	Φ = 1.1	Time	Φ = 1.22
0		0	
1.25		5	
2.5		7. 5	
3.75		11.25	
5		15	
6.25		18.75	
7.5		20	
8.75		21.25	
10		22.5	
11.25		23.75	
12.5		25	
13.75		26.25	
15		27.5	
16.25		28.75	
17.5		30	
18.75		31.25	
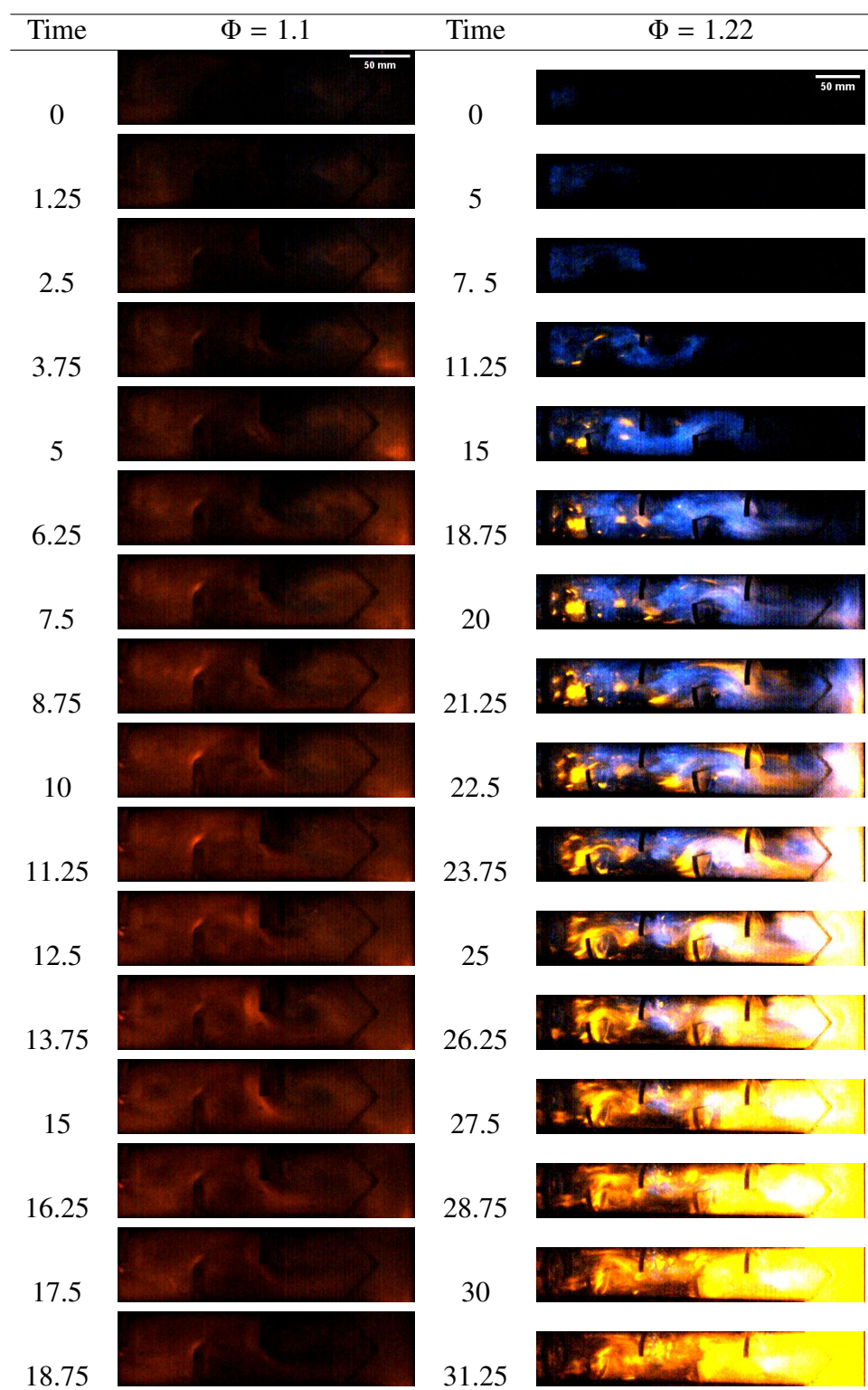
Figure 5.32: Flame propagation image of T-pipe in section I of mixtures with Φ = 1.1 and 1.22
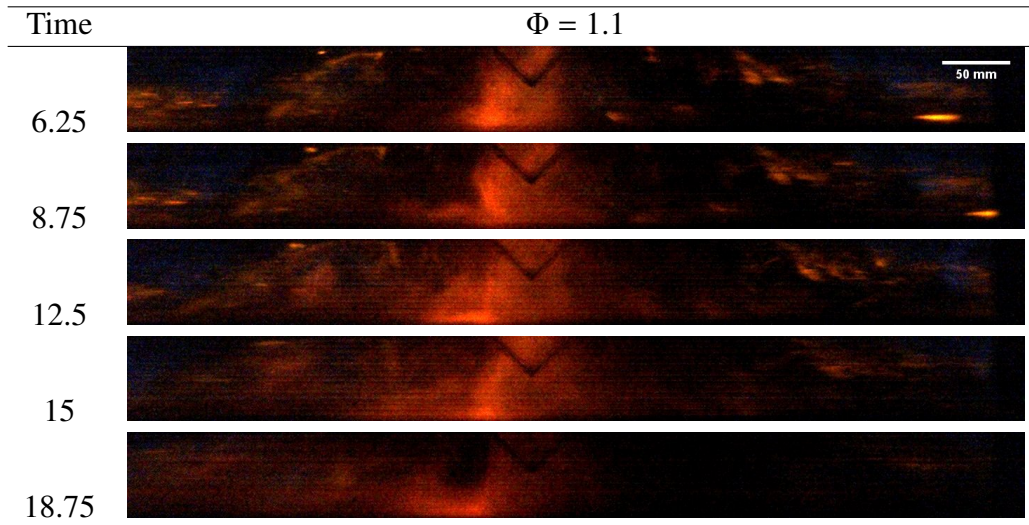
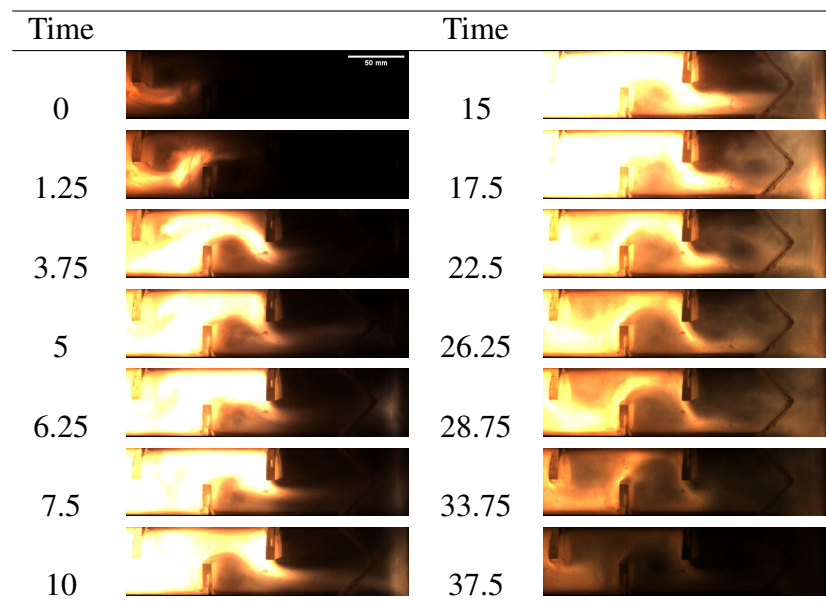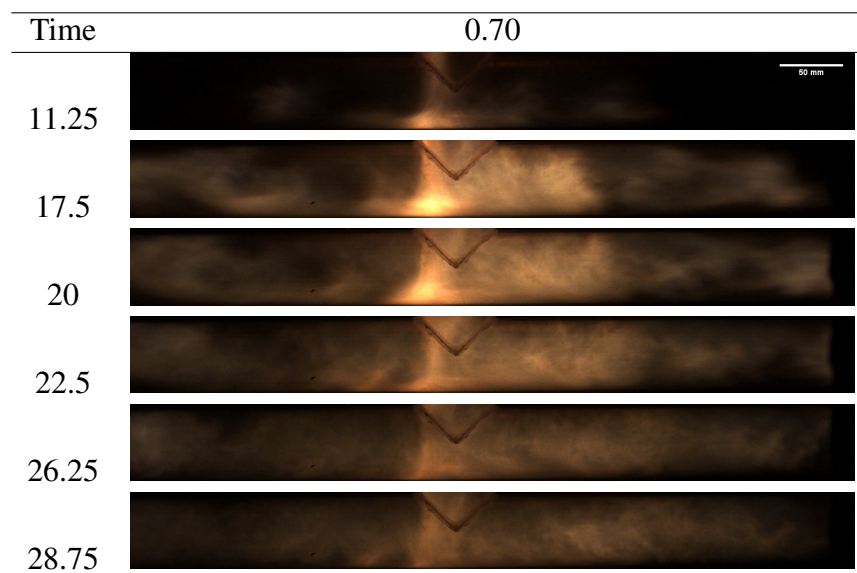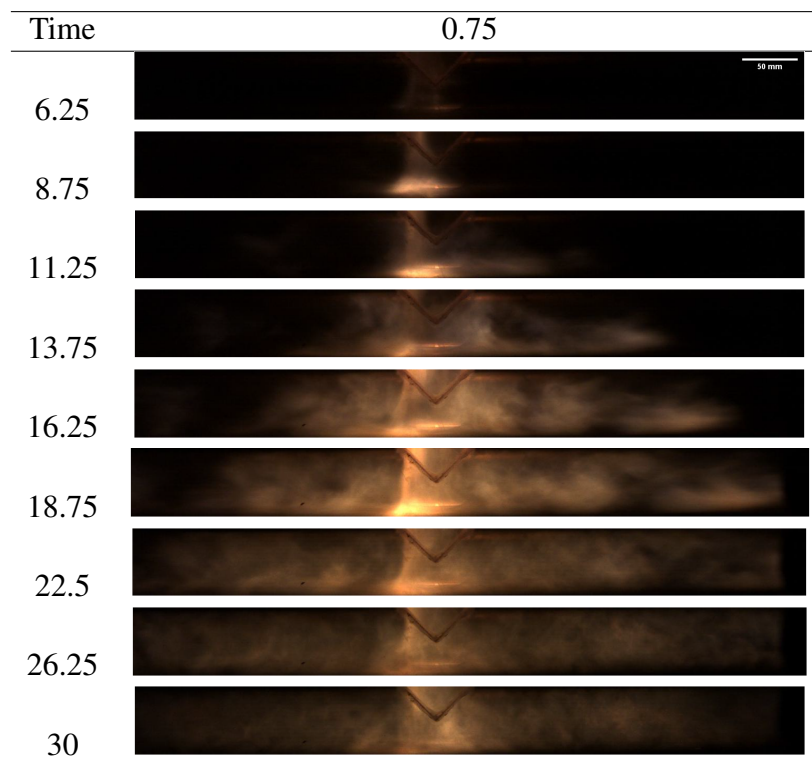Figure 5.33: Flame propagation image of T-pipe in section II and III of a mixture with Φ = 1.1
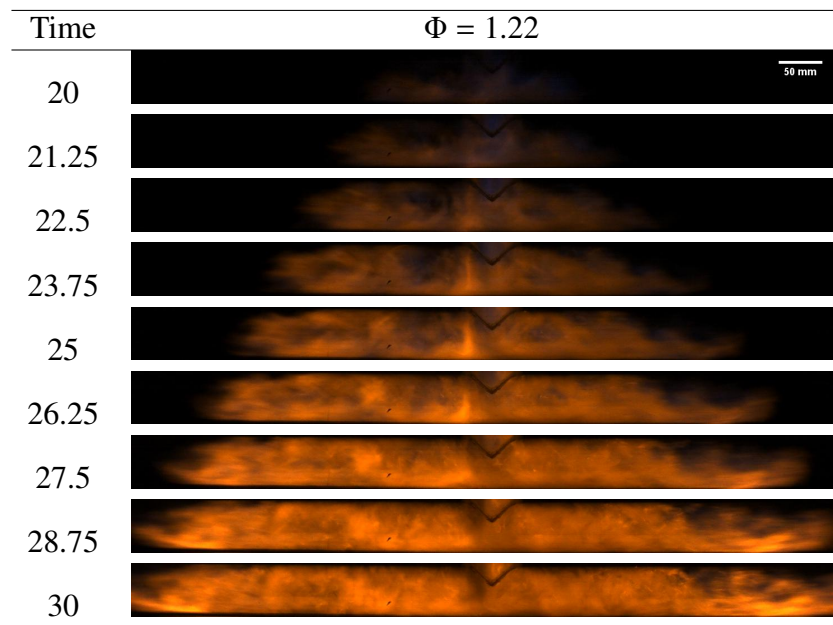
Figure 5.34: Flame propagation image of T-pipe in section II and III of a mixture with Φ = 1.22
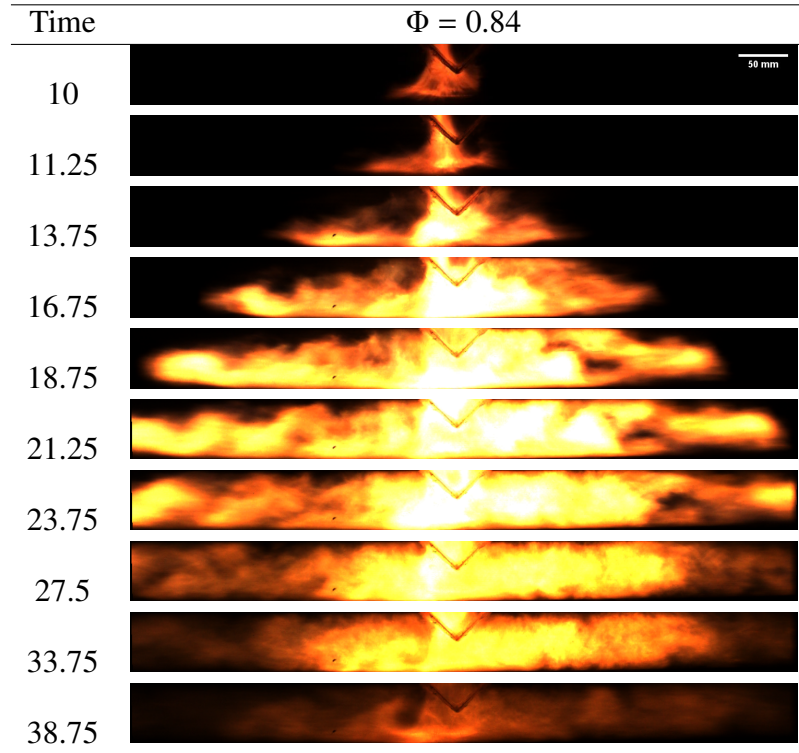
The flame propagation and nuance of the flame brightness can be observed in the results with Φ = 1.1 and 1.22 in section I. This nuance shows a variation of the methane-air reaction during the flame propagation.

The main differences of the flame propagation during the variation of methane-air concentration are the brightness intensity visualization, the speed of the flame, and the pressure. The flame front partially touches the wall and the obstacles in section I. The flame has a turbulent propagation with a vorticity formation in the space between the obstacles. The vorticity formation remains between the obstacles when the flame front already reaches the bent section. The flame continues a reaction in the zone behind the flame front, especially in the area between obstacles and after the flame crosses the obstacles.

The turbulent flame propagation hits the upper and lower part of the wall in section II and III. This vorticity formation and the flame speed increases. A reverse propagation happens from section II and III into section I. The flame propagates with a higher intensity into section II, see Figure 5.35 due to the last obstacle on the right part in section I.
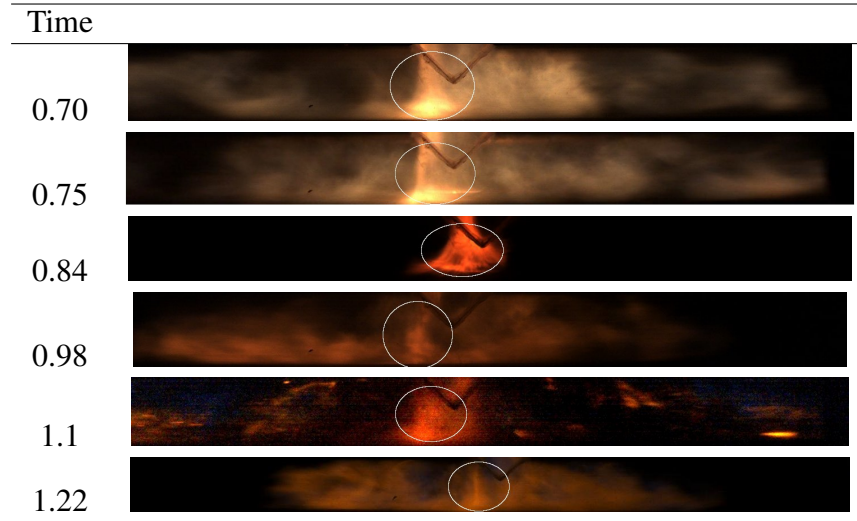
Figure 5.35: Flame propagation images in section II and III by equivalence ratio

Chapman and Wheeler [71] found that obstacles can accelerate the flame propagation in a tube. Lee [72] and Wang [62] also observed an increase of flame speed for a methane flame propagation in tubes with obstacles. The flame speed is estimated between the last obstacle and the bent region of the pipe for section I. For section II and III it is estimated in the region after the bent part in section I.

The T-pipe with obstacles shows a high flame speed propagation, see Figure 5.36 for section I, II, and III. To estimate the flame speed is challenging considering the obstacles which provoke a vorticity formation and the small number of frames. This small number is caused by the high velocity of the flame even though 8000 fps are used to record the propagation.
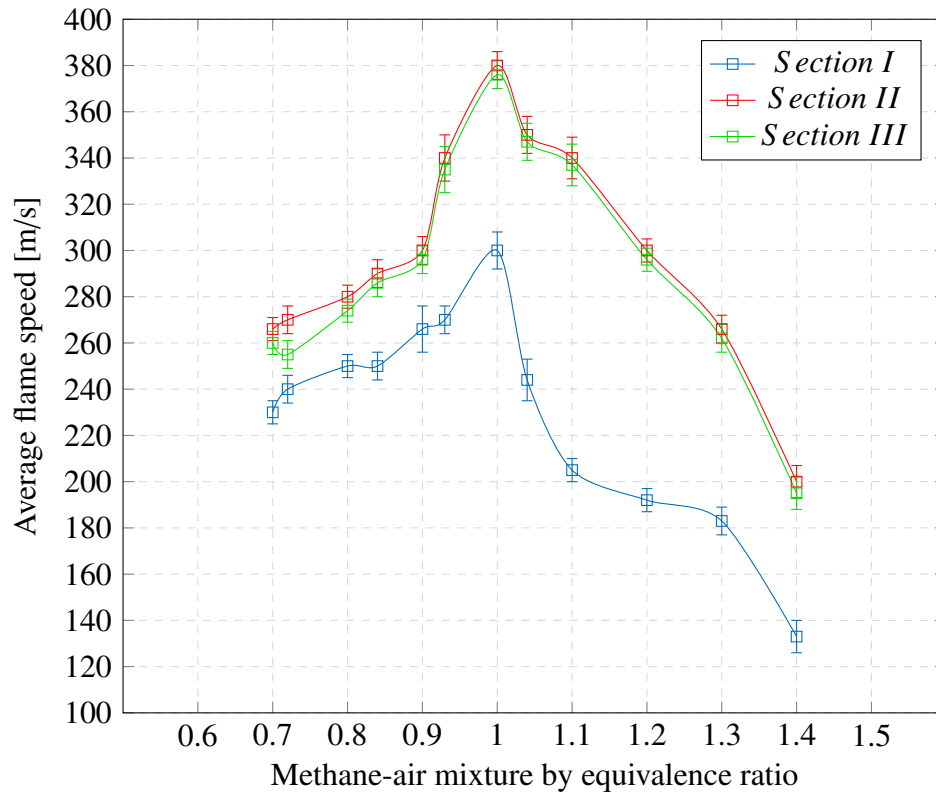
Figure 5.36: Premixed flame speed of T-pipe with obstacles by methane-air concentration

The flame front speed and the increase of flame speed provoked by the bent region of the T-pipe with obstacles are higher than the T-pipe without obstacles. The flame speed in section II is higher than section III due to the position of the last obstacles in section I. The stoichiometric methane-air concentration is the region where the highest flame speed is recorded. It shows an increase of 21% when the flame crosses the bent region. The moment in which the outlet PET foils break is not detected by images due to high flame speed. Wang [62] estimated flame speed for a straight pipe and an outlet PET foil has the same magnitude of the flame speed shown in Figure 5.36 for section I.

6. Numerical Investigation of Premixed Flame

Numerical simulations are performed for lean, stoichiometric, and rich methane-air concentrations. The OpenFoam combustion model *XiFoam* is used in the CFD simulations of premixed flame propagation in small scale geometry. The CFD investigation reproduces numerically the flame propagation in a T-pipe with and without obstacles.

Before setting up the final simulation it is essential to perform a series of simulation tests. In terms of saving time, the first test is realized in a 2D geometry. In total, mesh refinement, turbulence models, discretization methods, mathematical models, boundary, and initial conditions are tested. However, in this work, only the 3D simulations are discussed. The pre-tests are carried out to improve the accuracy of the CFD simulation results and to save time in the simulation with refined meshes. The steps to develop a CFD simulation are geometry, mesh, fluid dynamics assumptions and models, boundary and initial conditions, discretization models, mathematical solution methods, and time control.

6.1 Simulation Assumptions

The description of the assumptions is critical to establish the phenomenon in numerical simulations. The reaction of methane-air is set up as one single reaction and irreversible.

The one-step reaction and the fast chemical reaction are represented as generating solely products without any further reaction, as discussed in Section 2.1. The reaction is implemented in the code as fuel and oxidizer. The reaction stops when one of them depletes. Both assumptions are implemented through the PDF model, see Section 3.6. The domain is defined as compressible due to the high temperature and pressure gradient. On the grounds of this scenario, the governing equations must be solved using the Favre average method, as explained in Section 4.2. Additionally, it is assumed that the turbulence model is homogeneous, isotropic, and uses Boussinesq approximation, in detail discussed in Section 4.7. The

transport properties are represented with Sutherland equations, see Section 2.4. The thermo-dynamic properties are estimated based on Janaf equations. The thermodynamic condition is assumed to be a perfect gas mixture with an absolute enthalpy, discussed in Section 2.2.

6.2 Numerical Simulation Setup

6.2.1 Geometry and Mesh

The geometry is generated with the software ANSYS and exported to the software ICEM to establish the mesh. The geometry is designed like the apparatus used in the experiments. The mesh should be refined based on the flame thickness and the simulation convergence. The analytic tools diffusive and blint flame thickness are used to estimate the flame thickness to become a reference for the mesh refining, see Section 3.1. The geometries used in the simulations are represented in Paraview, see Figure 6.1 and Figure 6.2.

It is important to know the mesh constraint to generate an accurate mesh for the simulation and also to know the mesh quality to obtain accurate results. The mesh quality is checked for each mesh used by the tool *checkMesh* which evaluates the errors as skewness, aspect ratio, minimum face area, and non-orthogonality. All meshes used in the simulations are available by the OpenFOAM mesh evaluation.
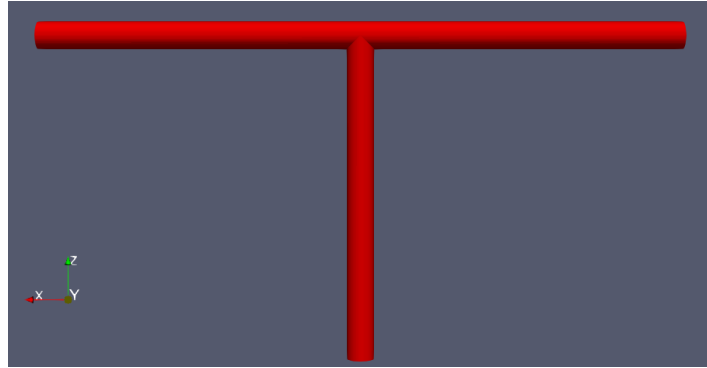
Figure 6.1: T-pipe geometry without obstacles
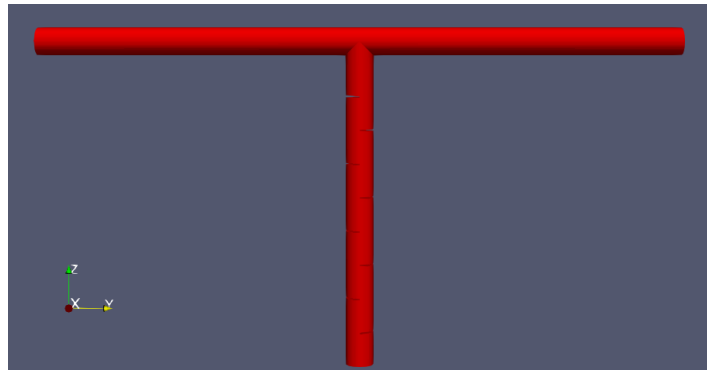
Figure 6.2: T-pipe geometry with obstacles

The mesh should be refined enough to solve turbulence energy from Kolmogorov η_k until integral length scale l_t, see Section 3.3. But the Kolmogorov length scale is too small and it is applicable for DNS simulations. Hence the cell size $\triangle x$ is set using the flame thickness as reference by the domain size L and the number of divisions N, see Equation 6.1.

$$\triangle x = \frac{L}{N} \tag{6.1}$$

The number of divisions is used in ICEM to set the refinement of the mesh. So the simulations are tested to observe the best solution of the governing equations. Several mesh tests are performed in 2D geometry using RANS turbulence models, and in 3D geometry using Large Eddy Simulation (LES) turbulence models. The 3D meshes are refined based on the number of divisions using the o-grid method, see Table 6.1 for the total number of cells.

Table 6.1: Mesh definition by number of cells

Geometry	Test
T-pipe	443552
T-pipe obstacles	491104

The meshes with a higher refinement than the applied in Table 6.1 did not show an improvement in the simulation performance and results. Because when the meshes are too refined, the simulations do not converge even if the tolerance in computing is increased. The CFD simulation has an unrealistic representation due to the size of the ignition point which is represented by a large number of ignition parameters in the calculation of the governing equations. And the flame front thickness is bigger than the mesh cell. Tests are carried out to decrease the diameter of the ignition site further than displayed in Table 6.6. But the simulation tested also remains out of a realistic observation.

The mesh type is also important to be defined. A hexahedral mesh is used following the concept of the geometries and the applicability of the LES turbulence model with *cubeRootVol*. The o-grid method is used to set the center of the geometry because it is a cylinder geometry, see Figure 6.3 [73, 74]. The sidewalls of the pipes are built using the hexahedral grid. The mesh refinement of the geometry side is similar for both meshes, see Figure 6.4. The bent region of the T-pipes has the meshes, as illustrated in Figure 6.5.
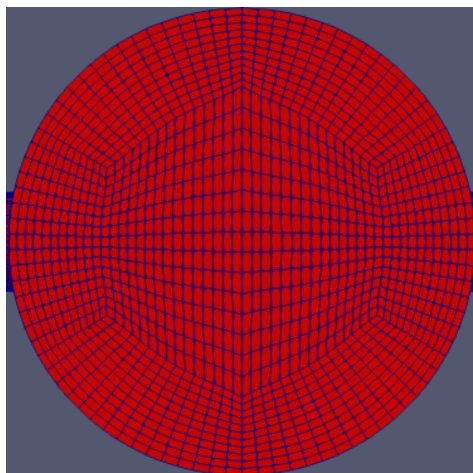
Figure 6.3: Wall mesh with o-grid method
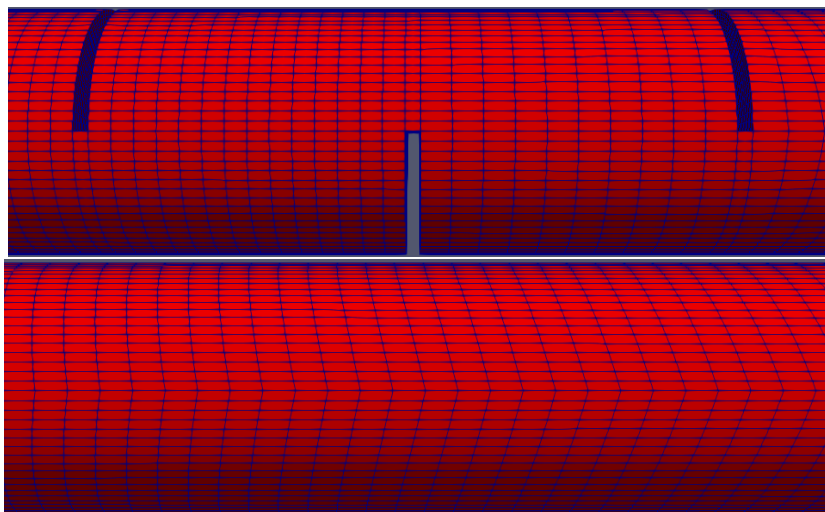
Figure 6.4: Side wall for T-pipes with obstacles and without obstacles
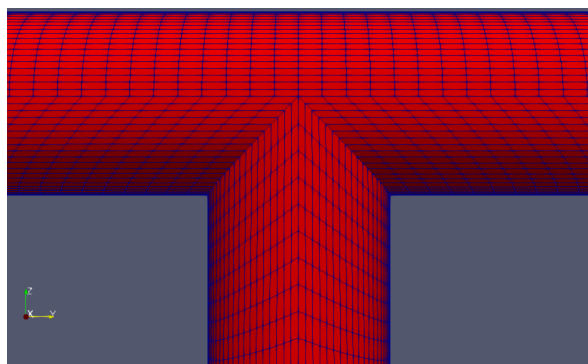
Figure 6.5: Bent region of T-pipes

6.2.2   Initial and Boundary Conditions

The parameters for premixed flames simulations for LES turbulence models are presented in
Table 6.2. *ft* parameter is only used in the inhomogeneous simulation because it is crucial to
define an inhomogeneous mixture, see Section 4.6.

Table 6.2: Parameters for the CFD simulation

Parameters	Symbol	Initial Conditions	Unit
Turbulence thermal diffusivity	alphat	0	$Kg.m^{-1}.s^{-1}$
Regress variable	b	1	1
Fuel mixture fraction	ft	-	1
Turbulence kinetic energy	k	-	$m^2.s^{-2}$
Pressure	p	101325	$Kg.m^{-1}.s^{-2}$
Laminar flame speed	S_L	-	$m.s^{-1}$
Initial temperature	T_0	300	K
Unburnt gas temperature	T_u	300	K
Velocity	U	(0 0 0)	$m.\ s^{-1}$
Flame wrinkle factor St/Su	Xi	-	1

Simulations are performed with an equivalence ratio variation step of 0.1 in the range of
$0.5 \leq \Phi \leq 1.5$. The fuel mixture fraction and laminar flame speed parameters are added
based on the current methane-air equivalence ratio simulation. The unburnt flame speed
is approximated to laminar flame speed with Gulder's correlations, see Equation 3.2. The
turbulence kinetic energy is estimated with analyses from the previous simulations.

The PET foils in the geometries can support the pressure of 5 bar, see Section 5.2. Although,
the PET foils break during the flame propagation even if the maximum pressure explosion is
lower than 5 bars. To set these boundary conditions in OpenFOAM is a challenge albeit the
software offers a large packet of boundary conditions.

In this way, two scenarios with different boundary conditions are simulated. These boundary
conditions tests are restricted only for the outlet part with PET foils. In the first scenario,
the outlet part is set up like a wall using the boundary conditions *wall*. It represents the fluid
flows until the PET foils and returns, notwithstanding the simulation is evaluated until the
fluid reaches the wall. In the second scenario, the outlet part is set up like a piston using
the boundary conditions *patch*. It represents a general boundary condition where the type is
set up in the initial condition files. *movingWall* is used to represent a piston wall that has a
pressure release and outlet flow when the fluid reaches the PET foils. The type *movingWall*

belongs to a packet of boundary conditions options. At the beginning of the simulation similar to the experiments, an archive pressure balance inside of the pipe is set up in the boundary conditions *patch* and *wall*. The boundary conditions are added in the file *boundary*. The type of boundary conditions is set up inside of the initial conditions files, see Table 6.3.

Table 6.3: Boundary conditions for wall and movingWall simulations

Parameters	BC Wall	BC Patch
alphat	alphatWallFunction	zeroGradient
b	zeroGradient	zeroGradient
ft	zeroGradient	zeroGradient
k	kLowReWallFunction	zeroGradient
p	zeroGradient	zeroGradient
S_u	zeroGradient	zeroGradient
T_0	zeroGradient	zeroGradient
T_u	zeroGradient	zeroGradient
U	fixedValue	fixedValue
Xi	zeroGradient	zeroGradient

zeroGradient is a homogeneous Neumann boundary condition because the quantity gradient is zero in the perpendicular direction of the boundary. *fixedValue* is a Dirichlet boundary condition [34, 46].

Velocity *U* is represented as the type *fixedValue* for all *wall* regions in the geometry. *U* is only represented as the type *movingWall* in the outlet region for the simulations which are desired to represent the PET foils as a piston. Wall functions used in the parameters *alphat* and *k* are only used in the regions of the *wall* type. These functions are set as *zeroGradient* in the region of the *movingWall* type. The usability of these parameters in the solution of the governing equations depends on the applied turbulence method. *alphatWallFunction* is a wall function for turbulence thermal diffusivity strictly applied for compressible scenarios. *kLowReWallFunction* is a pure *zeroGradient* Neumann boundary condition for high and low Reynolds numbers. The model operates in two modes, based on the computed laminar-to-turbulent switch-over *y+* value derived from *Kappa* and *E*. The property values for these wall functions are presented in Table 6.4 [4, 7].

Table 6.4: Wall functions parameter values

Parameters	Values
Cmu	0.09
Kappa	0.41
E	9.8
Prandtl	0.85

6.2.3 Combustion Properties

Combustion properties are set based on the models offered for the *XiFoam* code, see Section 4.6. It is important to understand the phenomenon, the scenario, and the mixture type to set the correct combustion sub-models. The model *transport* to calculate laminar flame speed and the flame wrinkle factor by the governing equation requires more simulation time but shows better results, see Table 6.5.

Table 6.5: Combustion settings

Function	Option
Laminar flame speed correlation	Gulders
Strain laminar flame speed model (SuModel)	transport
Equivalence ratio	-
Flame wrinkle factor model (XiModel)	transport

According to Williams [16], the spark system is usually made from discharged condensers based on capacitance energy. The duration of these discharges can be as short as $0.01 \times 10\ s$ or as long as $100 \times 10\ s$ for a larger engine. The ignition point in the geometry, the ignition sphere diameter, the ignition start time, the duration of the spark, and how strong is the spark is all set up. In the experiment, a spark generator is used as described in Section 5.1.2. In the CFD simulation, the discharge is set up as presented in Table 6.6.

Table 6.6: Ignition settings

Ignition Site	Values	Unit
Location	(0 0 0.015)	m
Diameter	0.003	m
Start	0.003	s
Duration	0.03	s
Strength	300	J

6.2.4   Thermophysical Properties

Thermodynamic and transport properties are set up in *thermophysicalProperties*, see Table 6.7. Premixed flames are set as homogeneous and inhomogeneous mixtures, see Section 2.1. The other proprieties are set with the same model.

Table 6.7: Thermophysical properties by mixtures simulated

Property	Inhomogeneous Premixed	Premixed
Type	heheuPsiThermo	heheuPsiThermo
Mixture	inhomogeneousMixture	homogeneousMixture
Transport	sutherland	sutherland
Thermodynamic	janaf	janaf
Equation of State	perfectGas	perfectGas
Energy	absoluteEnthalpy	absoluteEnthalpy

heheuPsiThermo is the thermophysical model to solve the energy equation for combustion simulations, see Section 4.1.3. The model is formulated for unburnt compressible gas using the PDF model which defines the reaction zone. A perfect gas state is assumed because of the gas compositions and conditions. Pressure and temperature are set up in the initial conditions as experimental conditions. Density ρ is calculated in Equation 6.2.

$$\rho = \frac{p}{RT} \tag{6.2}$$

The energy variable is important to specify the energy being used for the solution of the energy equation. Energy can be set for enthalpy or internal energy. *absoluteEnthalpy* is the heat formation by enthalpy energy without the sensible energy h_s, see Equation 6.3 where c_i is the molar fraction, h_f^i is the heat formation and i is the chemical species.

$$h = \sum_i c_i \triangle h_f^i \tag{6.3}$$

6.2.5   Turbulence Properties

Turbulence models are tested only with the stoichiometric equivalent ratio $\Phi = 1$ to see the impact of the models in the flame propagation. Tests with RANS turbulence models using kEqn and LaunderSharmaKE models do not have a flame propagation which crosses the bent region. The simulation with the LES turbulence model using kEqn model with Prandtl delta settings does not have a flame propagation that reaches the bent region. The turbulence setting in the final simulation for each equivalence ratio is simulated, see Table 6.8.

Table 6.8: Turbulence properties by mixtures simulated

Turbulence	Case 1
LES	kEqn
delta	cubeRootVol

6.2.6 Simulation Discretization

The time setting solution is defined by the dictionaries *controlDict* and pursues the experimental time, see Table 6.9. To have a general end time value the same end time is set for all simulations. Even though the simulations with different methane-air concentrations do not need the same end time value to reach the outlet walls. Different time steps and end times are tested to observe the impact on the simulation convergence. The simulation has a problem with the initial values for the governing equations because it deals with a scenario starting with an explosion provoked by an ignition. The PIMPLE algorithm is used as the initiation for pressure and velocity estimations.

fvSchemes and *fvSolution* have fundamental responsibilities for numerical discretization methods to solve the governing equations based on the finite volume method. Mathematical models to solve the governing equation's terms represented in the mesh are set up in *fvSolution*, see Table 6.10. Some discretization methods for a simulation with $\Phi = 1.0$ are tested, see Table 6.11.

Table 6.9: Time control setting

ControlDict	Option
Start time	0
End time	0.4
Time step	5×10^{-7}

Table 6.10: Mathematical methods settings

(p|rho)	Initial	Final
Solver	GAMG	GAMG
tolerance	1×10^{-7}	1×10^{-7}
relTol	0.001	0
smoother	GaussSeidel	GaussSeidel
nPreSweeps	0	0
nPostSweeps	2	2
cacheAgglomeration	on	on
nCellsInCoarsestLevel	1000	1000
agglomerator	faceAreaPair	faceAreaPair
mergeLevels	1	1
(U|b|Su|Xi|ft|ha|hau|k|epsilon)	Initial	Final
Solver	PBiCGStab	PBiCGStab
preconditioner	DILU	DILU
tolerance	1×10^{-6}	1×10^{-6}
relTol	0.1	0

Table 6.11: Discretization Methods Tests

Test	Transient $d\phi/dt$	Gradient $(U) \mid (p; k; \epsilon; Xi; Su)(ft; b; ha; hau)$	Diffusion (alphaEff; b; ft; heau; hea)	Laplacian	Interpolation	Result
1	Euler	GL	$GLU*^1 \mid GLL*^2 \mid LL*^3$	GLC	Linear	R1
2	backward	GL	GLU | GLL | LL	GLC	Linear	R2
3	Euler	CGL 1	GLU | GLL | LL	GLC	Orthogonal	R1
4	backward	CGL 0.5	GLU | GLL | LL	GLC	Orthogonal	R2
5	CN*⁴0.5	GL	GLU | GLL | LL	GLC	Linear	R2
6	CN 0.5	GL	GLU | GLL | LL	GLC	Linear	R2
7	CN 0.5	GLL 1	GLU | GLL | LL	GLC	Orthogonal	R2
8	CN 1.0	CGL 0.5	GLU | GLL | LL	GLC	Orthogonal	R2

*[1] GL - Gauss linear ; *[2] GL - Gauss linearUpwind; *[3] GLL - Gauss limitedLinear ; *[4] LL - limitedLinear; *[5] CN - Crank Nicholson ; *[6] GLC - Gauss linear corrected ; *[7] CGL - cellMDLimited Gauss linear;

Surface normal gradient *snGradSchemes* is defined as *corrected*. The Laplacian method is used as default and also for other Laplacian parameters. Crank Nicholson and backward methods for gradients do not show good results even if they are second-order methods. Result R1 shows a simulation where the flame propagation reaches the outlet section. Result R2 shows a simulation where the flame does not propagate from the ignition site.

7. Simulation Results Analysis

In the current chapter, the numerical simulation of the flame propagation is analyzed concerning the experimental results presented in Chapter 5. The CFD results from OpenFOAM are evaluated with the software Paraview. The CFD simulations are performed in 3D geometries. But the 3D visualization of the flame propagation does not show the fluid dynamics of the region inside of the geometries, due to a problem in solving the governing equation from the near-wall region, see Section 3.5. For better visualization of the flame propagation, a slice tool of the 3D geometry is applied. This technique concedes to observe with high quality the flame propagation inside of the geometry.

The methane-air mixture shows an explosion in each studied concentration, but the flame does not propagate or cross the bent region of the T-pipes for each simulated methane-air concentration.

Furthermore homogeneous and inhomogeneous mixtures are compared to analyze the impact of the fuel mixture fraction parameter ft in the governing equations and the difference of flame propagation in these two mixtures.

The flame propagation is examined based on parameter regressive variable b, turbulent flame speed St, flow velocity U and adiabatic flame temperature T_a to observe the explosion, the flame expansion, front and propagation. The turbulent flame speed St and flow velocity U parameters are characterized by vector definition which is estimated by the tool *glyph scale*. This allows investigating the flame propagation of the region behind the flame front. All flame propagation frames results are set up by the time scale $\times 10^{-4}$ s.

This numerical investigation has the purpose to evaluate by computational fluid dynamics the impact of a bent region on a flame propagation and the region behind the flame front.

7.1 Numerical Analysis of T-pipe without Obstacles

The CFD simulations with a T-pipe without obstacles have no flame propagation in $\Phi = 0.5$, 0.6, and 1.5 for a homogeneous and an inhomogeneous mixture. These simulations without

flame propagation only have an explosion site in the point set up in Table 6.6.
Figure 7.1 for a homogeneous and Figure 7.2 for an inhomogeneous methane-air mixture
with Φ =0.9 show comparison analyses which have the explosion site, the flame expansion,
front and propagation by the regressive variable b in section I of the T-pipe. The impact of
the boundary conditions piston and wall are also investigated.
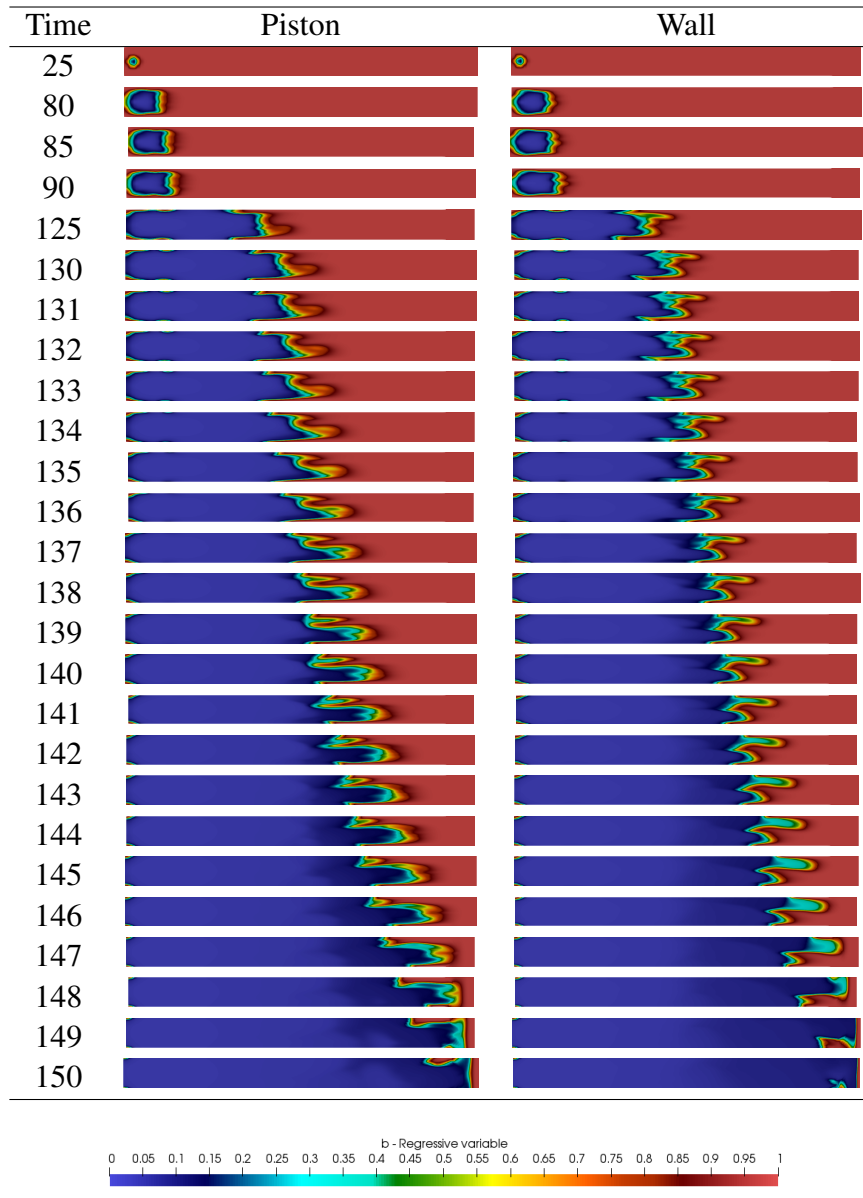

Figure 7.1: Flame propagation by regressive variable in section I of a homogeneous mixture
with $\Phi = 0.9$

Both homogeneous simulations with the boundary condition like a piston and wall indicate
a hemispherical flame front propagation in the beginning. Further propagation has a finger-
shaped elongation at frame time 130 s in both simulations. The closure of the flame front

happens near the bent region of the pipe at frame time 149 s in both simulations. The flame front has *b* value around 0.35 until 0.6 and the region behind the flame front has a value around 0 for both simulations.

Time	Piston	Time	Wall
25		25	
75		50	
100		80	
150		100	
190		115	
210		125	
220		130	
225		135	
230		136	
235		137	
236		138	
237		139	
238		140	
239		141	
240		142	
245		143	
246		144	
249		145	
250		146	
251		147	
252		148	
253		149	
254		150	

b - Regressive variable

0 0.05 0.1 0.15 0.2 0.25 0.3 0.35 0.4 0.45 0.5 0.55 0.6 0.65 0.7 0.75 0.8 0.85 0.9 0.95 1
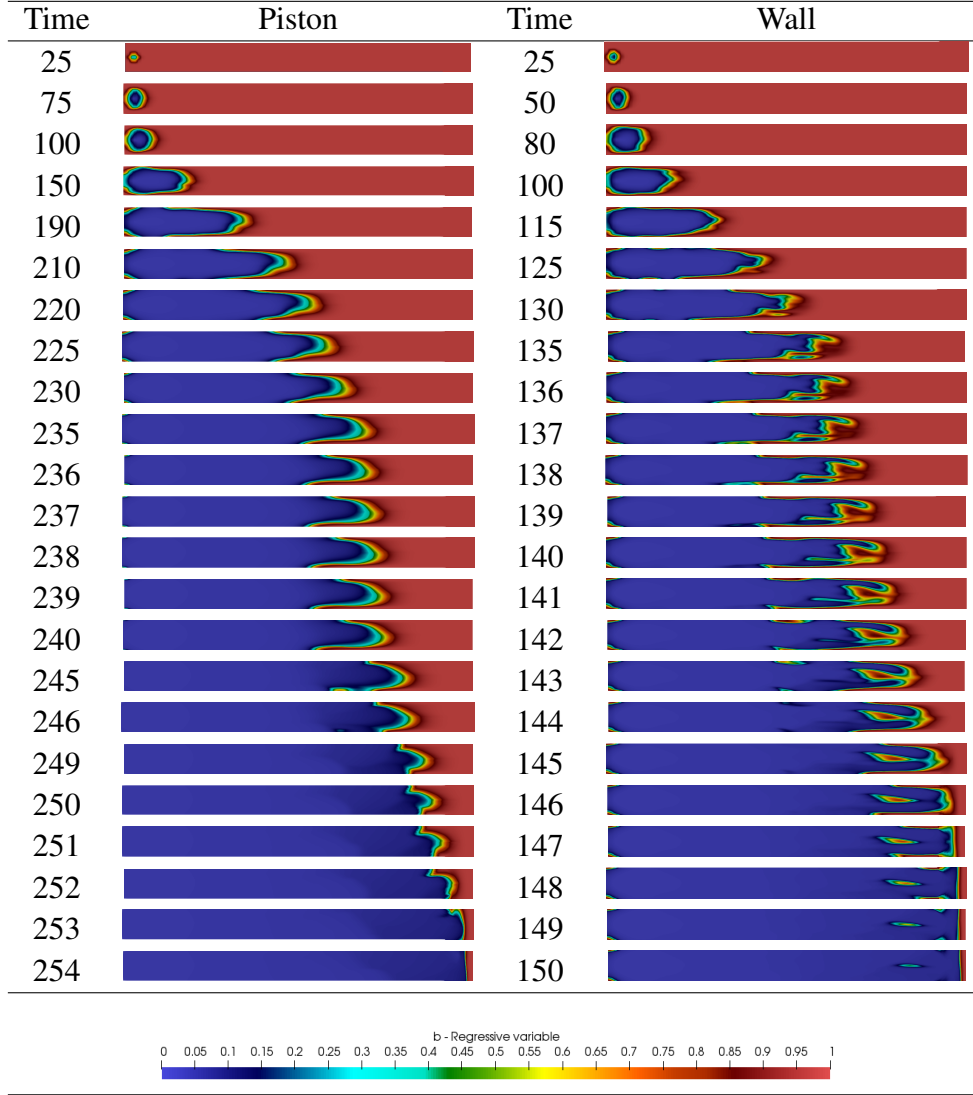
Figure 7.2: Flame propagation by regressive variable in section I variable of an inhomogeneous mixture with $\Phi = 0.9$

The regressive variable analysis of the inhomogeneous mixture simulation with the boundary condition like a piston shows a hemispherical flame front propagation until the bent region. The boundary condition like a wall shows a hemispherical flame front propagation at frame time 80 s, a finger-shaped elongation at frame time 135 s which starts to close at frame 143 s. The flame front has a full closure and reaches the bent region at frame time 150 s.

The turbulent flame speed and the turbulent flame speed vector estimation of the homogeneous mixture are shown in Figure 7.3 and Figure 7.4 for the boundary condition wall and piston, respectively.

Figure 7.3: Flame propagation by turbulent flame speed and vector flame speed in section I with BC as piston of a homogeneous mixture with $\Phi = 0.9$

Figure 7.4: Flame propagation by turbulent flame speed and vector flame speed in section I with BC as wall of a homogeneous mixture with $\Phi = 0.9$

Both homogeneous simulations indicate two increases of the flame speed and two reverse propagations. The flame propagation of homogeneous $\Phi = 0.9$ is detailed by the time frame for the boundary conditions piston and wall, respectively.

- The flame speed increases between 8 m/s and 10 m/s at frame time 130 s for both mixtures.

- The elongation starts for both mixtures at frame time 125 s.

- In both mixtures, the first reverse propagation behind the flame front happens at frame time 119 s.

- The flame speed increases again between 13 m/s and 15 m/s at frame 143 for both mixtures.

- The flame elongation close at frame time 146 s for both mixtures.

- In both mixtures, the second reverse propagation behind the flame front happens at frame time 149 s.

- The reverse propagation speed is around 15 m/s and 20 m/s for both mixtures.

The simulation with the boundary condition as a wall has the same behavior as with piston although the forward and reverse turbulent flame speed is higher. The flame propagation displayed by the turbulent flame speed shows an increase of the flame speed by the sides near the pipe wall. The center of the flame propagation shows an increase in the speed and reverse propagation occurs behind the flame front, a similar phenomenon happens in the results of the experiment. The wall boundary conditions have a closer representation of the flame propagation approaching to the experiment results.

The turbulent flame speed and its vector estimation of the inhomogeneous mixture are presented in Figure 7.5 and Figure 7.6 for boundary condition wall and piston, respectively.
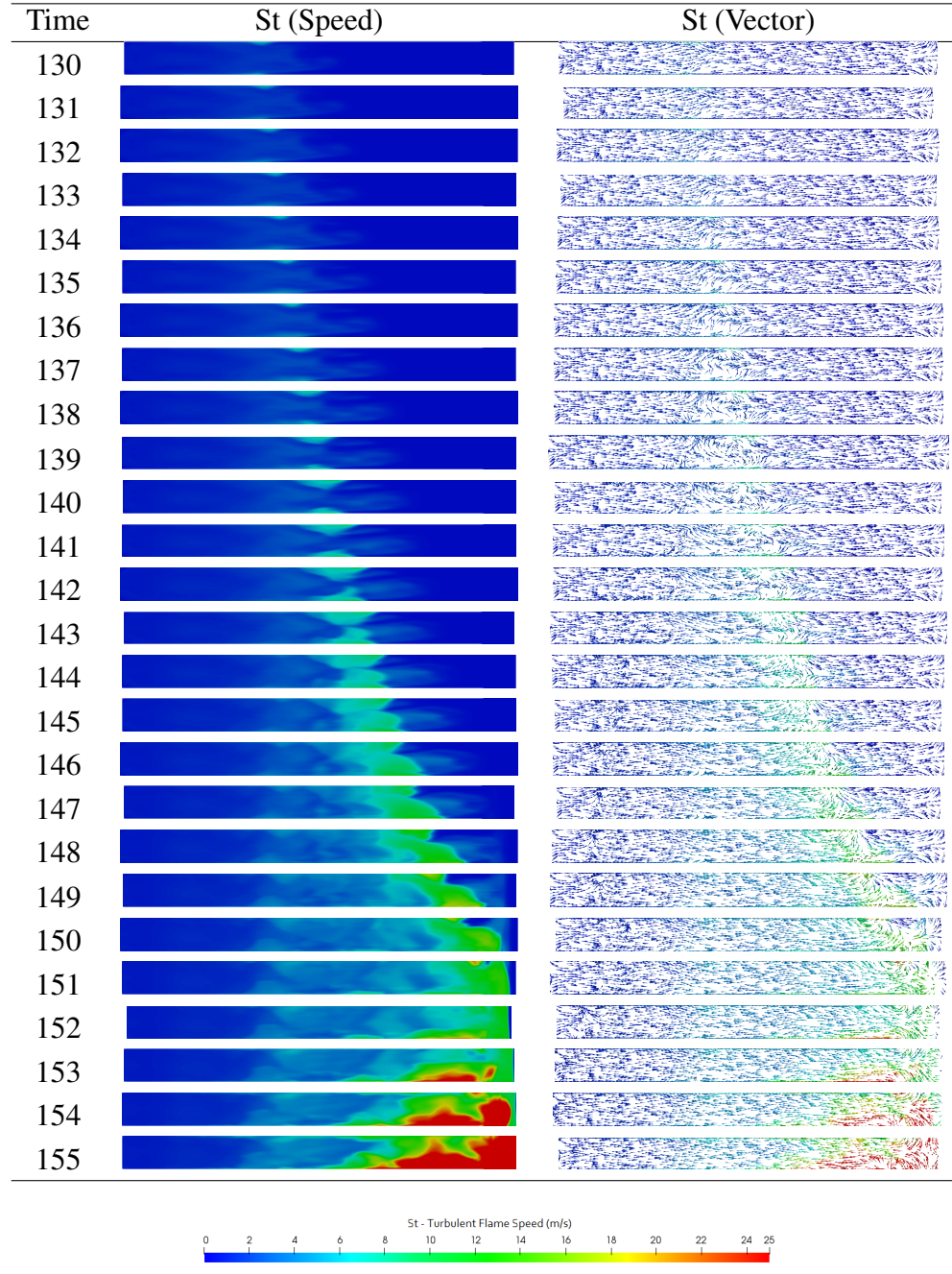
Figure 7.5: Flame propagation by turbulent flame speed and vector flame speed in section I with BC as piston of an inhomogeneous mixture with $\Phi = 0.9$
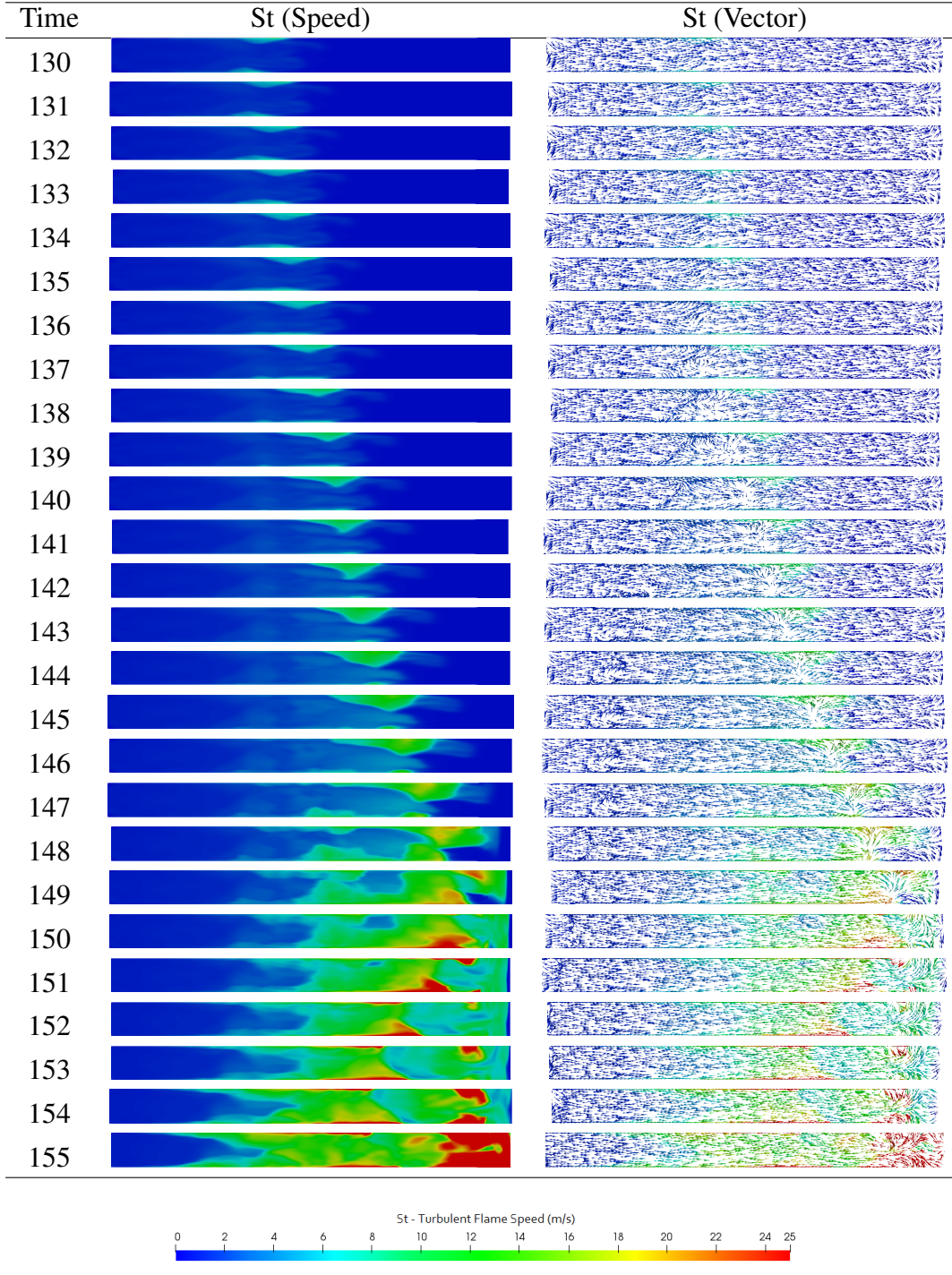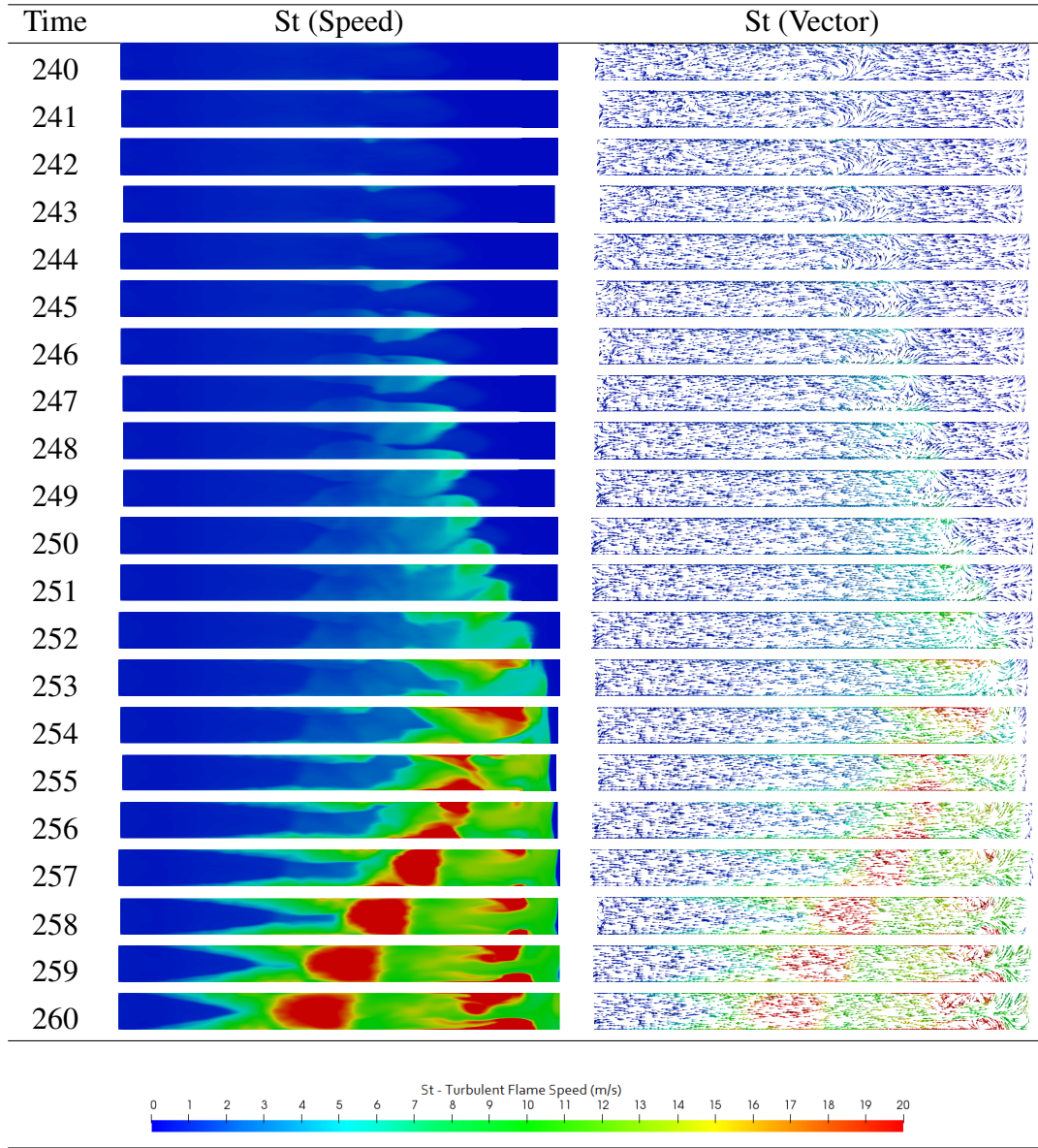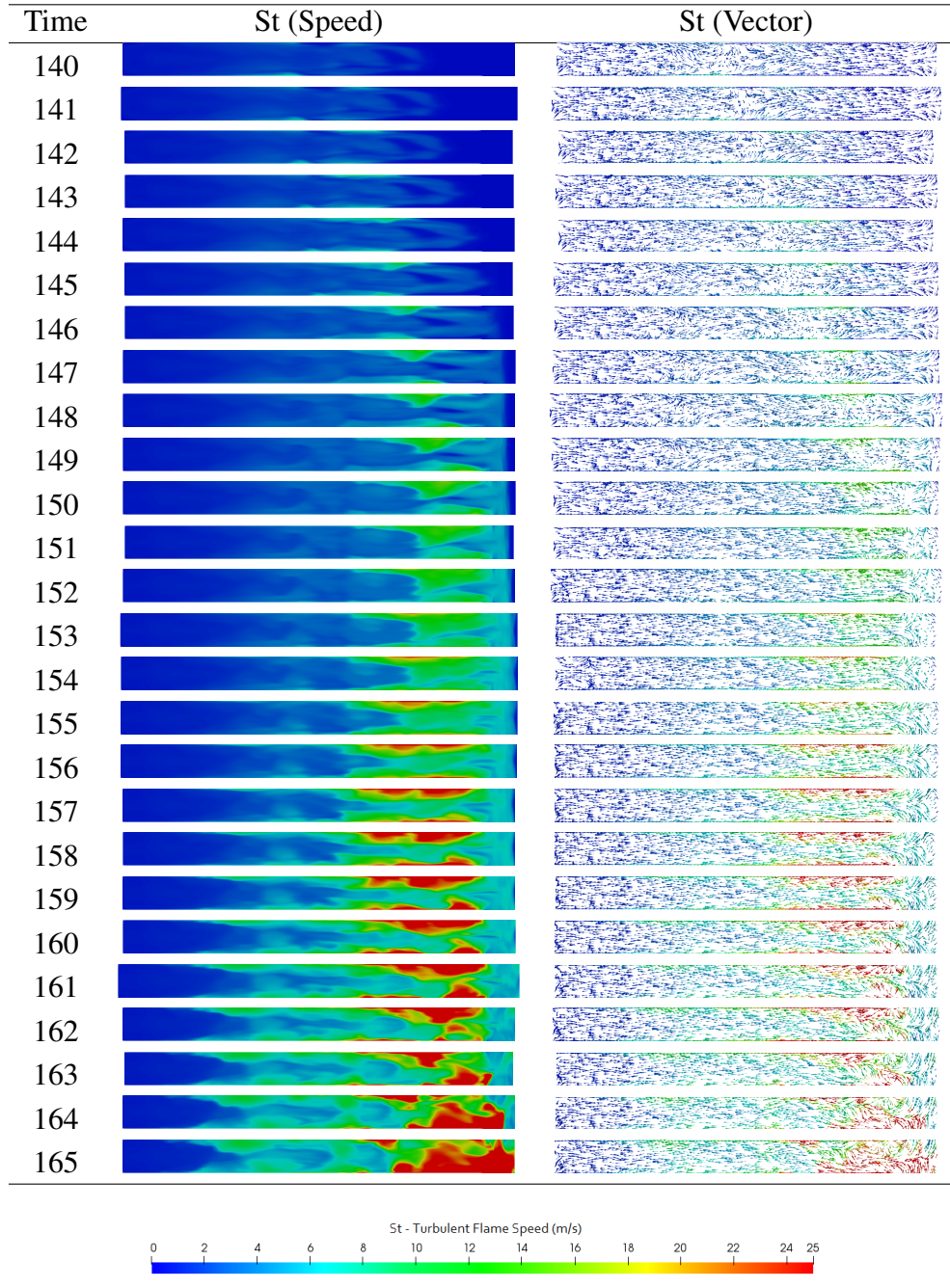
Figure 7.6: Flame propagation by turbulent flame speed and vector flame speed in section I with BC as wall of an inhomogeneous mixture with $\Phi = 0.9$

The inhomogeneous mixture with the boundary condition as a piston has a flame front propagation with a hemispherical format until the bent region. The flame propagation of inhomogeneous $\Phi = 0.9$ with piston as boundary condition is detailed by the frame time.

- The region behind the flame front shows an increase of the flame speed between 8 m/s and 9 m/s at frame time 246 s.

- The reverse propagation behind the flame front starts at frame time 249 s.

- The reverse propagation has a speed of around 12 m/s at frame time 253 s.

- A hemispherical reverse propagation can be observed at frame time 257 s until 260 s with a speed around 20 m/s. At the same frame, an elongation of a finger-shaped flame propagates forward with flame speed also around 20 m/s.

- This elongation has a closure at frame time 260 s in the bent region.

- The reverse propagation behind the flame front has a lower speed and there is an elongation speed which is around 12 m/s.

The flame propagation of inhomogeneous $\Phi = 0.9$ with a wall as the boundary condition is detailed by the frame time.

- The turbulent flame speed is very low in the hemispherical flame front propagation at frame time 115 s.

- The elongation of the flame front starts at frame time 135 s.

- A reverse propagation in the region behind the flame front is observed at frame time 141 s.

- The flame speed increases between 16 m/s and 17 m/s at frame time 144 s.

- The elongation closes at frame time 146 s and a second reverse propagation starts behind the flame front.

- The reverse propagation increases the speed between 17 m/s and 18 m/s at frame time 150 s.

- The second reverse propagates backward and reaches the first reverse propagation around at frame time 155 s.

Both boundary conditions have the flame front with a regressive variable around 0.35 until 0.6. And the region behind the flame front has a regressive variable around 0. Inhomogeneous mixture simulations with the boundary conditions wall offer the most realistic result if compared to the inhomogeneous premixed flame experimental results. Thus the further results are from the simulation of inhomogeneous premixed flame using a wall as the boundary

conditions for the outlet PET foils.

The addition of parameter *ft* which defines the mixture as inhomogeneous impacts the scenario, especially in the flame speed scale and the flame front near the bent region. Regarding the inhomogeneous simulation with the boundary conditions piston, the propagation in the region behind the frame front shows two reverse propagation and an increase of these reverse propagation speeds.

Section II and III of the simulation for a mixture with $\Phi = 0.9$ are analyzed by the regressive variable, the turbulent flame speed and the vector representation of the turbulent flame speed, see Figure 7.7.
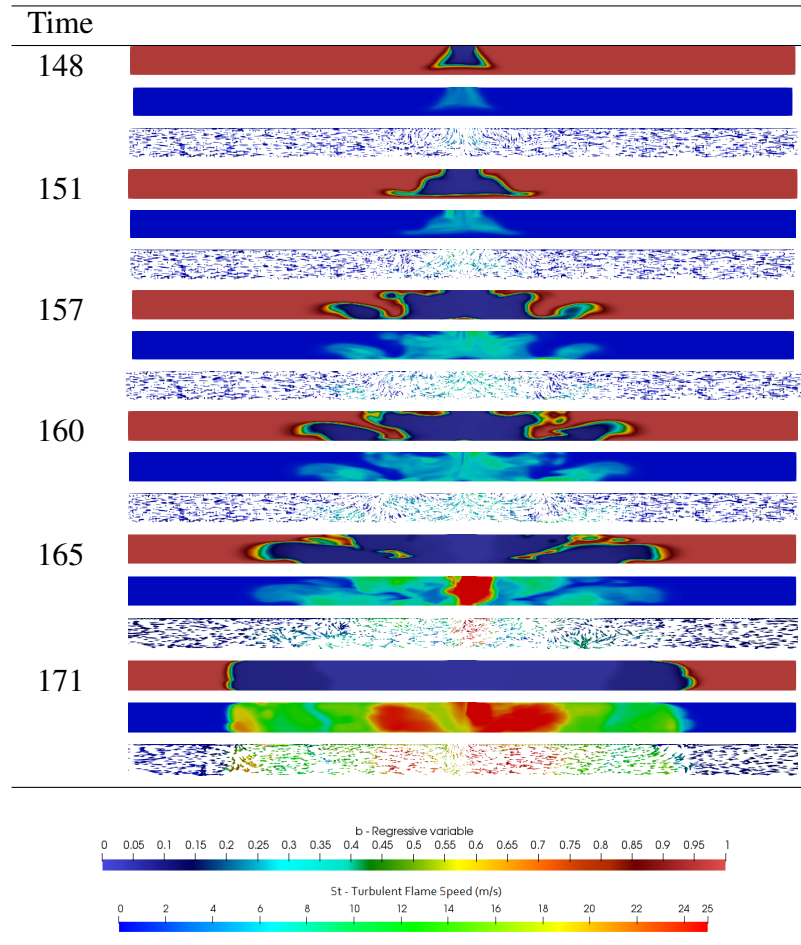
Figure 7.7: Flame propagation by regressive variable, turbulent flame speed and vector flame speed in section II and III of a mixture with $\Phi = 0.9$

The flame front in section II and III displays an equal propagation for both sides. The flame front tends to propagate near the bottom part of the wall as observed in the experiments. There is a vorticity formation in both directions and reverse propagation into section I. The flame front continues with a regressive variable around 0.35 until 0.6. And the region behind

the flame front has a regressive variable around 0. The flame propagation of inhomogeneous $\Phi = 0.9$ with a wall as the boundary condition is detailed by frame time.

- The flame speed increases from 16 m/s into 18 m/s at frame time 157 s in section II and III.

- A reverse propagation occurs in section I with a speed of around 24 m/s at frame time 165 s.

- The simulation stops when the unburnt fluid in the domain reaches the outlet wall and the flame does not propagate further. The flame stops at frame time 171 s and with a pressure 0.38 bar, see Figure 7.29.

Further numerical simulation results are presented by the equivalence ratio and divided by lean, stoichiometric, and rich concentrations. The lean inhomogeneous mixtures by regressive variables in section I are shown in Figure 7.13 and Figure 7.9.
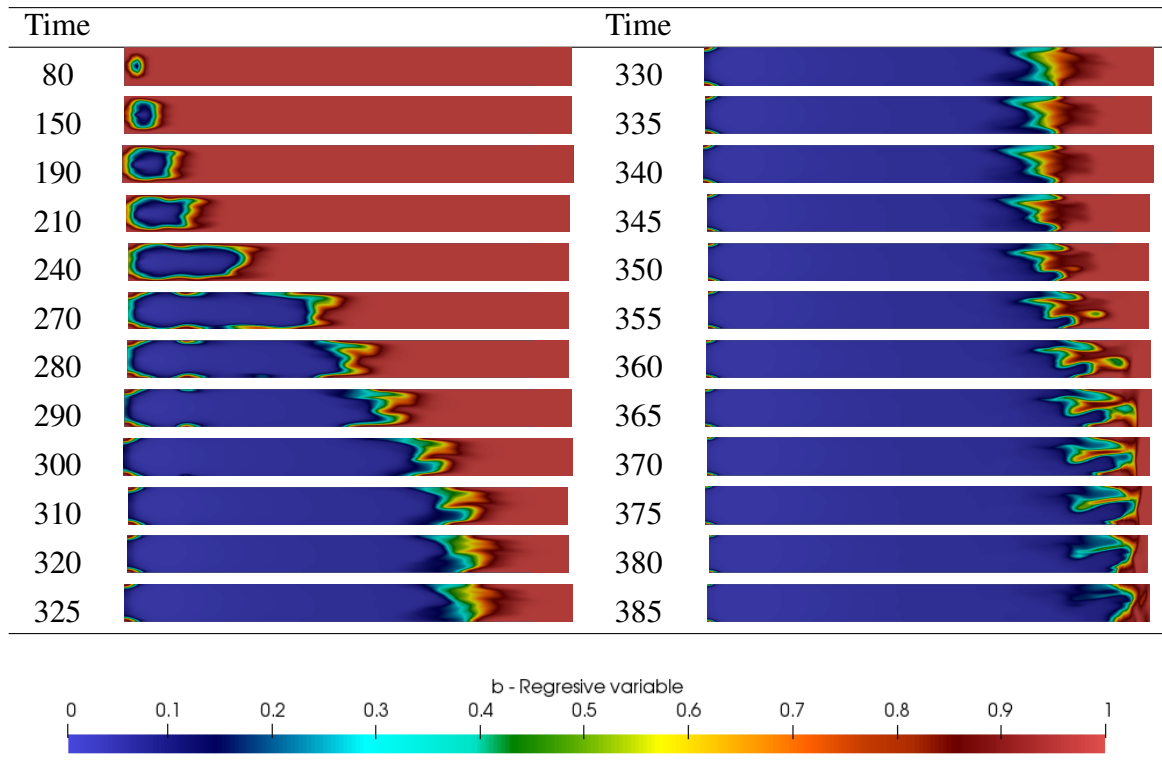
Figure 7.8: Flame propagation by regressive variable in section I of a mixture with $\Phi = 0.7$
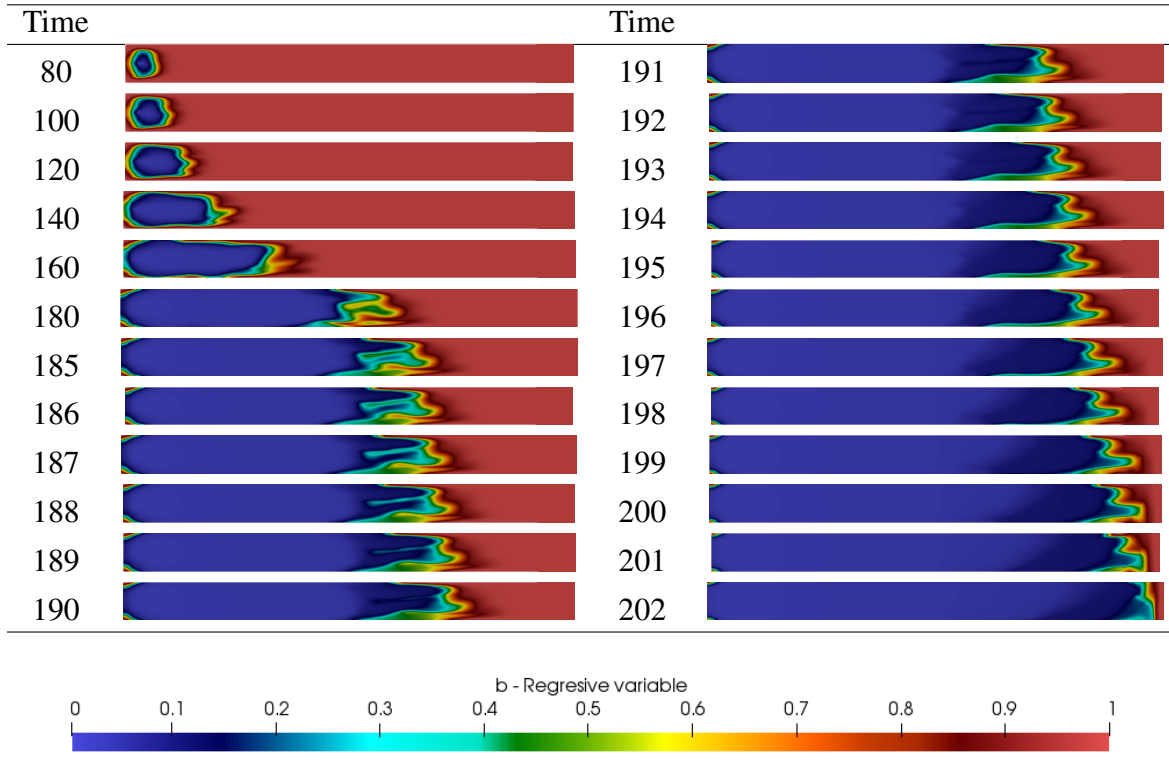
Figure 7.9: Flame propagation by regressive variable in section I of a mixture with $\Phi = 0.8$

The simulation result with $\Phi = 0.7$ does not have the propagation which crosses the bent region of the T-pipe. The lean inhomogeneous simulations $\Phi = 0.7$ and 0.8 show the hemispherical flame front as well as an elongation of the finger-shape and the closure of the elongation near the bent region. The flame propagation is detailed by frame time for $\Phi = 0.7$ and 0.8, respectively.

- The flame propagation elongation happens at frame time 270 s and 160 s.

- The flame elongation closes at frame time 375 s and 200 s.

- The flame reaches the bent region at frame time 380 s and 201 s.

Lean mixtures by turbulent flame speed and its vector estimation in section I are displayed Figure 7.10 and Figure 7.11.

Figure 7.10: Flame propagation by turbulent flame speed and vector flame speed in section I of a mixture with $\Phi = 0.7$

Time	St (Flame)	St (Vector)
80		
100		
120		
140		
160		
180		
185		
186		
187		
188		
189		
190		
191		
192		
193		
194		
195		
196		
197		
198		
199		
200		
201		
202		

St - Turbulent Flame Speed (m/s)

0 1 2 3 4 5 6 7 8 9 10 11 12 13 14 15 16 17 18 19 20
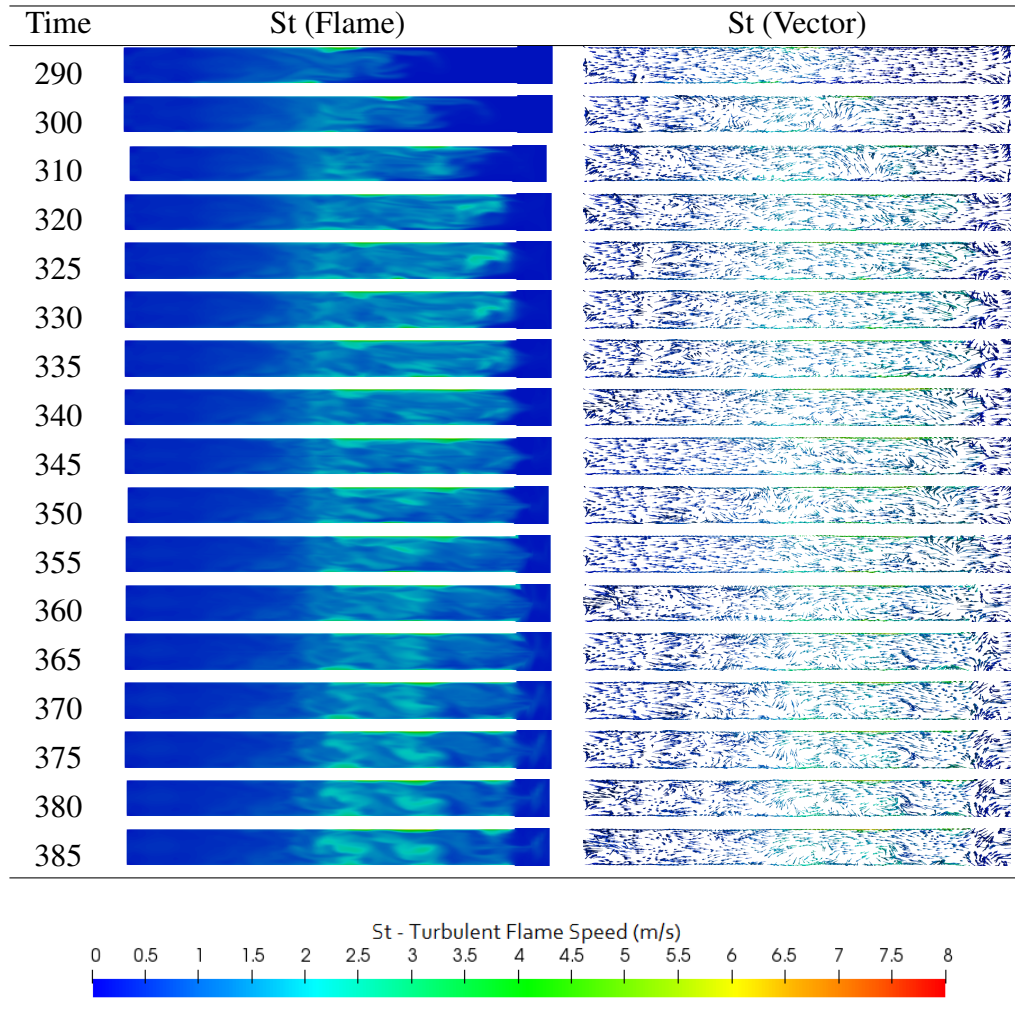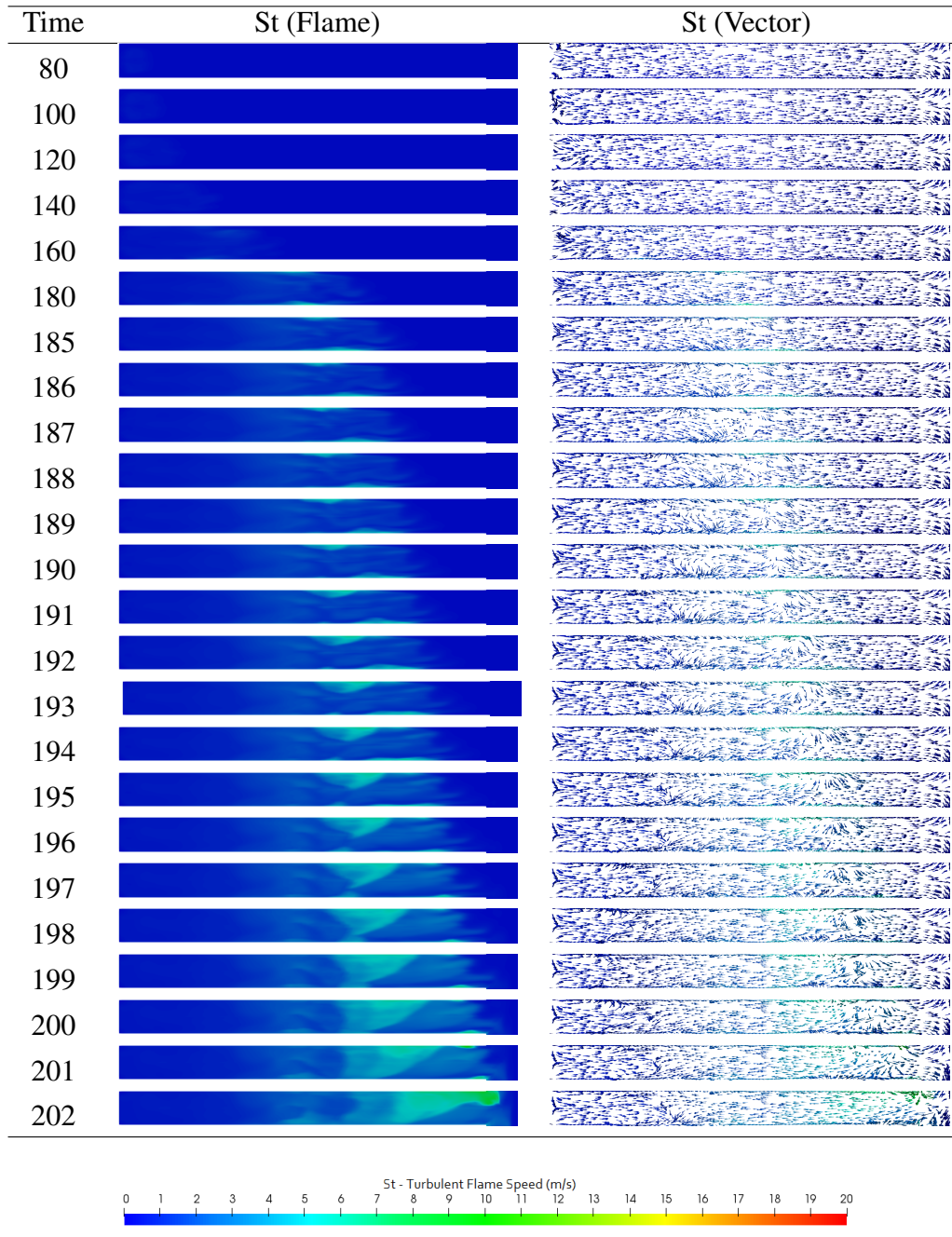
Figure 7.11: Flame propagation by turbulent flame speed and vector flame speed in section I of a mixture with $\Phi = 0.8$

The lean inhomogeneous simulations $\Phi = 0.7$ and 0.8 with boundary conditions as wall have two increases of the flame speed and two reverse propagations behind the flame front. The flame propagation is detailed by time frame for $\Phi = 0.7$ and 0.8, respectively.

- The flame speeds increase between 3 m/s and 4 m/s at frame time 290 s and 8 m/s and 9 m/s at frame time 190 s.

- The first reverse propagation behind the flame front happens at frame time 300 s and 194 s.

- The flame speeds increase again between 4 m/s and 5 m/s at frame time 340 s and 10 m/s and 11 m/s at frame time 198 s.

- The second reverse propagation behind the flame front happens at frame time 380 s and 202 s.

The mixtures with $\Phi = 0.8$ by turbulent flame speed and its vector estimation in section II and III is shown in Figure 7.12.
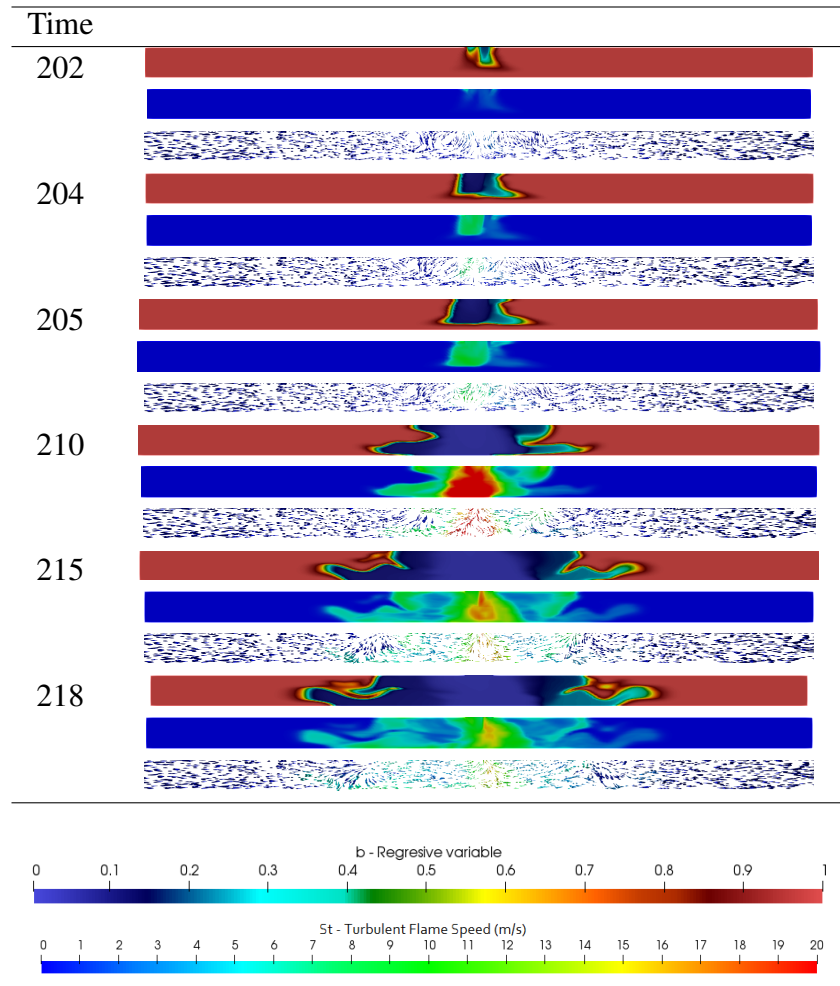

Figure 7.12: Flame propagation by regressive variable, turbulent flame speed and vector flame speed in section II and III of a mixture with $\Phi = 0.8$

The flame propagation of the inhomogeneous mixture $\Phi = 0.8$ shows an equal increase of the flame speed when the flame front reaches section II and III. The flame front tends to propagate near the bottom part of the wall as observed in the experiments. There is a vorticity formation in both directions and reverse propagation into section I. The flame front continues with a regressive variable around 0.35 until 0.6. And the region behind the flame front has a regressive variable around 0. The flame propagation of inhomogeneous $\Phi = 0.9$ with a wall as the boundary condition is detailed by frame time.

- The flame speed increases from 10 m/s to 13 m/s at frame time 204 s in section II and III.

- A reverse propagation occurs into section I with a speed of around 20 m/s at frame time 210 s.

- The simulation stops when the unburnt fluid in the domain reaches the outlet wall and the flame does not propagate further. The flame stops at frame time 218 s and with a pressure 0.267 bar, see Figure 7.29.

The stoichiometric inhomogeneous mixture by regressive variable in section I is shown in Figure 7.14.

Figure 7.13: Flame propagation by regressive variable in section I of a mixture for $\Phi = 1.0$

The turbulent flame speed and its vector estimation in section I are shown in Figure 7.14.
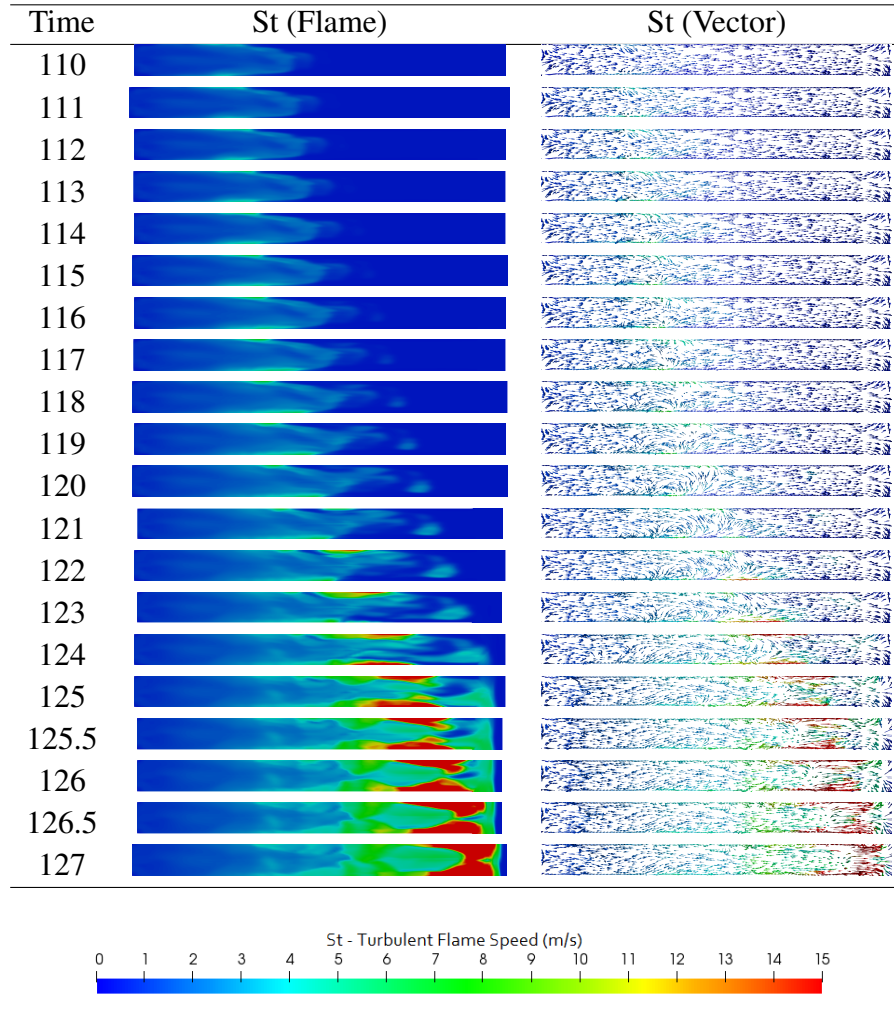
Figure 7.14: Flame propagation by turbulent flame speed and vector flame speed in section I of a mixture with $\Phi = 1.0$

The flame propagation of inhomogeneous simulations $\Phi = 1.0$ is detailed by the time frame.

- The flame speed increases between 7 m/s at frame time 110 s.

- The elongation starts at frame time 117 s.

- The first reverse propagation behind the flame front happens at frame time 119 s.

- The flame speed increases again between 11 m/s and 12 m/s at frame time 125 s.

- The flame elongation closes at frame time 125.5 s.

- The second reverse propagation behind the flame front happens at frame time 126 s.

- The reverse propagation speed is around 15 m/s.

The stoichiometric inhomogeneous mixture by regressive variable, turbulent flame speed, and its vector estimation in section II and III is shown in Figure 7.15.
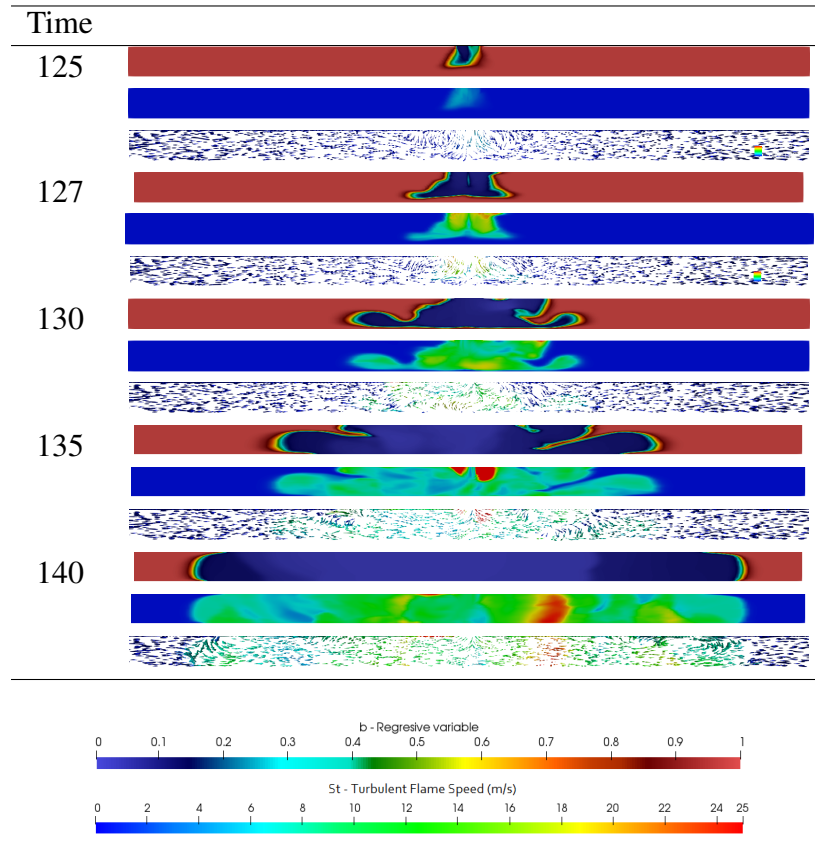
Figure 7.15: Flame propagation by regressive variable, turbulent flame speed and vector flame speed in section II and III of a mixture with $\Phi = 1.0$

The stoichiometric mixture flame propagation shows also an equal increase of the flame speed when the flame front reaches section II and III. The flame propagates also near the bottom part of the wall and there is a reverse propagation into section I. The vorticity appears in both directions. The flame front continues with a regressive variable around 0.35 until 0.6. And the region behind has a regressive variable around 0. The flame propagation of $\Phi = 1.0$ with a wall as the boundary condition is detailed by frame time.

- The flame speed increases from 15 m/s to 20 m/s at frame time 127 s in section II and III.

- A reverse propagation occurs into section I with a speed of around 14 m/s at frame time 130 s.

- The flame stops at frame time 140 s and with a pressure 0.385 bar, see Figure 7.29.

The rich mixtures by regressive variable in section I are shown in Figure 7.16, Figure 7.17, Figure 7.18 and Figure 7.19.
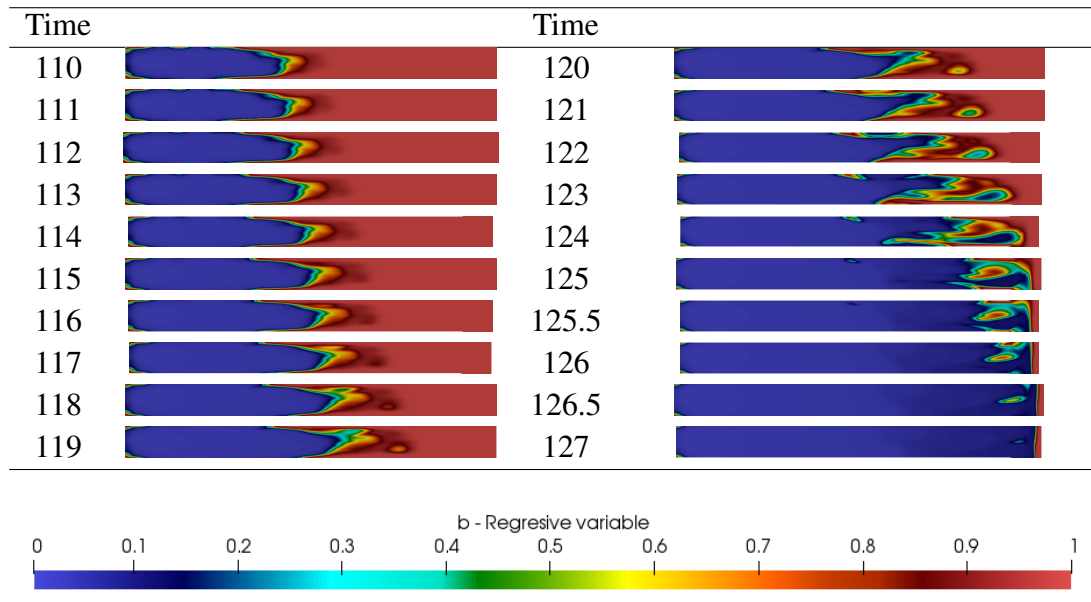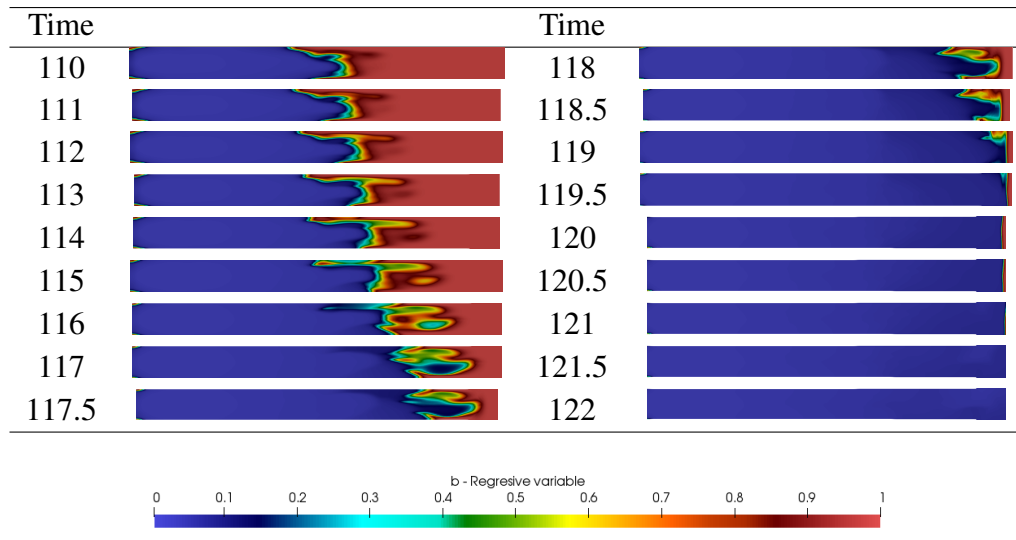

Figure 7.16: Flame propagation by regressive variable in section I of a mixture with $\Phi = 1.1$
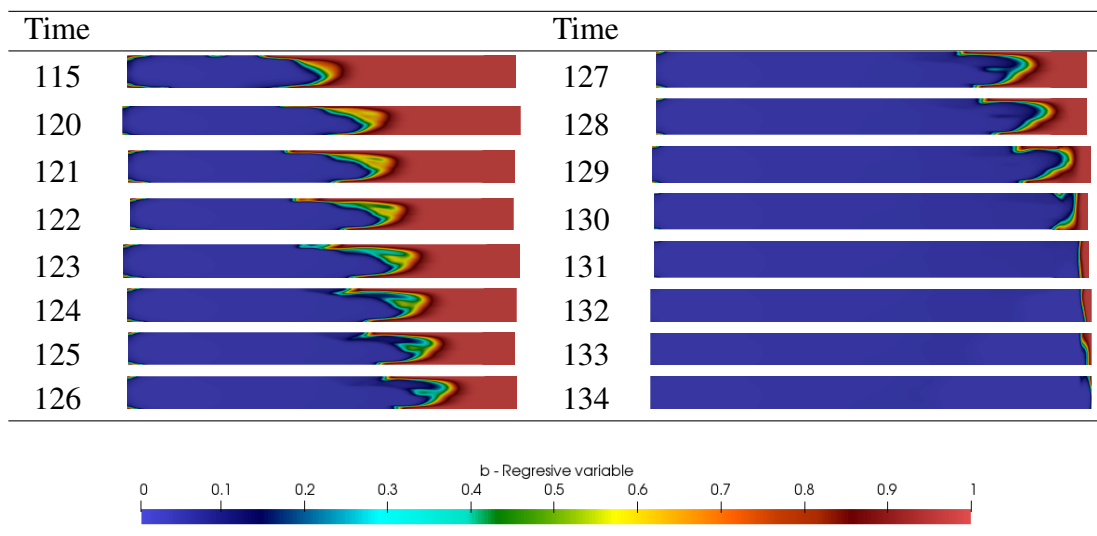
Figure 7.17: Flame propagation by regressive variable in section I of a mixture with $\Phi = 1.2$
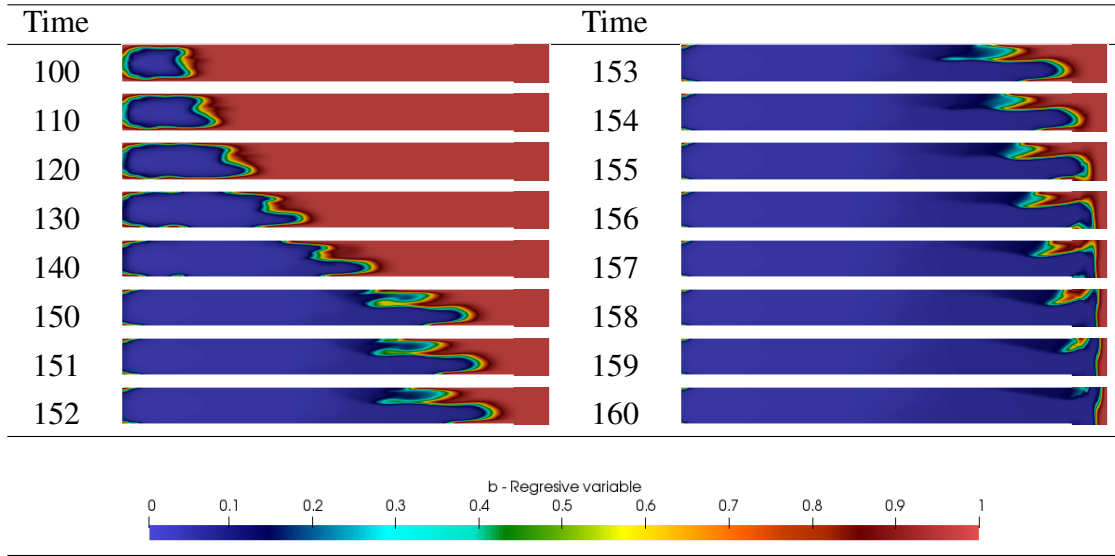
Figure 7.18: Flame propagation by regressive variable in section I of a mixture with $\Phi = 1.3$
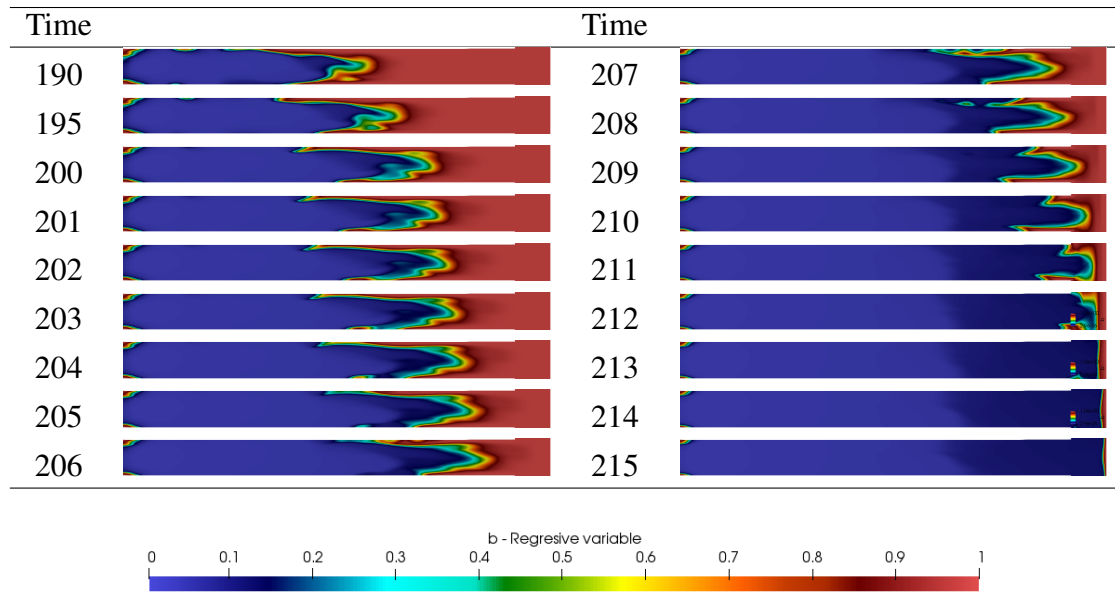
Figure 7.19: Flame propagation by regressive variable in section I of a mixture with $\Phi = 1.4$

The rich inhomogeneous simulations $\Phi = 1.1, 1.2, 1.3$ and 1.4 show also a hemispherical flame front as well as an elongation of the finger-shape and the closure of the elongation near the bent region. The flame propagation is detailed by time frame for $\Phi = 1.1, 1.2, 1.3$ and 1.4, respectively.

- The flame propagation elongation happens at frame time 111 s, 122 s, 130 s, and 190 s.

- The flame elongation closes at frame time 118 s, 128 s, 154 s, and 208 s.

- The flame reaches the bent region at frame time 118.5 s, 129 s, 156 s, and 210 s.

The rich mixtures by turbulent flame speed and its vector estimation in section I are shown in Figure 7.20, Figure 7.21, Figure 7.22 and Figure 7.23.

Figure 7.20: Flame propagation by turbulent flame speed and vector flame speed in section I of a mixture with $\Phi = 1.1$

Time	St (Flame)	St (Vector)
115		
120		
121		
122		
123		
124		
125		
126		
127		
128		
129		
130		
131		
132		
133		
134		
135		

St - Turbulent Flame Speed (m/s)

0 1 2 3 4 5 6 7 8 9 10 11 12 13 14 15

Figure 7.21: Flame propagation by turbulent flame speed and vector flame speed in section I of a mixture with $\Phi = 1.2$

Time	St (Flame)	St (Vector)
100		
110		
120		
130		
140		
150		
151		
152		
153		
154		
155		
156		
157		
158		
159		
160		

St - Turbulent Flame Speed (m/s)

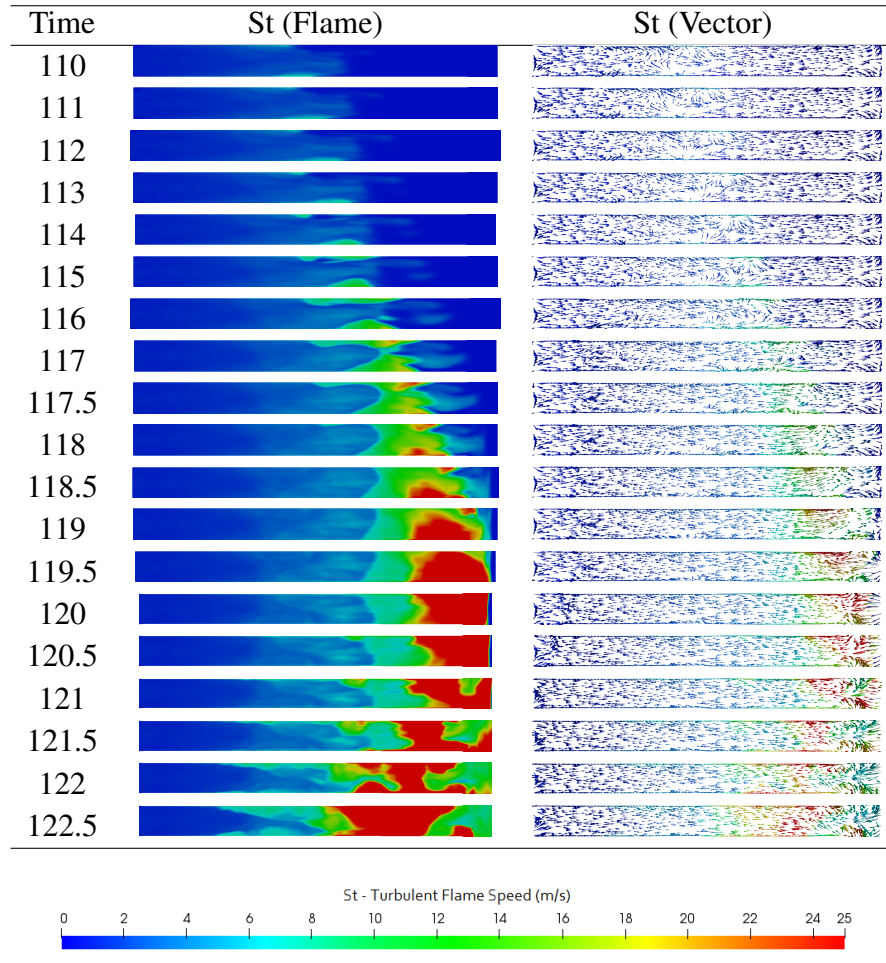0   1   2   3   4   5   6   7   8   9   10   11   12

Figure 7.22: Flame propagation by turbulent flame speed and vector flame speed in section I of a mixture with $\Phi = 1.3$

Figure 7.23: Flame propagation by turbulent flame speed and vector flame speed in section I of a mixture with $\Phi = 1.4$

The rich inhomogeneous simulations $\Phi = 1.1$, 1.2, 1.3, and 1.4 show two increases of the flame speed and two reverse propagations. The flame propagation is detailed by time frame for $\Phi = 1.1$, 1.2, 1.3 and 1.4, respectively.

- The flame speed increases at frame time 110 s to around 8 m/s, 115 s to around 6 m/s, 130 s to around 5 m/s, and 190 s to around 4 m/s.

- The first reverse propagation behind the flame front happens at frame time 115 s, 122 s, 150 s, and 203 s, respectively

- The flame speed increases again at frame time 118 s to around 16 m/s, 127 s to around 10 m/s, 154 s to around 9 m/s and 208 s to around 8 m/s.

- The second reverse propagation happens behind the flame front at frame time 118.5 s to around 25 m/s, 129 s to around 15 m/s , 156 s to around 9 m/s and 210 s to around 8 m/.

The rich mixtures by regressive variable, turbulent flame speed and its vector estimation in section II and III are shown in Figure 7.24, Figure 7.25, Figure 7.26 and Figure 7.27.

Figure 7.24: Flame propagation by turbulent flame speed and vector flame speed in section II and III of a mixture with $\Phi = 1.1$
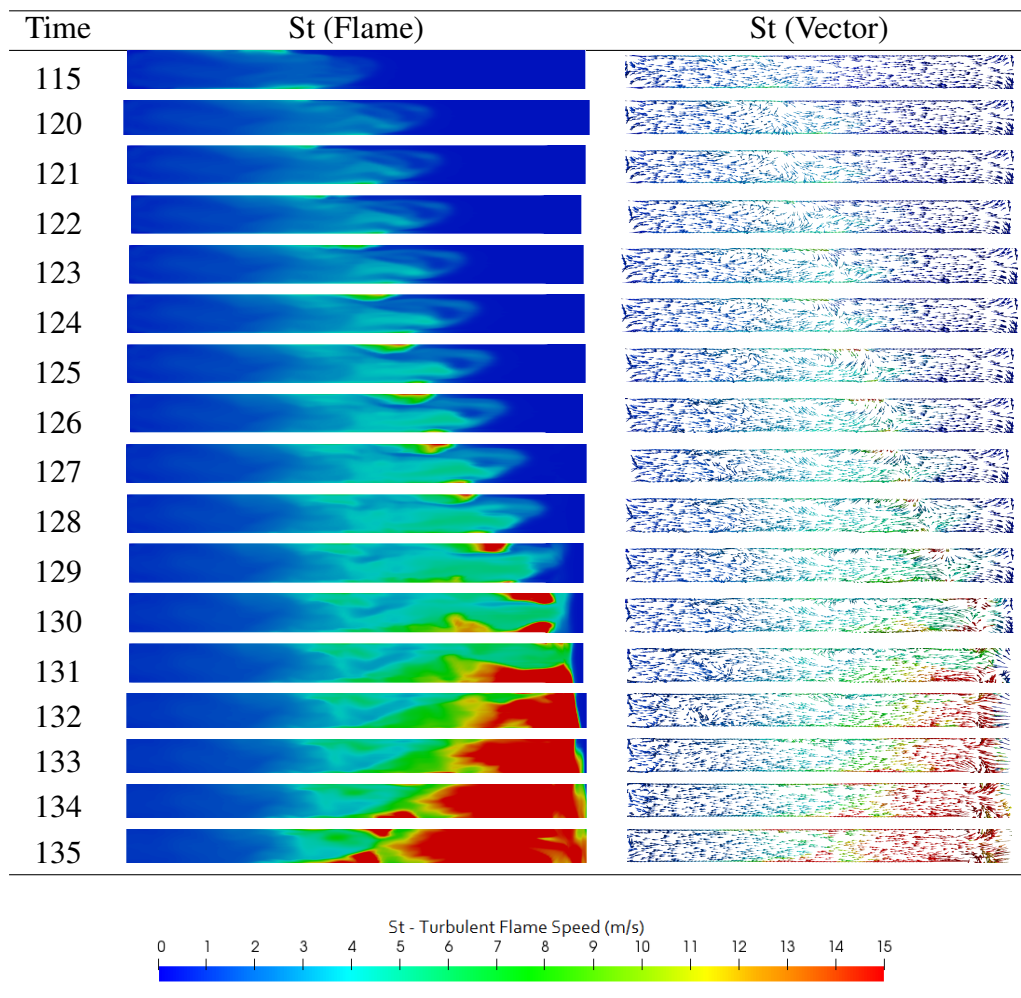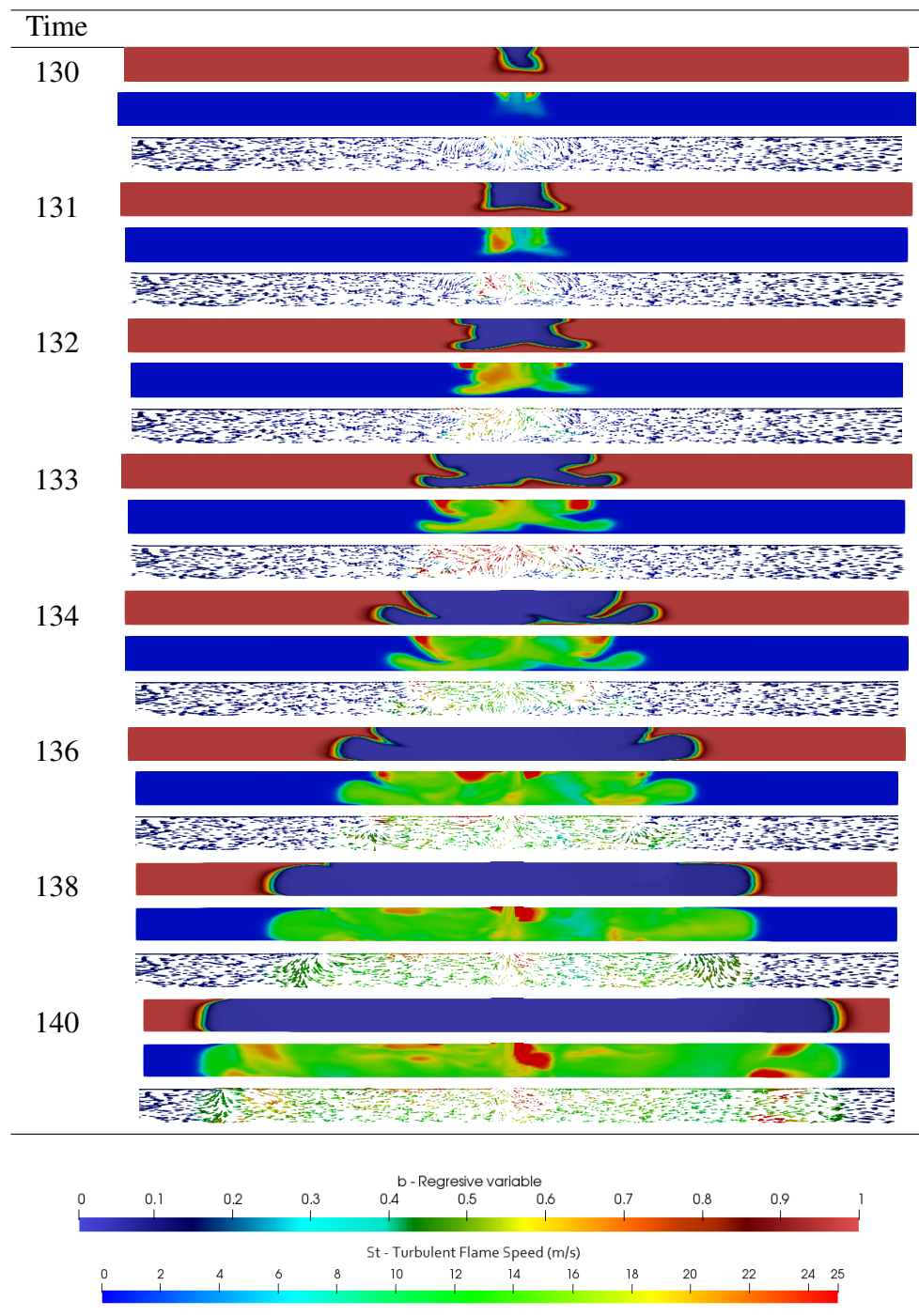
Figure 7.25: Flame propagation by turbulent flame speed and vector flame speed in section II and III of a mixture with Φ = 1.2
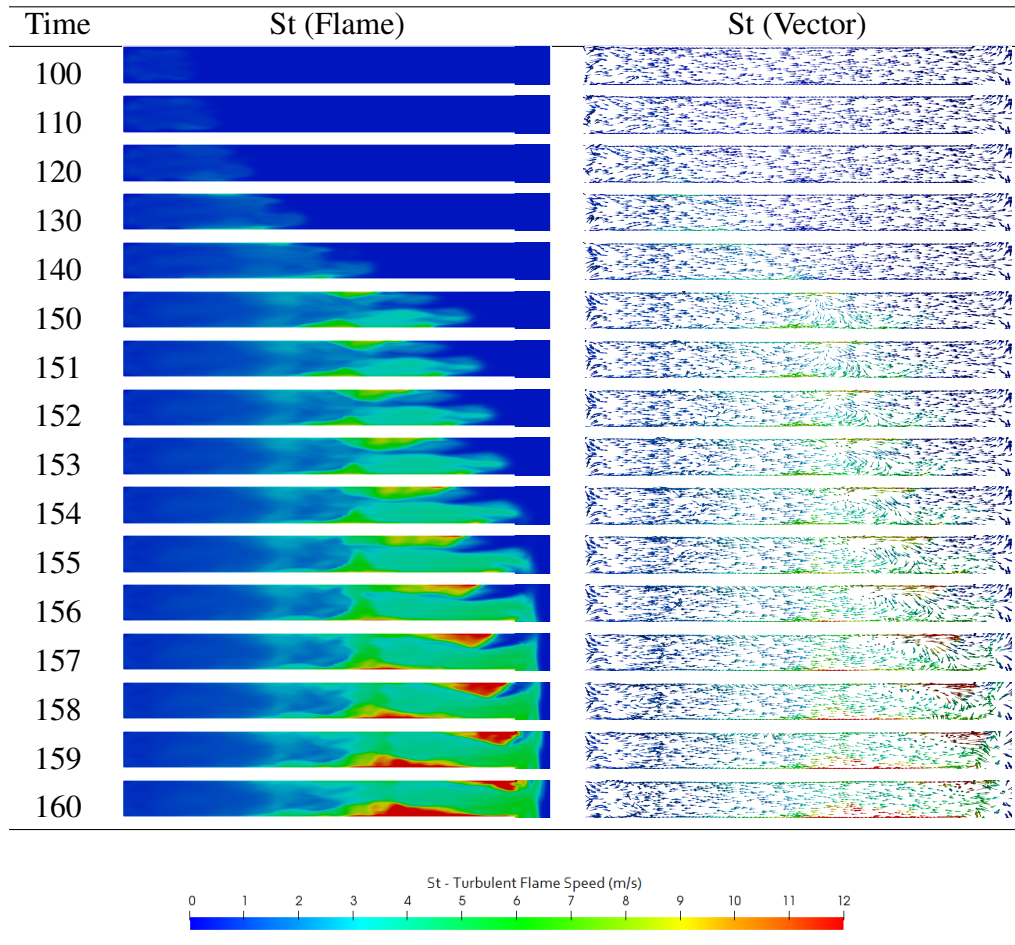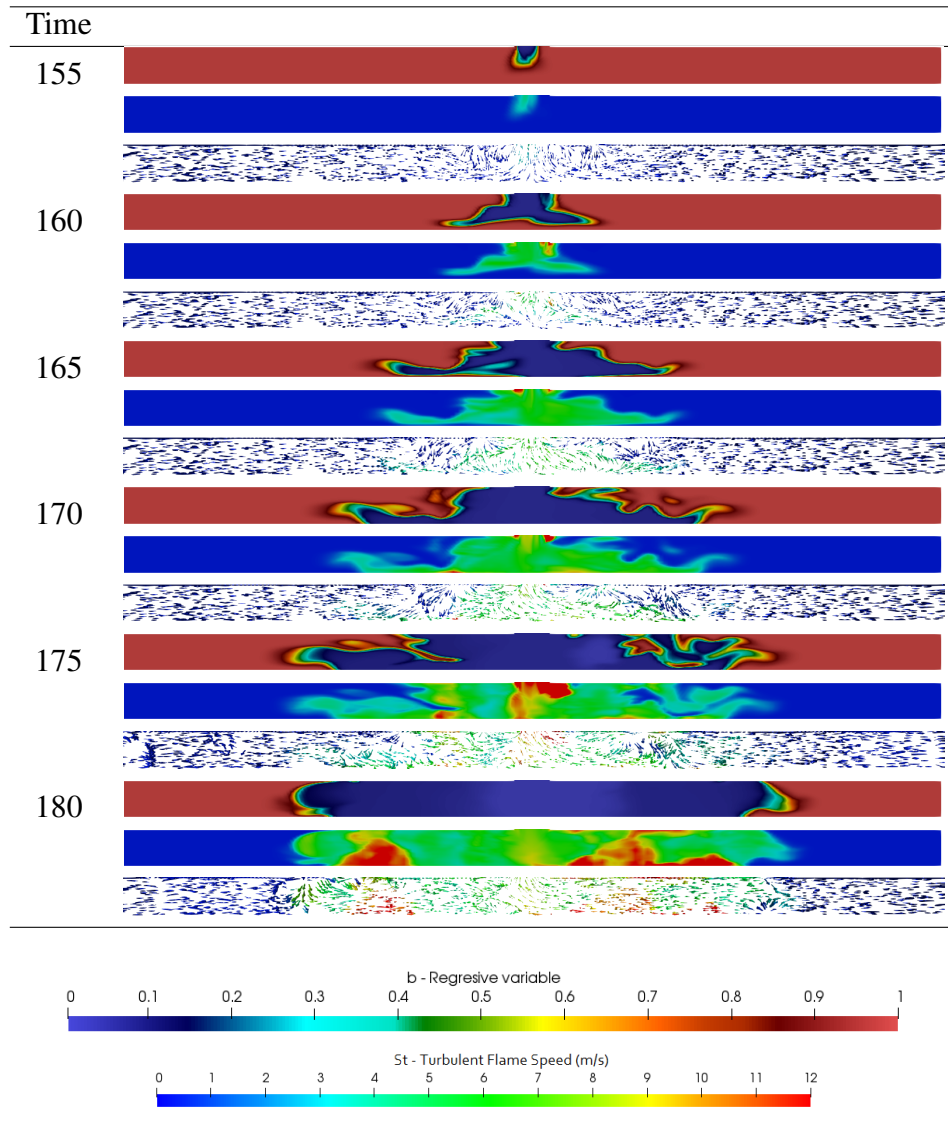
Figure 7.26: Flame propagation by turbulent flame speed and vector flame speed in section II and III of a mixture with $\Phi = 1.3$
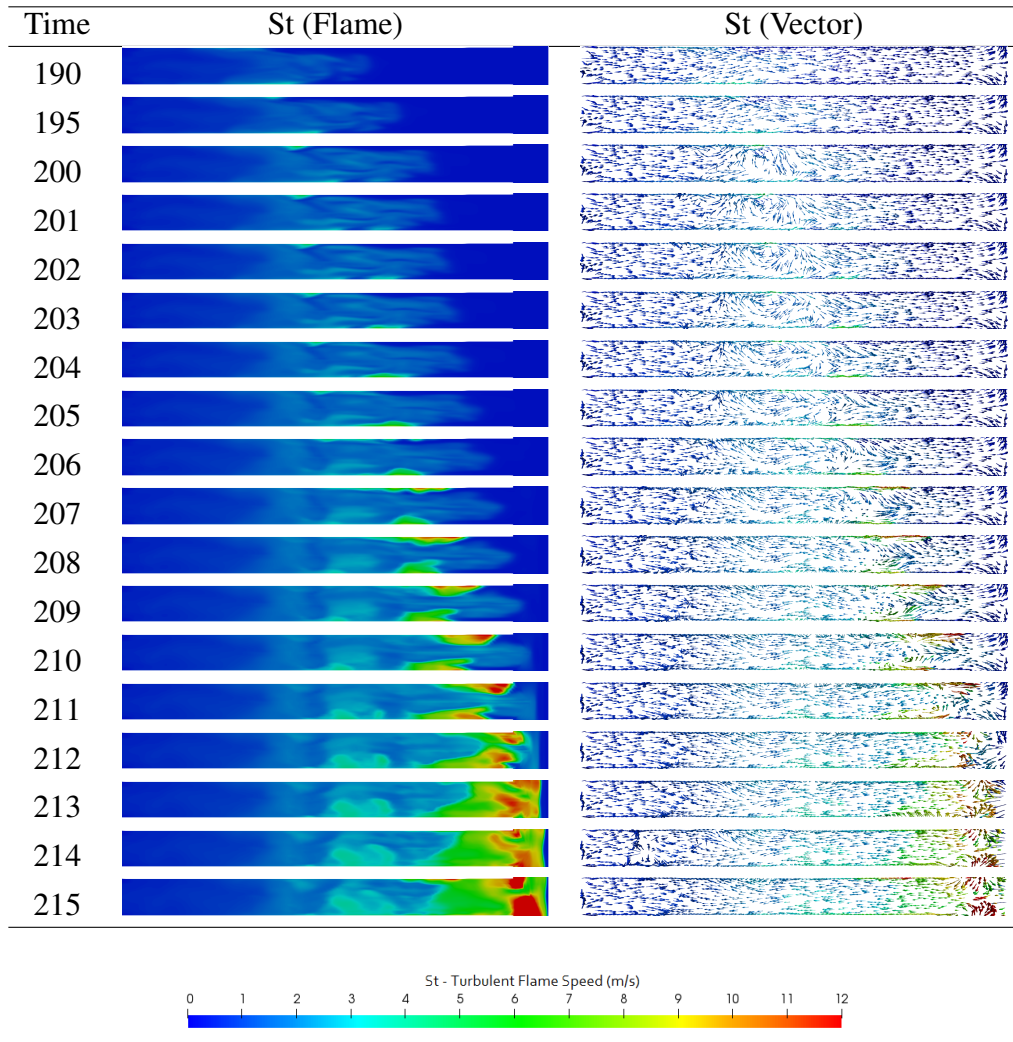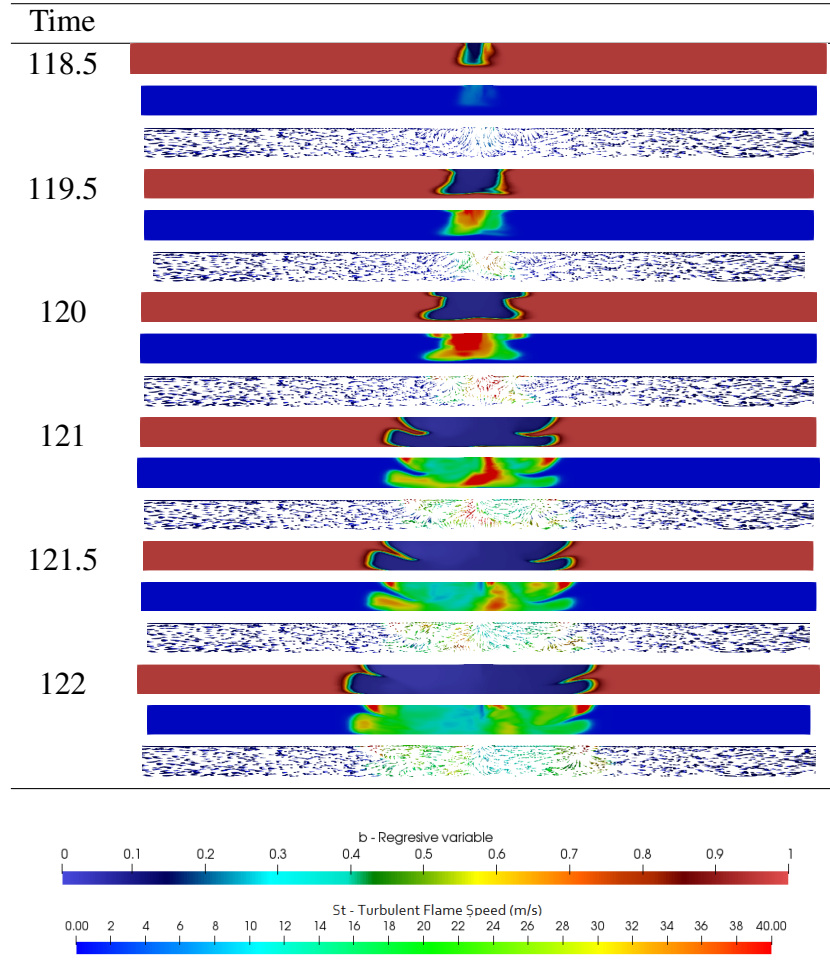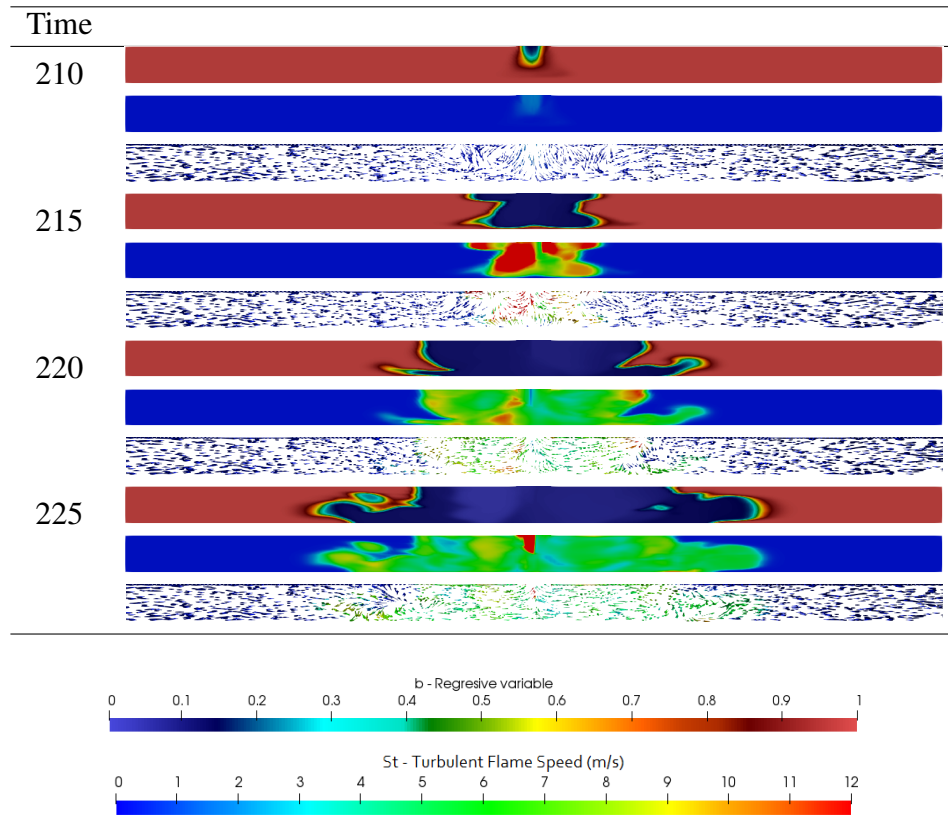
Figure 7.27: Flame propagation by turbulent flame speed and vector flame speed in section II and III of mixture with $\Phi = 1.4$

In the rich mixtures simulations $\Phi = 1.1$, 1.2, 1.3, and 1.4 appear a flame speed equality growth from section I into section II and III. The flame front tends to propagate near the bottom part of the wall. The vorticity formation is developed during the flame propagation. There is a reverse propagation from section II and III into section I. The flame front continues with a regressive variable around 0.35 until 0.6. And the region behind the flame front has a regressive variable around 0. The flame propagation of rich mixtures with a wall as the boundary condition is detailed by frame time $\Phi = 1.1$, 1.2, 1.3 and 1.4, respectively .

- The flame propagation from section I into section II and III increases around 16 m/s into 24 m/s at frame time 121 s, 10 m/s into 18 m/s at frame time 134 s, 8 m/s into 10 m/s at frame time 165 s and from 8 m/s into 9 m/s at frame time 220 s.

- The flame stops at frame time 122 s, 140 s, 180 s, and 225 s.

- The pressure is 0.365 bar, 0.309 bar, 0.307 bar and 0.270 bar, see Figure 7.29.

7.1.1 Regressive Variable, Temperature and Pressure

The average value of the regressive variable variation of each simulation where the flame propagation crosses the bent region is plot by time as displayed in Figure 7.28.
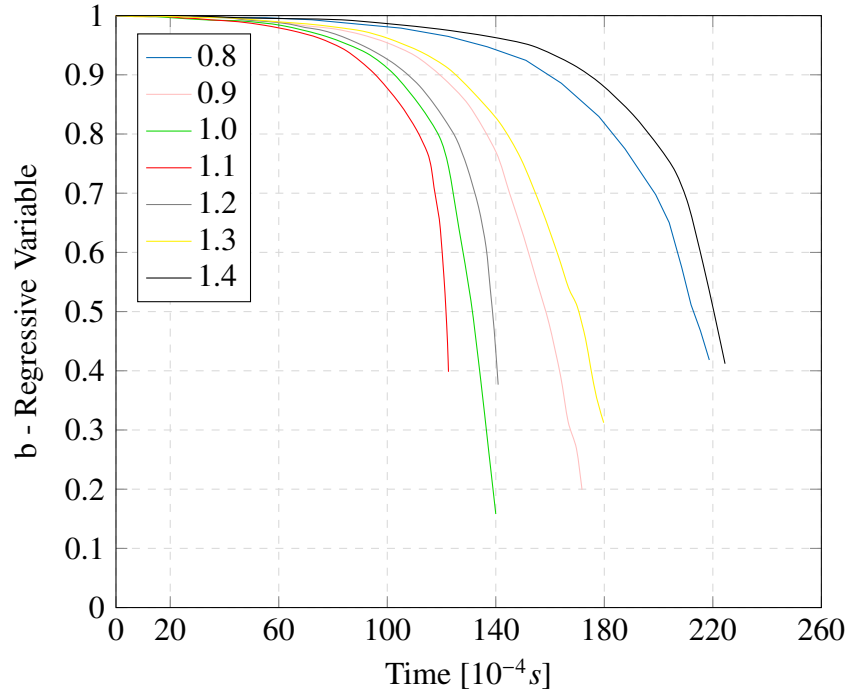
Figure 7.28: Regressive variable of premixed flame propagation of methane-air mixtures by time

b tends to deplete during the flame propagation. The methane-air mixture does not react completely, because it is an inhomogeneous mixture and the simulation stops before the flame reaches the outlet walls.

The pressure variation during the flame propagation is estimated by time, see Figure 7.29. The pressure obtained from the experiments is plotted together with the highest pressure from the numerical results by methane-air concentration, Figure 7.30.
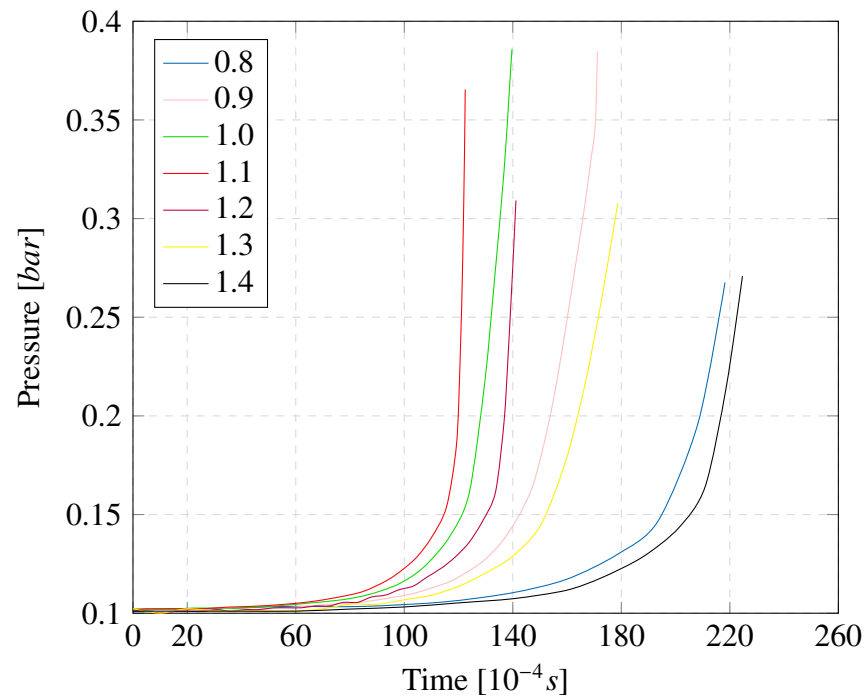
Figure 7.29: Pressure of premixed flame propagation of methane-air mixtures by time
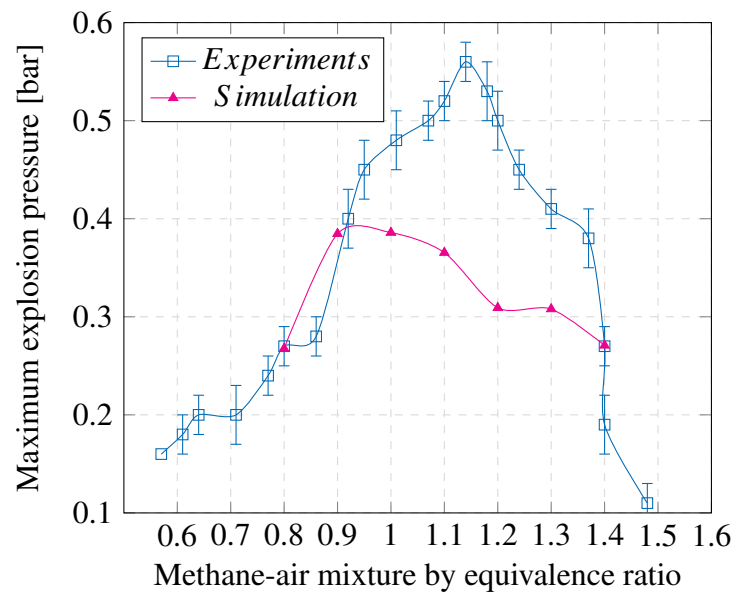
Figure 7.30: Experimental and numerical pressure of premixed flame propagation of methane-air mixtures by equivalence ratio

Figure 7.30 shows that pressure from the numerical investigation has a scale similar to the measured average maximum explosion pressure of the experiments. The pressure variation from the CFD simulation also has an increase from the lean mixtures into the rich mixture, where the highest pressure is near the stoichiometric concentration. The adiabatic flame temperature is analyzed only in section I. The flame propagation by adiabatic flame temperature is shown in Figure 7.31, Figure 7.32 and Figure 7.33.
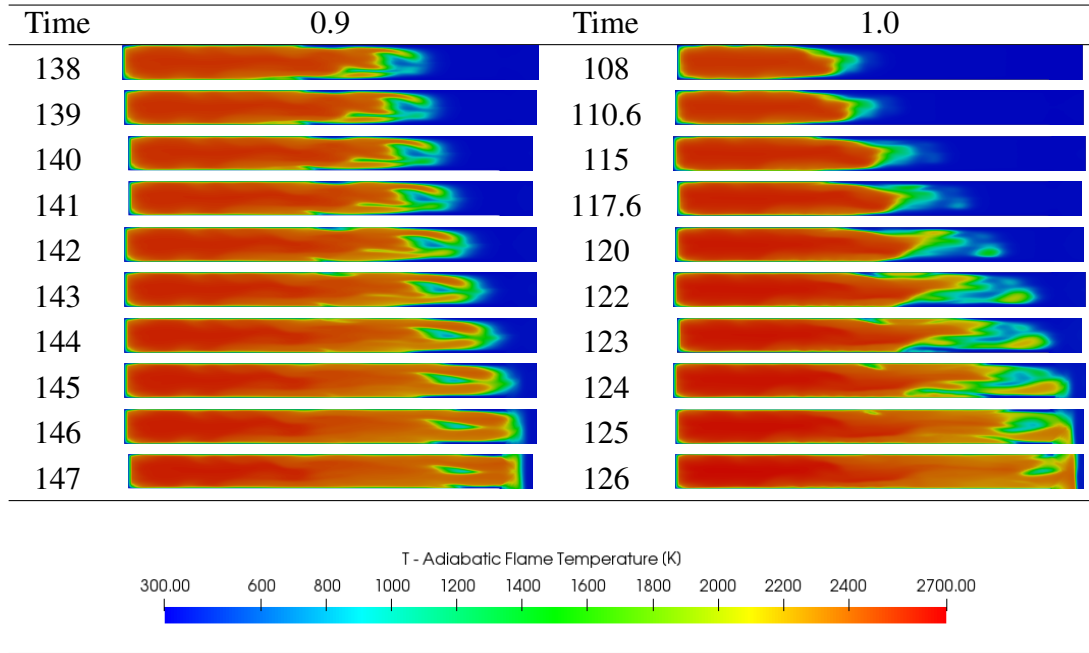
Figure 7.31: Flame propagation by adiabatic flame temperature in section I of mixtures with $\Phi = 0.9$ and 1.0
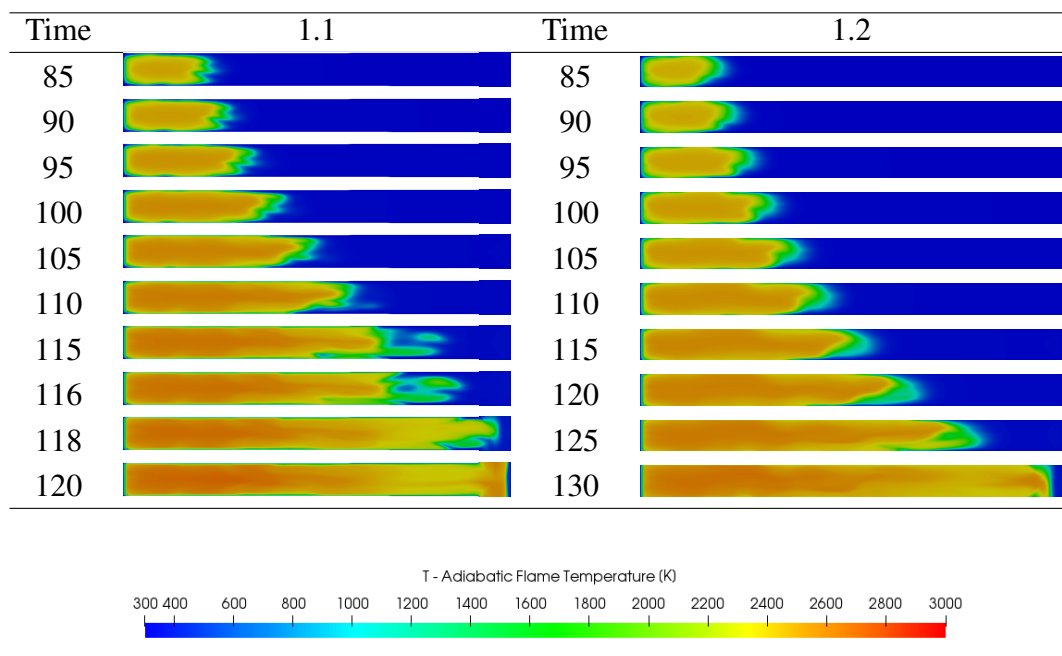
Figure 7.32: Flame propagation by adiabatic flame temperature in section I of mixtures with Φ = 1.1 and 1.2
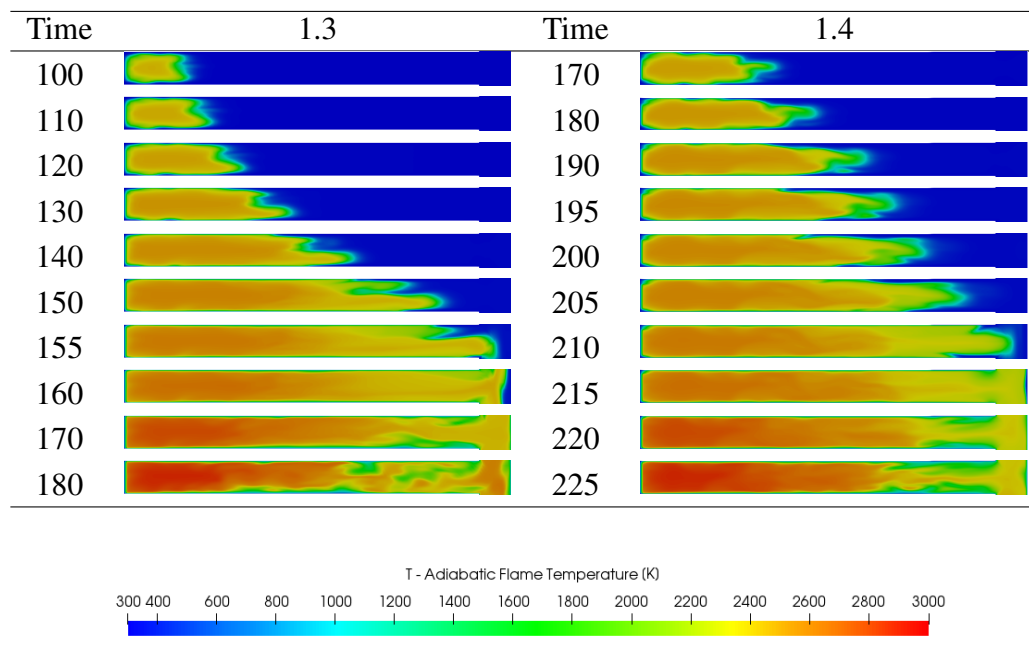
Figure 7.33: Flame propagation by adiabatic flame temperature in section I mixtures with Φ = 1.3 and 1.4

The flame temperature of the simulations shows a similar temperature in comparison to the adiabatic flame temperature estimated as shown in Figure 2.2. The region behind the flame front has a higher temperature than the flame front during the flame propagation which defines the reaction continuing after the flame front crosses the region. A similar phenomenon happens with the experimental results where the flame brightness increased directly corresponding to the temperature growth when the flame front already crosses the region.

7.2 Numerical Analysis of T-pipe with Obstacles

The numerical investigation of the T-pipe with obstacles focuses on the analysis of the flame propagation between the obstacles and the bent region. The CFD simulations performed are separated by homogeneous and inhomogeneous and each mixture is simulated by the boundary conditions as wall and piston. The numerical simulation has flame propagation results where the flame crosses the bent region only in $\Phi = 0.9, 1.0, 1.1$ and 1.2 for a homogeneous mixtures and in $\Phi = 1.0, 1.1, 1.2$ and 1.3 for inhomogeneous mixtures.

he results investigation display the flame propagation by the parameters b regressive variable, U flow velocity and flow vector velocity. The flow velocity consists of the unburned and burned region of the domain. This restricts the investigation because it is necessary to place the flame by the regressive variable and estimate the flow velocity in the area where the flame propagates.

The simulation with $\Phi = 1.2$ is chosen to compare the settings of the mixture and boundary conditions' types. The simulation with the homogeneous mixture is compared by regressive variable for the boundary conditions piston and wall as shown in Figure 7.34.

Figure 7.34: Flame propagation by flow velocity and vector flow velocity in section I of a homogeneous mixture with $\Phi = 1.2$

Figure 7.35 and Figure 7.36 show a homogeneous mixture propagation by flow velocity and vector flow velocity for the boundary conditions as piston and wall, respectively.

Figure 7.35: Flame propagation by flow velocity and vector flow velocity in section I with BC piston of a homogeneous mixture with $\Phi = 1.2$

Figure 7.36: Flame propagation by flow velocity and vector flow velocity in section I with BC wall of a homogeneous mixture with $\Phi = 1.2$

The simulation result of both boundary conditions shows a partial reaction of methane-air in the region behind the flame front. The flame propagation for both boundary conditions as a piston has b around 0.7 until 0.5 at frame time 120 s and 170 s. The region behind the flame front shows a scenario where the methane-air has a higher reaction rate with a b value around 0.3 for the boundary condition as piston and 0.5 for the boundary condition as a wall. The flow velocity and the vector velocity of the flame has a value around 300 m/s at frame time 180 s and the vorticity formation between the obstacles have a value around 120 m/s in both

simulations.

The boundary conditions wall and piston are analyzed by the regressive variable of the inhomogeneous mixture simulations as shown in Figure 7.37.
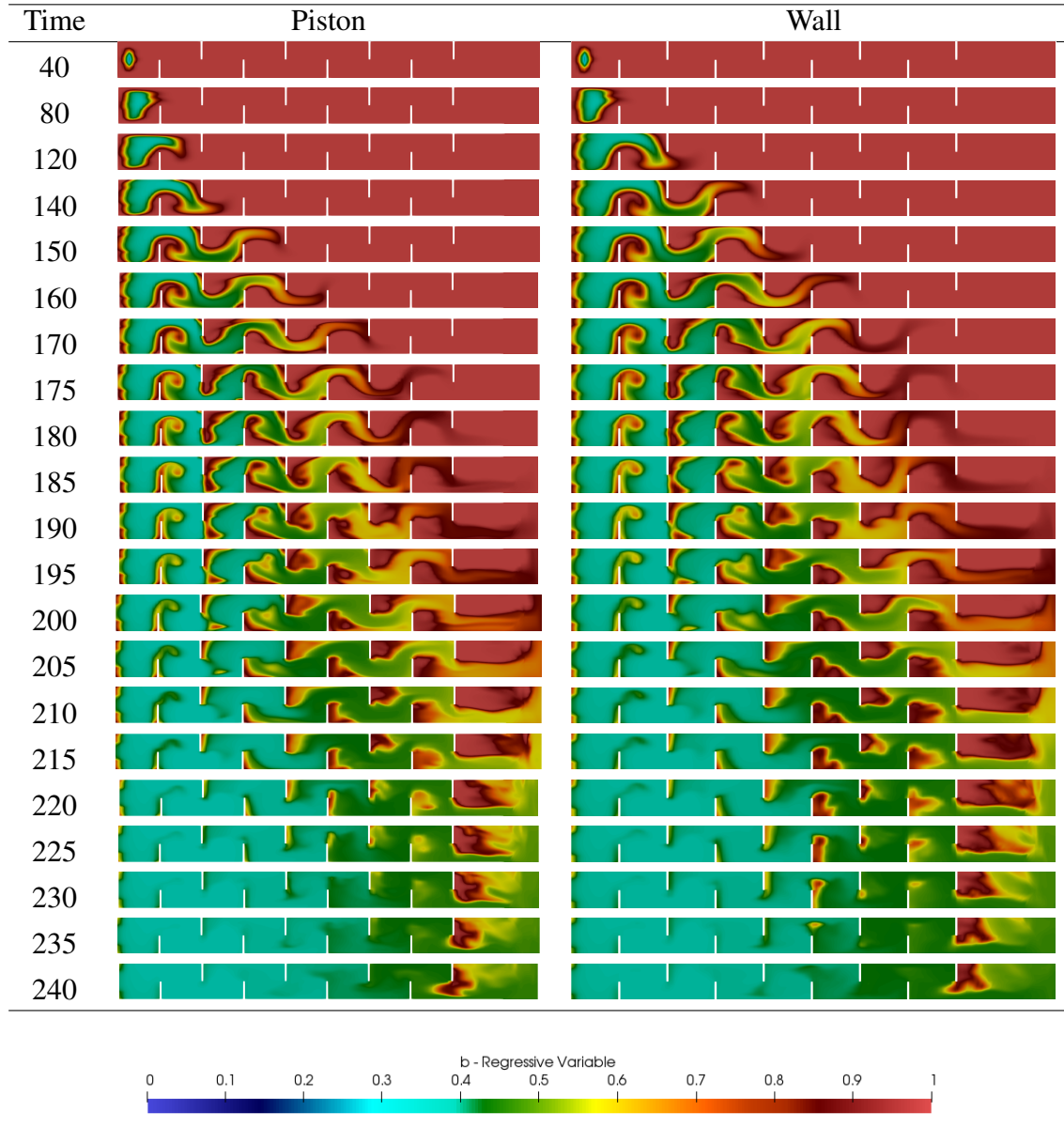
Figure 7.37: Flame propagation by regressive variable in section I of an inhomogeneous mixture with $\Phi = 1.2$

The flame propagation of both simulations using boundary conditions as wall and piston does not show a significant difference by the parameter regressive variable. b has a value around 0.7 on the flame front propagation. The flame front only fills the region between the obstacles near the explosion site as frame time 120 s indicates in both simulations. In a first instance,

further propagation of the flame until the bent region does not fill the region between the obstacles.

A methane-air reaction continues in the region behind the flame front and due to this reaction, the flame fills the region between the obstacles. The region behind the flame front has a variation of the regressive variable around 0.6 until 0.4 due to the continuity of a methane-air reaction. After the flame propagation crosses the bent region of the T-pipe, the methane-air increases the reaction rate in the region behind the flame front. Figure 7.38 and Figure 7.39 show the flow velocity and the vector flow velocity of the simulation with boundary conditions as wall and piston, respectively.
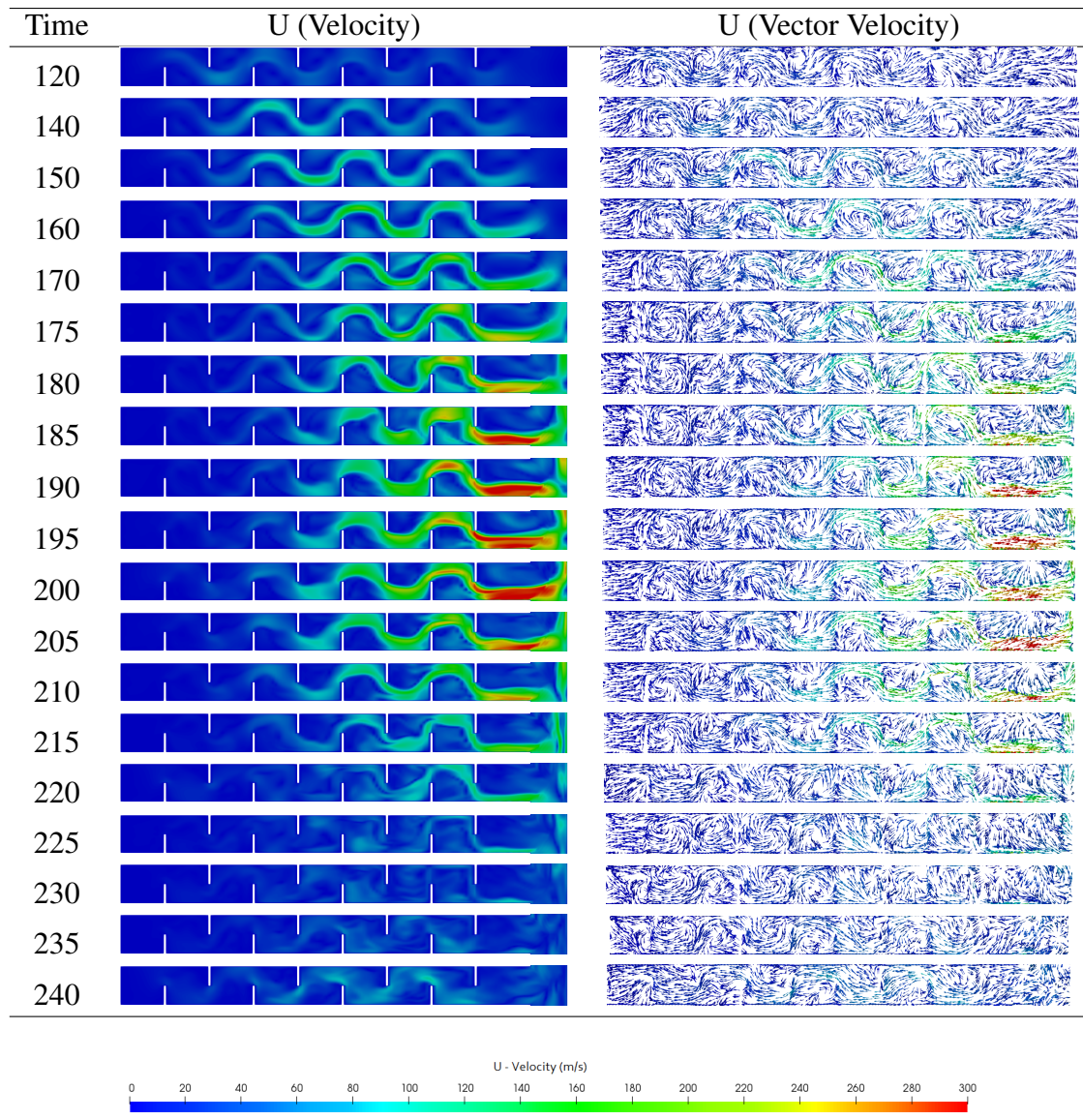
Figure 7.38: Flame propagation by regressive variable in section I with BC as piston of an inhomogeneous mixture with $\Phi = 1.2$
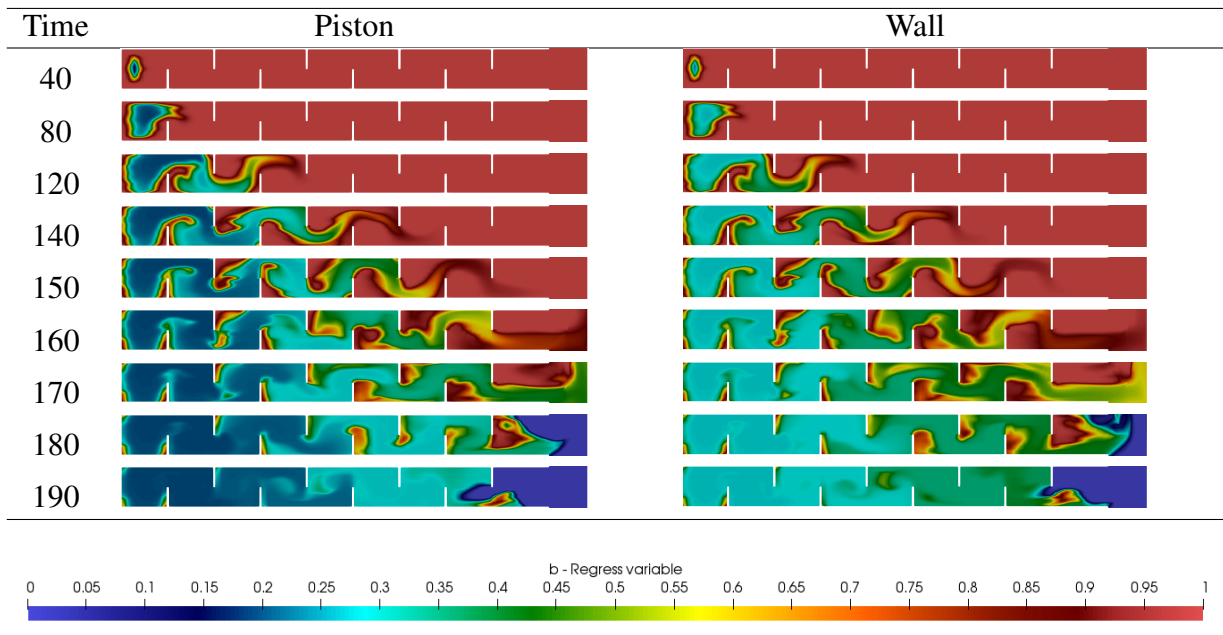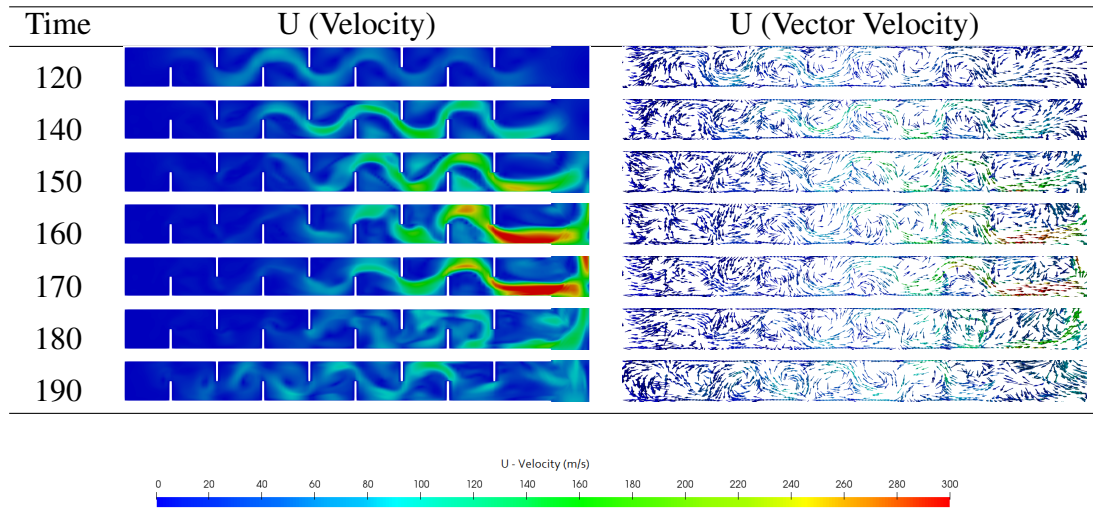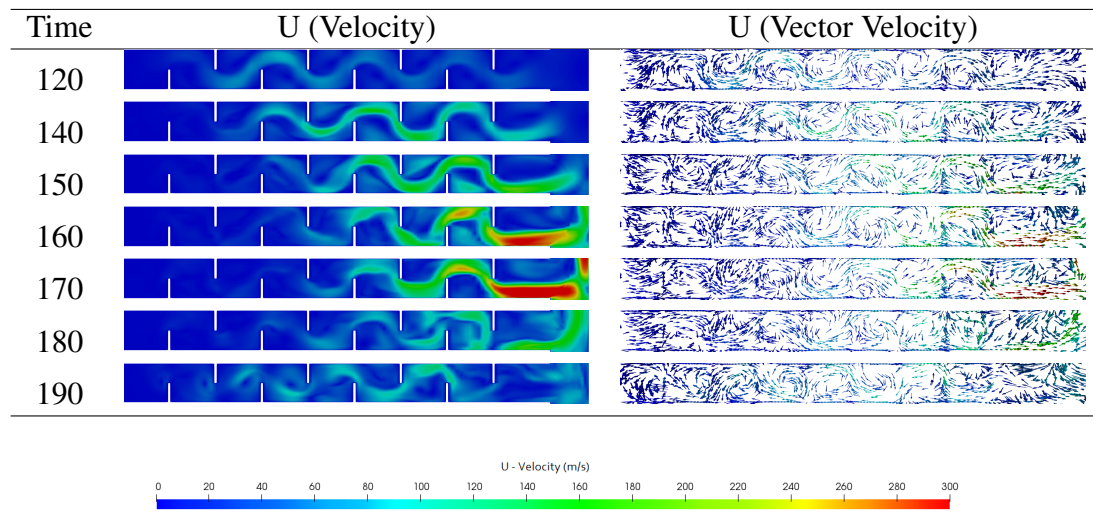
Figure 7.39: Flame propagation by flow velocity and vector flow velocity in section I with BC as wall of an inhomogeneous mixture with $\Phi = 1.2$

The flame front reaches the region between the last obstacle and bent region at frame time 195 s for both simulations. Both simulations have a similar flame velocity and vector flame velocity around 290 m/s at frame time 195 s. There is a vorticity formation between the obstacles, especially the obstacles closer to the bent region. The vorticity region has a flame velocity of around 200 m/s for both simulation.

The simulation with piston and wall does not show a significant difference by the parameters regressive variable, flow velocity, and vector flow velocity.

Further analyses use only the simulation with inhomogeneous mixtures with a wall as the boundary conditions of outlet walls. Figure 7.40 shows the flame propagation by regressive variable, flame velocity, and vector flame velocity in section II and III.

Figure 7.40: Flame propagation by regressive variable, flow velocity and vector flow velocity in section II and III of a mixture with $\Phi = 1.2$

The flame front velocity is around 300 m/s at frame time 200 s and decreases immediately at frame time 210. The simulation stops at frame time 230 s and the flame front stagnates as the frame time 240 s indicates. The flame does not propagate further after the frame time 230 s because the flow velocity in the domain reaches the outlet wall too soon and the flame stops to propagate. The stoichiometric and rich mixtures by regressive variable in section I are shown in Figure 7.41 and Figure 7.42.
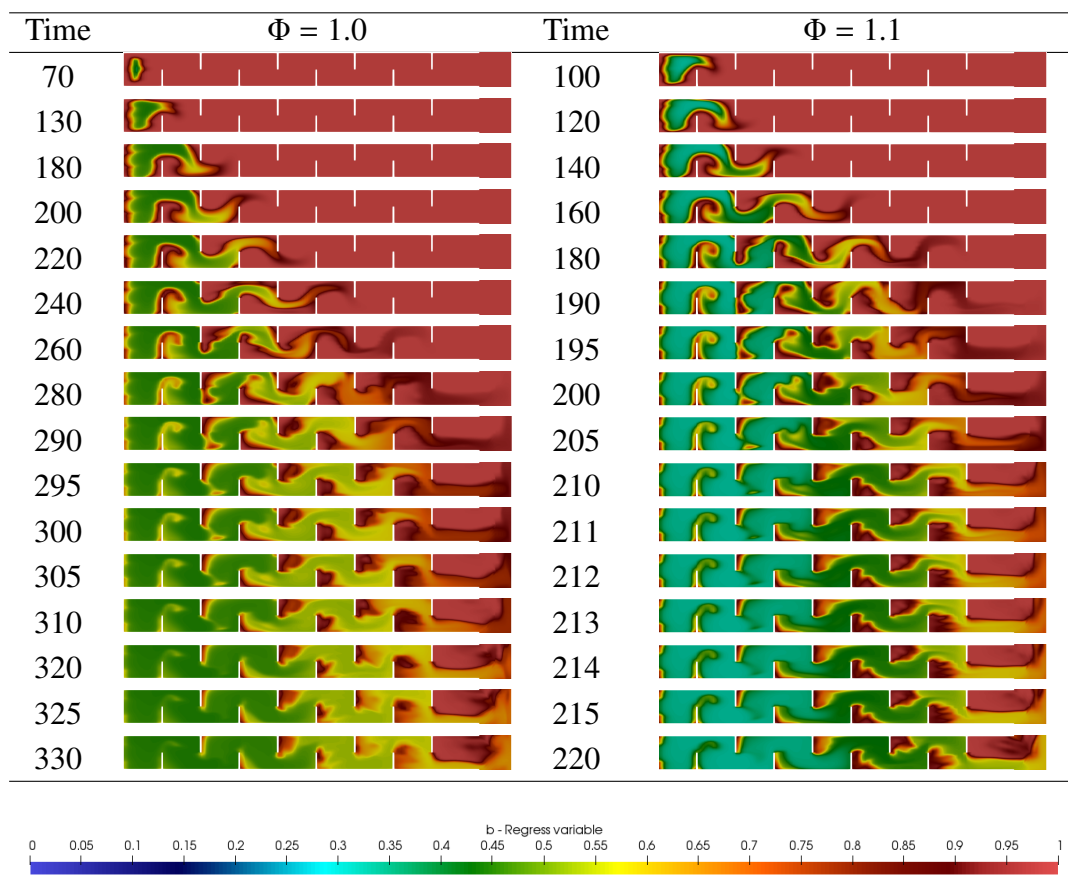
Figure 7.41: Flame propagation by regressive variable in section I of mixture with Φ = 1.0 and 1.1
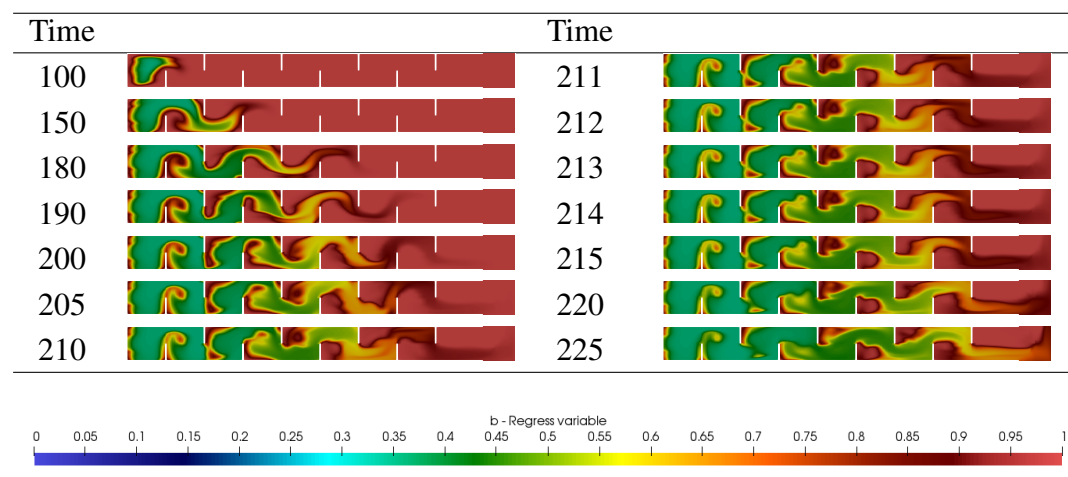
Figure 7.42: Flame propagation by regressive variable in section I of a mixture with Φ = 1.3

The flame propagation by regressive variable illustrated in Figure 7.38 and Figure 7.39 is similar to the flame propagation for $\Phi = 1.2$. The simulations show a methane-air reaction flame front with b around 0.7 for these simulations. The flame front propagation does not fill the region between the obstacles, especially after the third obstacle. The region behind the flame front continues a methane-air reaction as the decrease of the regressive variable. The regressive variable for $\Phi = 1.0$ has a value around 0.6 until 0.45, and for $\Phi = 1.1$ and 1.3 has a value around 0.6 until 0.35, respectively, until the fluid reaches the outlet wall.

The stoichiometric and rich mixtures by flow velocity and its vector estimation in section I are shown in Figure 7.43, Figure 7.44 and Figure 7.45.
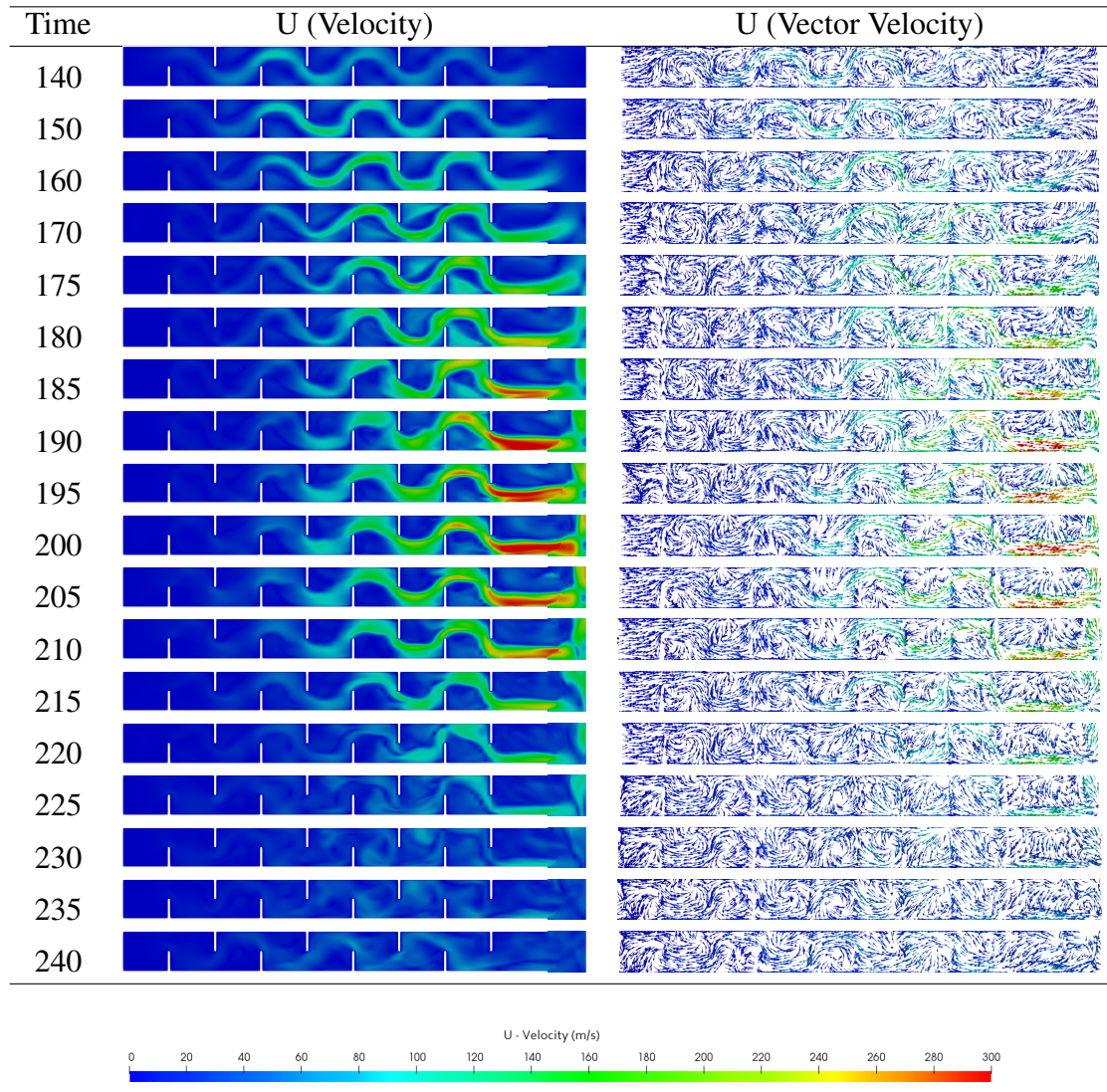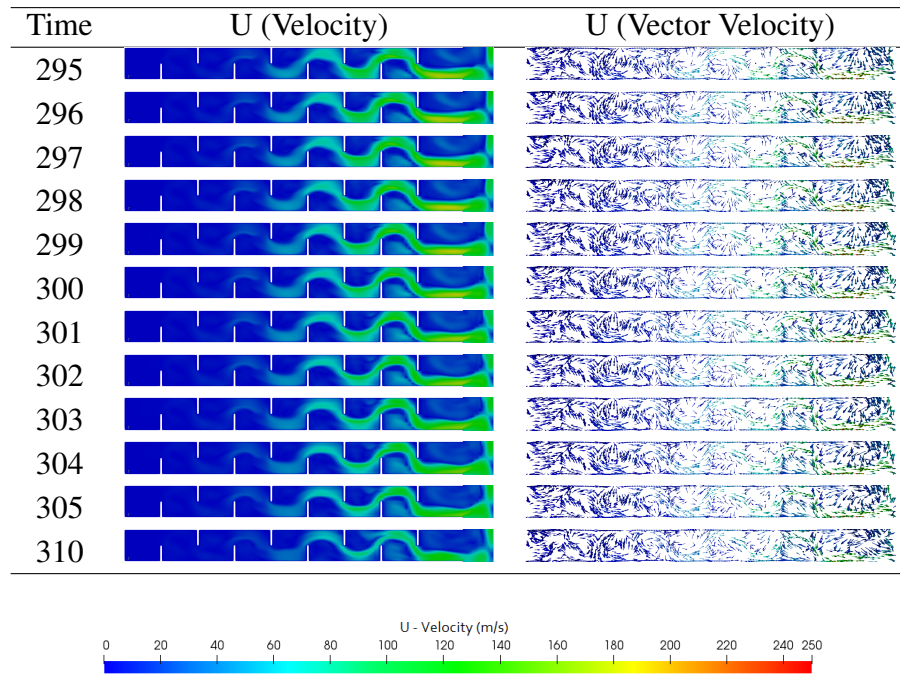

Figure 7.43: Flame propagation by flow velocity and vector flow velocity in section I of a mixture with $\Phi = 1.0$

Time	U (Velocity)	Time	U (Vector Velocity)
190		190	
195		195	
197		197	
199		199	
200		200	
205		205	
210		210	
211		211	
212		212	
213		213	
214		214	
215		215	
220		220	

U - Velocity (m/s)

0   50   100   150   200   250   300   350
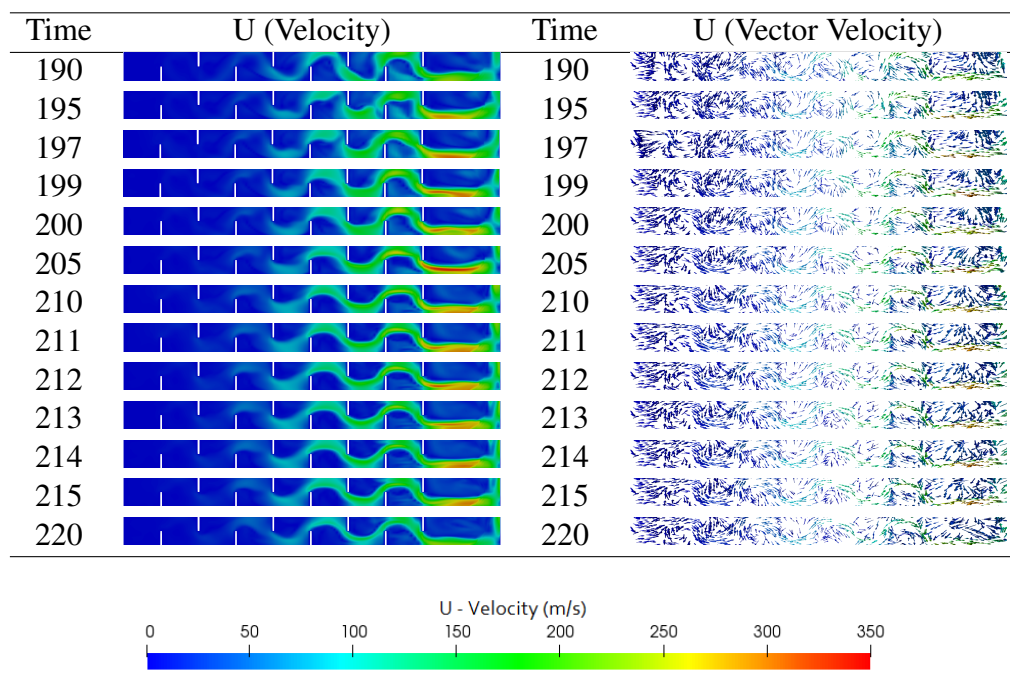
Figure 7.44: Flame propagation by flow velocity and vector flow velocity in section I with BC as wall of a mixture with $\Phi = 1.1$

Time	U (Velocity)	U (Vector Velocity)
190		
200		
205		
210		
215		
220		
221		
222		
223		
224		
225		

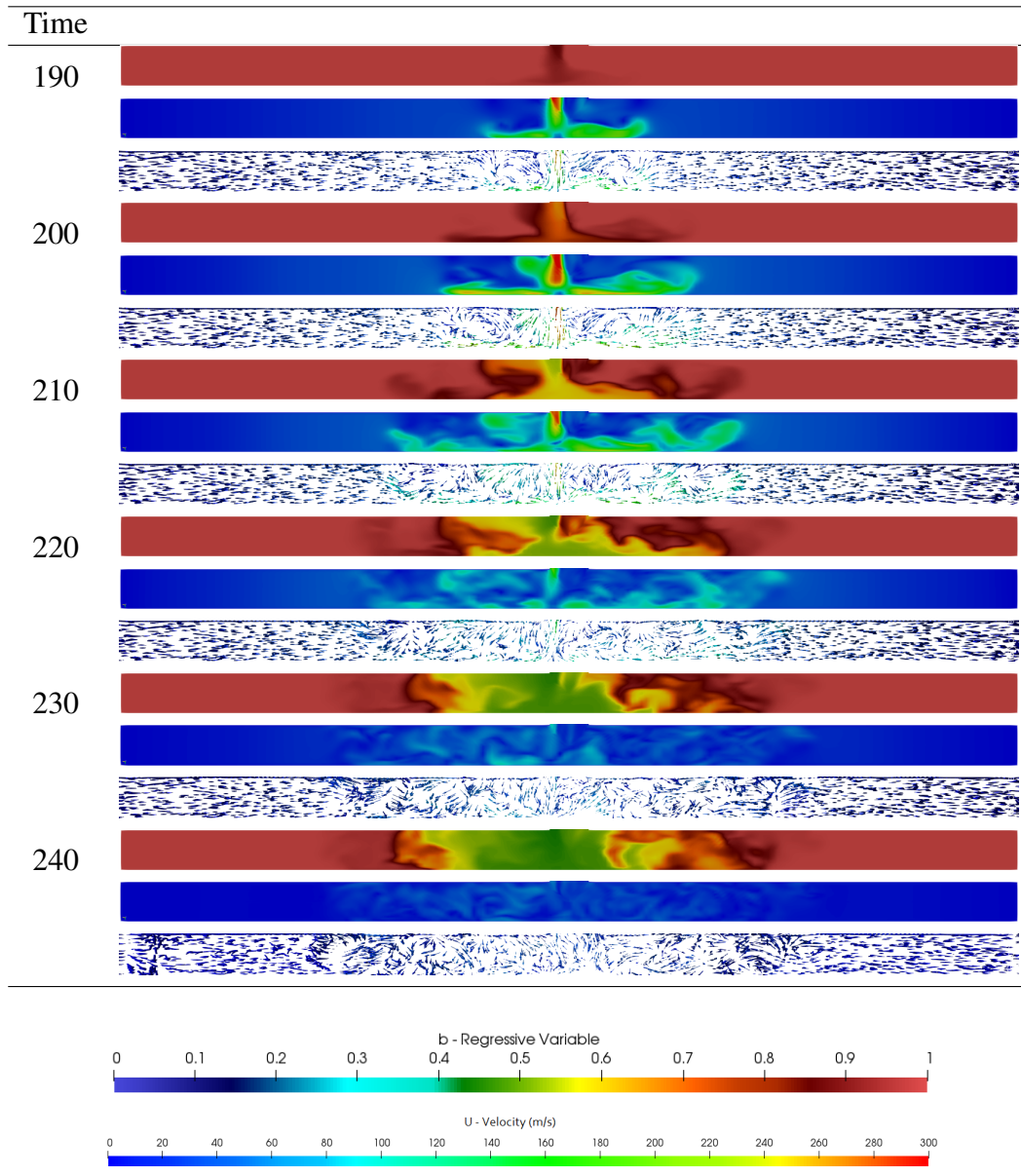U - Velocity (m/s)

0   50   100   150   200   250   300   350
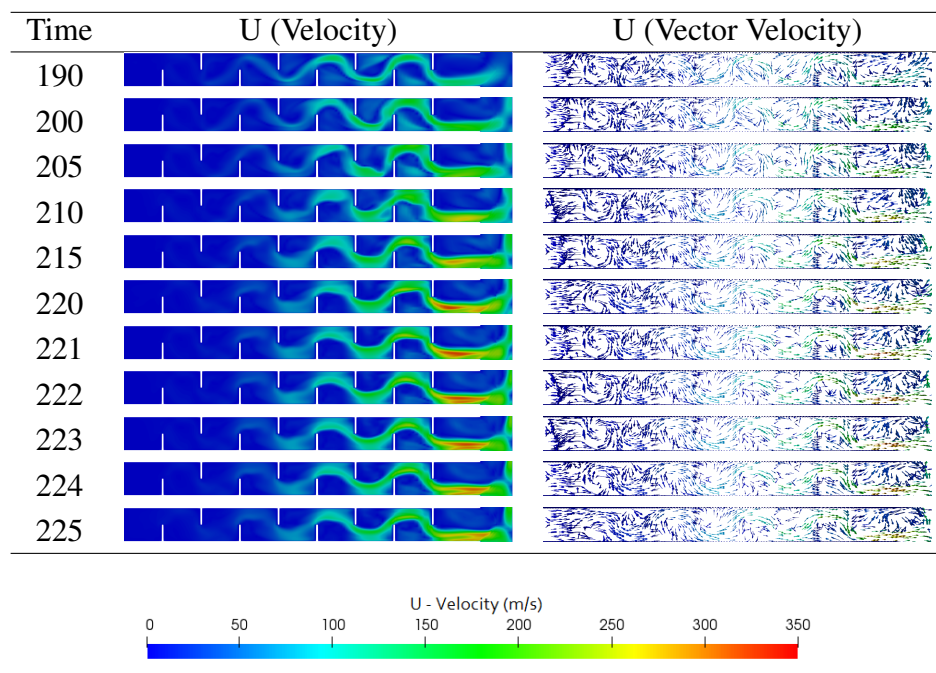
Figure 7.45: Flame propagation by flow velocity and vector flow velocity in section I with BC as wall of a mixture with $\Phi = 1.3$

The flame front by flow velocity of $\Phi = 1.0$, 1.1 and 1.3 increases when the flame is near to the end of section I. The simulation with $\Phi = 1.0$, 1.1 and 1.3 has a flame front by flow velocity around 190 m/s at frame time 295 s, 260 m/s at frame time 195 s and 250 m/s at frame time 220 s, respectively.

A vorticity formation on the last obstacles is observed for all four concentrations. The flow velocity on the vorticity formation with the flame is around 130 m/s until 150 for $\Phi = 1.0$ and 150 m/s until 200 for $\Phi = 1.1$ and 1.3.

The stoichiometric and rich mixtures by flow velocity and its vector estimation in section II and III are shown in Figure 7.46, Figure 7.47 and Figure 7.48.
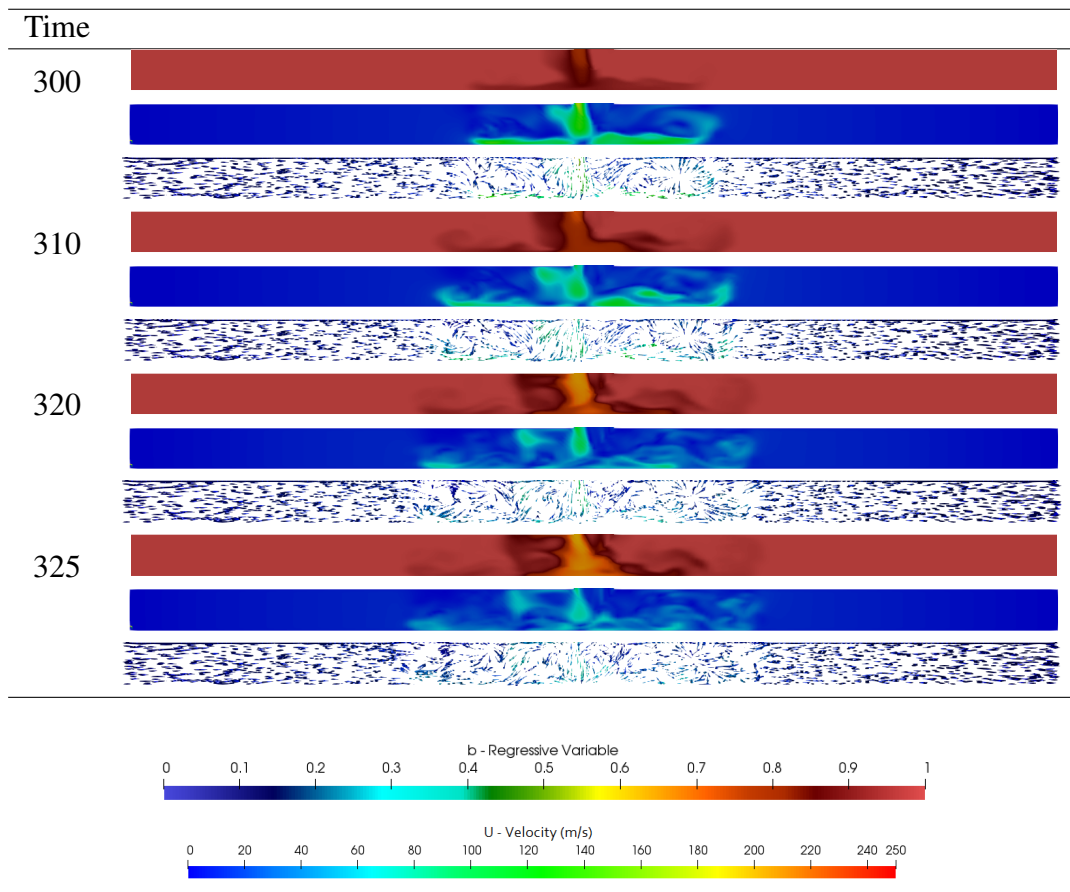
Figure 7.46: Flame propagation by regressive variable, flow velocity and vector flow velocity in section II and III of a mixture with $\Phi = 1.0$
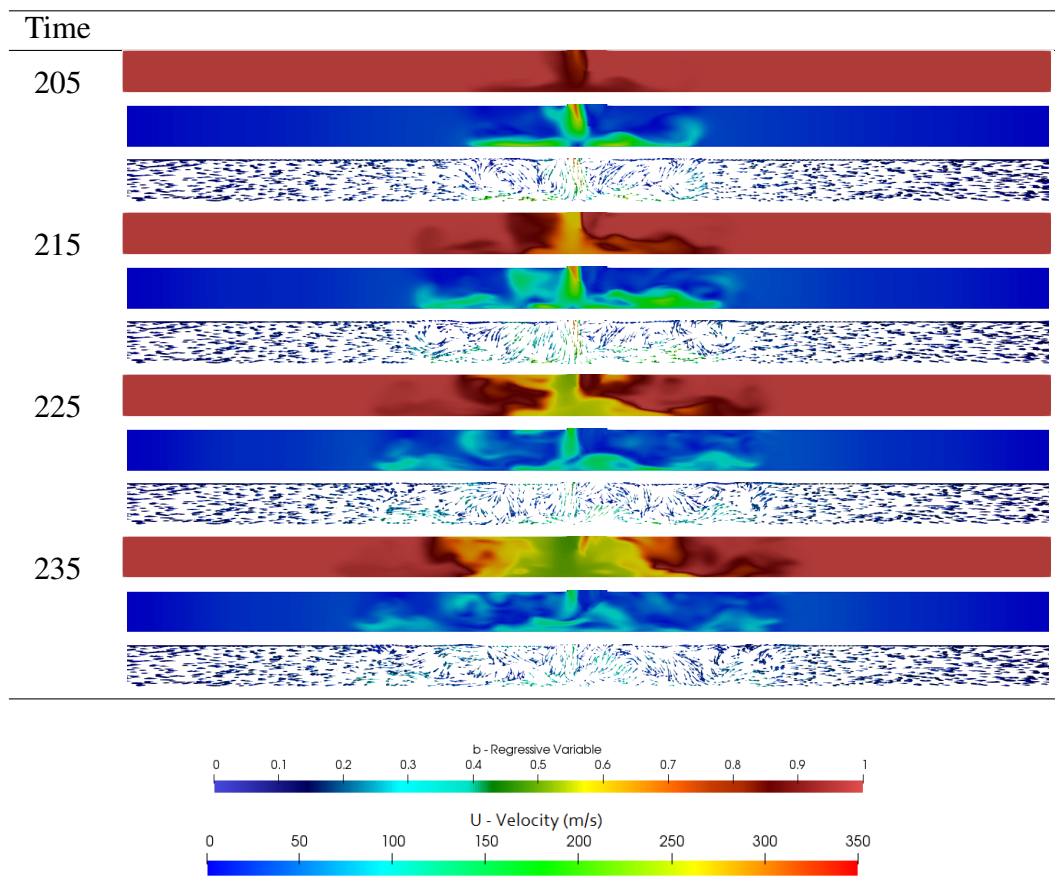
Figure 7.47: Flame propagation by regressive variable, flow velocity and vector flow velocity in section II and III of a mixture with Φ = 1.1
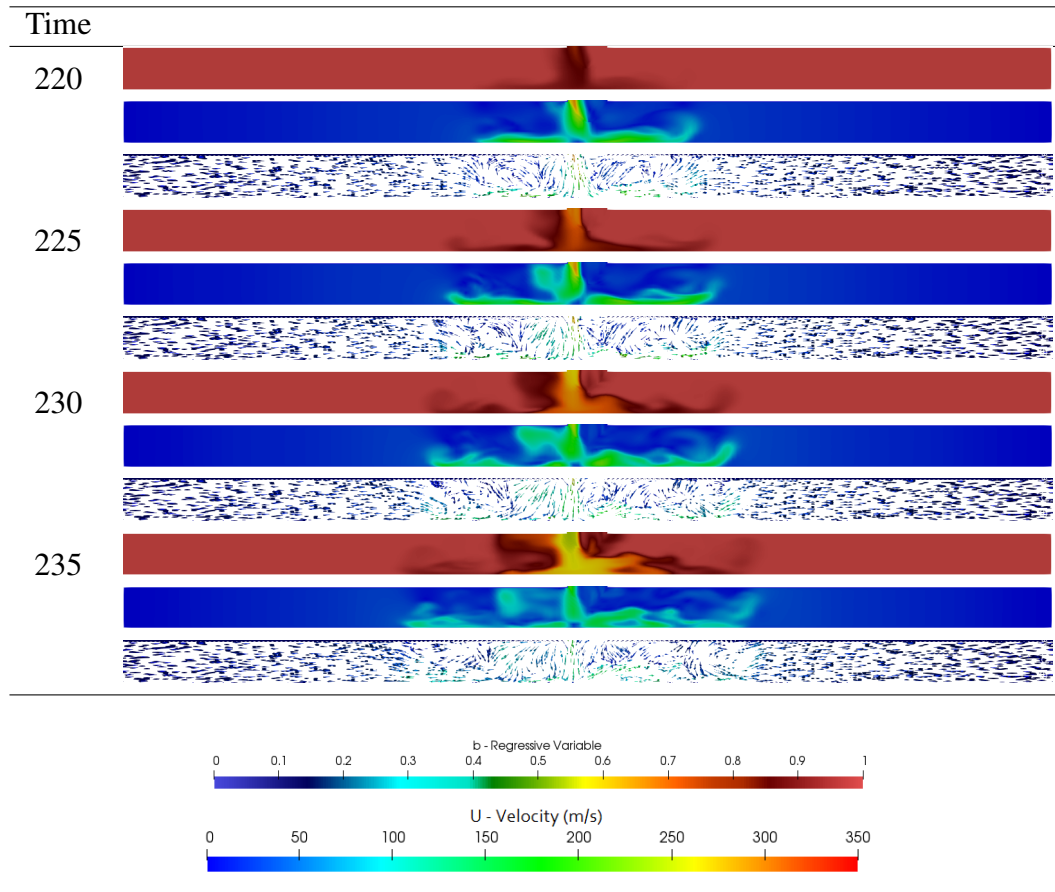
Figure 7.48: Flame propagation by regressive variable, flow velocity and vector flow velocity in section II and III of a mixture with $\Phi = 1.3$

The fluid inside of the domain reaches the outlet wall and the simulation stops before the flame propagates further. Thus the flame propagation velocity does not increase in section II and III. Different frame time sets are tested but the simulation stops due to the length of the pipe and the high flow velocity in the domain.

The flame propagation velocity of $\Phi = 1.0$, 1.1 and 1.3 has 160 m/s at 300 s, 250 m/s at 215 s and 200 m/s at 225 s, respectively. The bent region provokes a vorticity formation in section II and III.

The flame propagates with a higher intensity in direction of section II due to the last obstacle in section I. The simulation stops for $\Phi = 1.0$, 1.1, and 1.3 at frame time 325 s, 235 s, and 235 s, respectively.

7.2.1 Regressive Variable, Temperature, and Pressure

The fuel-oxidizer rate of methane-air reaction is defined by the regressive variable. The variation of this parameter by time is shown in Figure 7.49.
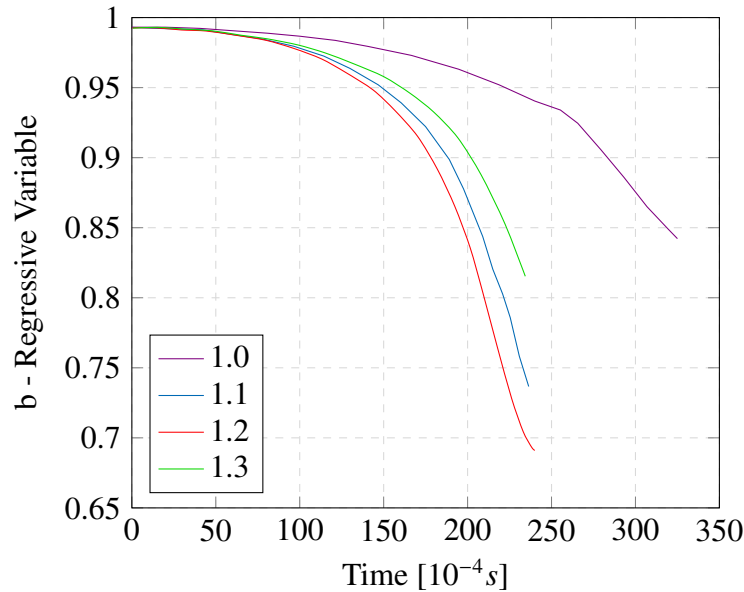
Figure 7.49: Regressive variable of premixed flame propagation of methane-air mixtures by time

The simulation stops and the regressive variable for $\Phi = 1.0$, 1.1, 1.2 and 1.3 is 0.84 at frame time 325 s, 0.73 at frame time 240 s, 0.69 at frame time 240 s and 0.81 at frame time 235 s, respectively. The plot in Figure 7.49 shows the methane-air does not react fully by the fuel-air ratio chosen. The CFD simulation of scale complex geometry as a T-pipe with obstacles shows a lower regressive variable depletion, especially if it is compared with the simulation of a T-pipe without obstacles, see Figure 7.28.

The pressure variation during the flame propagation by time is shown in Figure 7.50. The pressure of the experiments is compared with the pressure from the numerical simulation as illustrated in Figure 7.51.
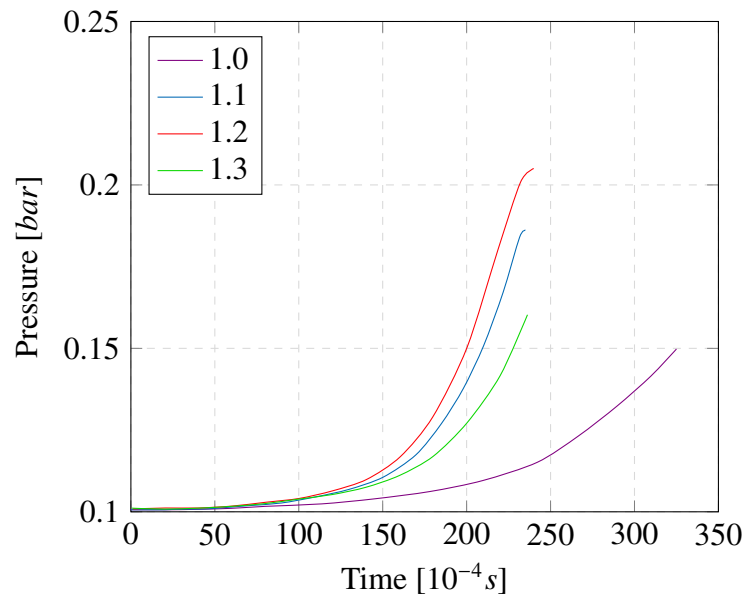
Figure 7.50: Pressure of premixed flame propagation of methane-air mixtures by time
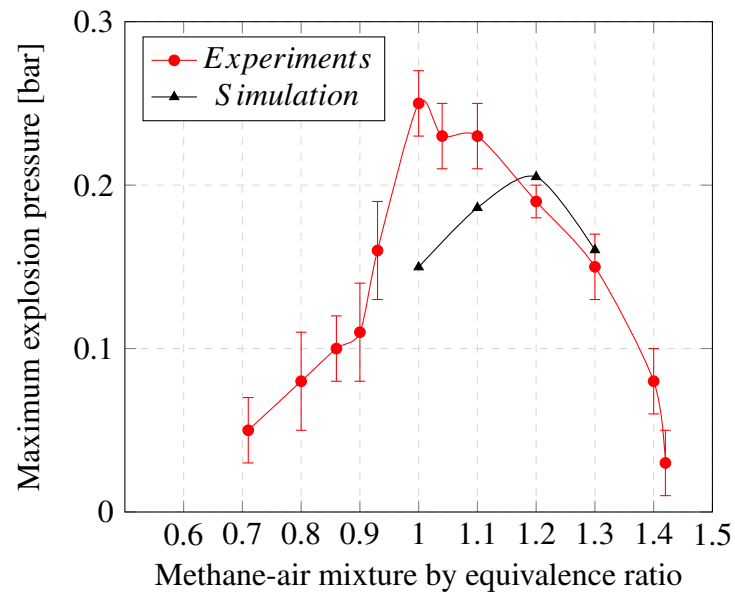
Figure 7.51: Experimental and numerical pressure of premixed flame propagation by methane-air concentrations

The pressure of the T-pipe with obstacles in Figure 7.50 shows a lower pressure in comparison to Figure 7.29. The numerical results of flame propagation at section I reproduce a similar pressure value as observed in the analysis of the experiments in Figure 7.51. The fluid inside of the T-pipe domain flows with a high velocity until the outlet wall and the simulation stops. A similar scenario in the experiment is observed as well as a lower pressure. The obstacles and the bent region provoke an increase of the flame speed and a decrease of the pressure. The adiabatic flame temperature is analyzed only in section I. The flame propagation by adiabatic flame temperature is shown in Figure 7.52 and Figure 7.53.
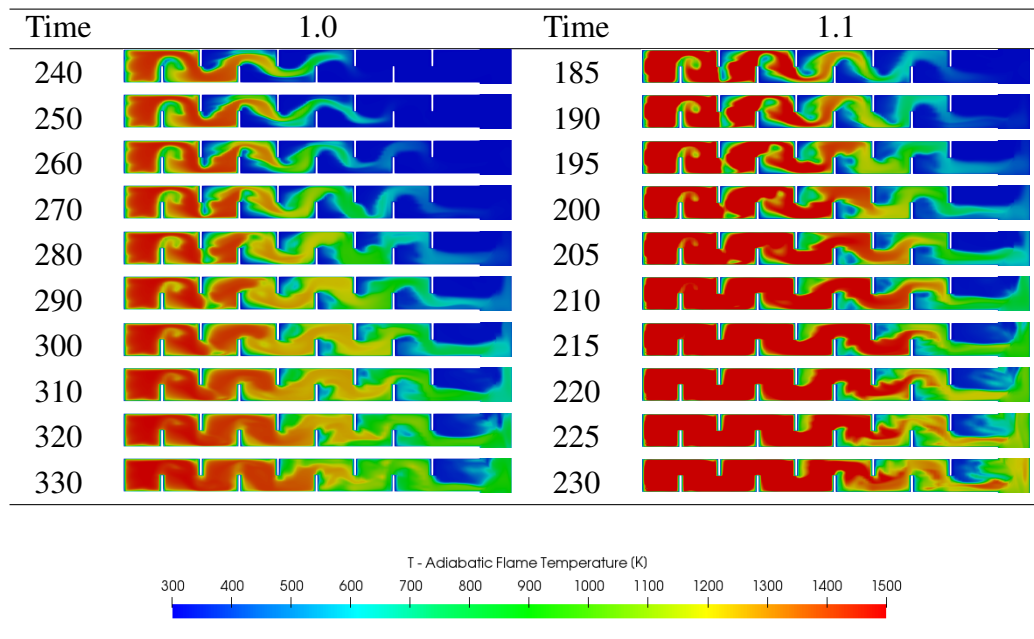
Figure 7.52: Flame propagation by adiabatic flame temperature in section I of mixtures with $\Phi = 1.0$ and 1.1
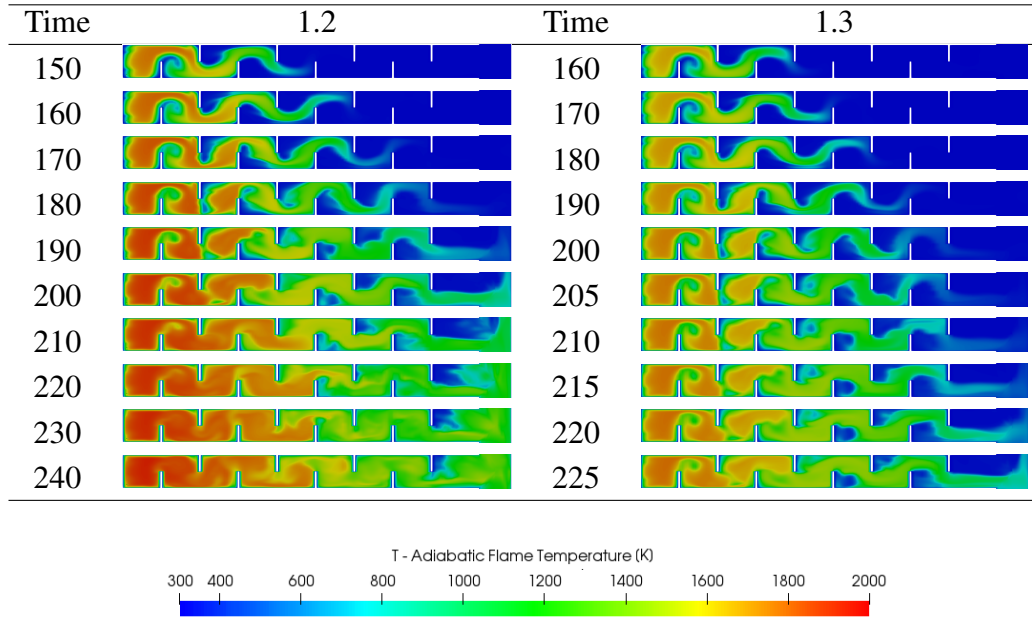
Figure 7.53: Flame propagation by adiabatic flame temperature in section I of mixtures with Φ = 1.2 and 1.3

The adiabatic flame temperature from a T-pipe obstacles is lower than T-pipe without obstacles. The methane-air concentrations Φ = 1.0, 1.1, 1.2 and 1.3 have a flame front with an adiabatic temperature around 1000 K, 1300 K, 1200 K and 1400 K, respectively. And the region behind the flame front has an adiabatic temperature around 1500 K until 1200 K, 1500 K until 1400 K, 1800 K until 1600 K and 1700 K until 1500 K, respectively. The region with the highest adiabatic flame temperature during the flame propagation is the same region with the lowest variable regressive.

8. Conclusion

This work aims to investigate the flame propagation of premixed methane-air in complex geometries. An explosion and flame propagation are performed in a pipe with bent parts with the purpose to resemble a complex geometry. This phenomenon is submitted to an experimental and numerical investigation to study the impact of the bent region on the flame fluid dynamics. A T-pipe is selected to represent a complex geometry with a bent region. A methane-air mixture is evaluated from the lean, stoichiometric, and rich concentration based on the flammability limit. The investigation is composed of the flame propagation in a T-pipe with and without obstacles, and a long straight pipe. A T-pipe with obstacles is constructed to study further impacts of the bent region in a flame propagation which already impinged by the addition of obstacles.

The premixed methane-air flame experiments show an elaborate scenario to execute the experiments, monitor flame propagation, and analyze the results. The experiment setup demands the construction of the apparatus to initiate, record high-speed images of explosion and flame propagation, and monitor the pressure. The implementation of programming logic control for the devices and the application of image processing techniques to evaluate the results is necessary. The numerical simulation also shows a complexity to set the CFD simulations, especially to set up the discretization methods, the boundary condition for the outlet walls, and turbulence models. Also important is the understanding of the numerical codes as the governing equations and the combustion models which can represent a realistic scenario equivalent to an explosion and flame propagation in small scale complex geometries of methane-air mixtures. To set up the experiments and numerical simulation, demands different technical procedures and a variety of tests are executed to achieve the results presented in this work. Additionally, attention to safety procedures is crucial because it is dealt with explosions and combustion.

The experiments request a gradation of a test to reach the quality of the flame propagation images feature. The first experiments are conducted using only premixed methane-air to provoke a flame propagation which is recorded by a high-speed camera. The images results of these experiment do not have an image resolution quality which allows analyzing the region

behind the flame front. TiO$_2$ powder is placed inside of the pipe. The addition of TiO$_2$ powder in the experiment expands the visualization of the flame propagation where other flame behaviors are possible to be observed. The images collected from the experiments using TiO$_2$ powder improve the image resolution of the flame propagation images, especially the region behind the flame front.

The setup and solving of the numerical simulations request numerous tests to understand and modify the code especially of the governing equations and combustion models, to generate the mesh and to implement the discretization methods. The methane-air mixture in the CFD simulations is tested as homogeneous and inhomogeneous mixtures. The purpose is to evaluate the impact of the fuel mixture fraction which defines the methane-air mixture as inhomogeneous in flame propagation. Similarly, the differences between homogeneous and inhomogeneous mixtures in complex geometries are evaluated. Both geometries show a difference in inhomogeneous and homogeneous methane-air mixtures, especially characterized by the regressive variable and turbulent flame speed parameters.

The outlet PET foils provoke a surplus scenario because it is between an open and closed-end outlet system. This scenario demands two different settles of numerical simulation which are separated by the boundary conditions as wall and piston.

The comparison of the experimental results with the numerical simulation of this phenomenon has the purpose to conjure the phenomenon of the laboratory to other scenarios, understand better the phenomenon and the applicability of the simulation on reality.

8.1   T-pipe without Obstacles

The analysis of flame propagation in a T-pipe without obstacles extends the knowledge of the reactive fluid dynamic of a flame in complex scenarios. The image results monitored by the high-speed camera with the addition of TiO$_2$ powder allow observing the fluid dynamic of the region behind the flame front and the impact of this region on the flame front. The numerical simulation enhances the understanding of the phenomenon studied in the laboratory.

The pressure provoked by the explosion and flame propagation has an increase and decreases during the variation of lean, stoichiometric, and rich methane-air concentrations. The pressure collected from the experiments and the numerical results coincide with pressures collected in experiments using a PET foil as outlet foil and between the pressure scale of the experiment which has an open and a closed system. The pressure scale from the numerical results shows also a similar behavior during the variation of the methane-air concentration and pressure scale.

The information obtained from the experimental and numerical results shows the fluid dynamic of the flame front and region behind the flame front. They indicate different stages of the flame during the propagation. The analysis of flame in section I provides a new perspective of flame propagation in a straight and small scale cylinder pipe with an outlet PET foil. This works aims to propose a modification of the "Tulip Flame" described in Clanet's and Searby's work [12]. The model is applied for inhomogeneous premixed methane-air flame propagation on atmospheric pressure. The flame propagation has a total of seven stages. The first stage is defined as hemispherical expansion. The second stage refers similarly to

the hemispherical finger-shaped flame and it occurs a reverse propagation behind the flame front. The third stage is the elongation of the finger-shaped where the flame front has a flame stretch on the sides. In the fourth stage, which is called "Tulip Flame", the flame front elongates and the reverse propagation behind the flame front continues to propagate backwards. The fifth stage initiates another elongation of the flame front by side. The sixth stage is where the elongation of the flame is beginning to close and it occurs a second reverse propagation behind the flame front. The seventh stage is when the flame front is closed and the second reverse propagation propagates backwards and approaches the first reverse propagation. The proposed stages settle in more details the fluid dynamic of the flame propagation and enhance the description of the region behind the flame front which is barely visualized through images without the addition of TiO_2 powder.

The propagation at the bent region forwarding section II and III acknowledge a fluid dynamic with a reverse propagation behind the flame front and a flame front propagation which tends to propagate near the wall. The flame conduces to propagate equally to both sections. The flame front speeds increase in section II and III in comparison to the flame speed in section I. The center of section II and III show a separated region where the flame does not propagates. The numerical simulations of the T-pipe without obstacles obtain a fluid dynamic similar to the flame propagation observed in the experiments. The combustion model does not converge for all methane-air concentrations evaluated in the experiments. But the concentrations which converged are the same possible to observe in the experimental flame propagation, and it exposes a similar scenario as the experiments.

The result analysis of the simulations with boundary conditions as piston and wall displays a distinction of the flame fluid dynamic of these two scenarios. The simulation results comparison of these boundary conditions uses the parameters regressive variable and the turbulent flame speed. The outlet wall defined as wall exhibits a flame propagation similar as observed in the experiment. The flame speed characterized by the turbulent flame speed and its vector definition of the turbulent flame speed show a flame speed equivalence to the experimental results. The region behind the flame front displays the proposed stages. The regressive variable exposes a flame front format also similar to the experimental results. The outlet defined as piston exhibits by the turbulent flame speed a lower flame speed in comparison to the experimental result. The flame front format does not show similar behavior as the experimental results. But the region behind the flame front resembles better the model proposed with seven stages for inhomogeneous premixed flame propagation. So further CFD simulation results are only used from the outlet wall using the boundary condition as wall.

The simulation of homogeneous mixtures in comparison to the simulation of inhomogeneous mixtures indicates a difference in the flame front propagation by the regressive variable parameters analysis, especially the simulation with an outlet as a piston. The flame propagation, characterized by the turbulent flame speed, displays a similar flame speed and a reverse propagation behind the flame front.

The numerical results of the lean, stoichiometric, and rich concentrations derive from the simulations with inhomogeneous mixtures and boundary conditions of the outlet as wall. The parameters analyses of the converged numerical simulations expose a flame fluid dynamic similar to the images collected by the high-speed camera. The flame propagation is investigated by the parameters regressive variable, temperature, and turbulent flame speed.

These parameters show flame propagation in section I with the seven stages proposed. The increase of the flame speed when the flame reaches and crosses the bent region is observed by the turbulent flame speed. The reverse propagations behind the flame front is noticed using the vector characterization of the turbulent flame speed. The format of the flame is shown using the regressive variable parameters which shows the flame front format as the hemispherical, the hemispherical finger-shape, and the closure of the finger-shape. The flame format in section II and III featured by the regressive variable shows a flame front similar to the experimental results. The flame tends to propagate near the wall and there is a separated region in the center of section II and III where the flame does no propagate. The flame has an equivalence flame speed for both sides as indicated in the turbulent flame speed. Additionally, it exposes a vorticity formation and a reverse propagation behind the flame front as displayed by the vector characterization of the turbulent flame speed.

The straight pipe experiments show a relative increase of the flame speed during the propagation and more important the region behind this flame propagation and the join of the second reverse propagation from the seventh stage of the proposed model. The increase of the pressure is also relative due to the impact of the pipe prolonging.

8.2 T-pipe with Obstacles

The flame propagation in the T-pipe with obstacles enhances the comprehension of different complex flame fluid dynamic scenarios. The pressure results acquired by the piezoelectric pressure sensor show an unexpected pressure provoked by the explosion and flame propagation. The image results monitored with the high-speed camera of the T-pipe endure the comprehension of the region behind the flame front and flame front propagation. The flame propagation form of the experiment assimilates to the simulation results.

The maximum explosion pressure collected from the experiments is significantly lower than the explosion obtained in a T-pipe without obstacles and a straight pipe. This decrease of the pressure does not corespondent to the results observed in the references cited in this work. Notwithstanding, the pressure variation during the increase of methane-air concentration corresponds to previous works where the pressure increases from the lean concentration until the stoichiometric methane-air concentration and afterwards decreases into a rich concentration. The pressure result of the numerical simulation also shows a lower pressure concerning the numerical results of the T-pipe without obstacles. And it exposes a similar pressure scale in comparison to the T-pipe with obstacles experimental results.

The addition of TiO_2 powder inside of the apparatus enhances the flame propagation visualization of the flame front and region behind the flame front. The flame propagation of the experiments and numerical simulation show a vorticity formation between the obstacles, particularly on the last obstacles near the bent region. The vorticity speed from the experimental results is not possible to be estimated due to the quality resolution of the images. But the fluid dynamics are equivalent to the results exposed by the fluid velocity by the vector. The flame front does not fill initially the region between the obstacles in the experimental and numerical results. Notwithstanding, this region is filled when the flame reaches section II and III in both analyses.

The flame front speed estimated at the end of section I and during the propagation at the bent region forwarding the outlet PET foils shows a high speed in the experiments. The addition of the obstacles is the main reason for this speed increase in section I. The flame speed has a considerable growth in comparison to the T-pipe without obstacles, especially when the flame reaches the end of section I. The fluid velocity of the flame propagation observed in the CFD simulation shows also a high flame speed in section I.

The flame propagation at the bent region tends to propagate with a higher intensity and speed into section II due to the last obstacles which are placed on the right side of section I. A reverse propagation behind the flame front is observed in the bent region of the experimental and numerical results. The flame speed already increased due to the obstacles in section I. In section II and III the flame speed and vorticity formation increase as a result of the bent region. The impact in the flame speed and vorticity formation provoked by the bent region on the T-pipe with obstacles is higher than the increase provoked by the bent region in the T-pipe without obstacles. But in the numerical results when the flame crosses the bent region, the velocity does not increase at the same scale as observed in the experiments. Because the CFD simulations stop before the flame front crosses a certain length in section II and III. Furthermore, the fluid reaches the outlet wall too soon. This scenario limits a numerical analysis of the flame propagation in these section.

The inhomogeneous and homogeneous T-pipe with obstacles simulation shows a difference in the methane-air reaction by the regressive variable analysis in the simulation with the outlet using the boundary condition as a piston. The flame speed of homogeneous mixtures shows a lower fluid velocity in comparison to inhomogeneous mixtures.

The boundary conditions as piston and wall tested in theses simulations do not have an expressive difference. The flame velocity is too high and the simulation stops before the flame propagates and increases the speed in section II and III .

The simulation with methane-air concentration which does not converge can be motivated due to the set up of the simulation, especially the outlet wall boundary conditions, methane-air mixture distribution on the grid, or a limitation of the combustion model. These limitations also appear in simulations with a homogeneous methane-air mixture, other turbulent and discretization models, refiner meshes, and simulations using boundary conditions as piston for the outlet walls. The experimental and numerical analyses of an explosion and flame propagation of inhomogeneous mixture in a T-pipe with obstacles resemble a complex geometry providing a better understanding of the impact of a bent region after the flame propagation is submitted into a stress scenario.

8.3   Future Work

This work attempts to improve the understanding of flame propagation in complex scenarios. This study shows how a bent region impacts the flame propagation with the increase of the flame speed in geometries such as a T-pipe with and without obstacles. And it displays a decrease of pressure when obstacles, such as a T-pipe are added into the complex scenario. A further perspective of flame propagation in the straight track of the T-pipe without obstacles is observed in the region behind the flame front. The experimental and numerical result analyses prompt to propose seven stages of the flame during the propagation.

The numerical simulations using the wrinkle combustion model *XiFoam* does not converge for all methane-air concentrations simulated. Thus a full comparison of premixed flame propagation from the experiments with the simulation results is not possible. The limitation remains in the numerical simulations for different equivalence ratios with the same mesh, mathematical models, and discretization methods.

Due to the observed limitations in near-wall boundary conditions in OpenFOAM for premixed flame simulations, the development of new techniques is a surplus. Besides, the boundary conditions representing the outlet wall shall be improved for a more realistic result. It is also suggested to simulate other types of complex geometries where the flame propagates longer after the bent region and with more bent regions. Moreover, other mathematical models and discretization methods shall be simulated. Especially focusing on the methane-air concentrations which do not show a flame propagation or just partly. Interesting can also be the implementation of new discretization methods of the governing equations based on advanced PDF models.

For further development of this work's experimental results the following steps are suggested: Experiments shall be performed by using the PIV technique with 2D and 3D high-speed images to improve the visualization of the flame propagation and to estimate a vector velocity.

Bibliography

[1] Peters N. (2010) Combustion Theory. RWTH Aachen University. (cited on Page xiii, 10, 11, 17, and 20)

[2] Poinsot T. and Veynante D. (2012) Theoretical and Numerical Combustion. 3th ed., Edwards. (cited on Page xiii, 10, 11, 12, 13, 15, 17, 19, 20, 21, 22, 23, 24, 26, 27, 31, 40, and 42)

[3] Pope S. B. (2012) Turbulent Flows. 1th ed., Cambrigde University Press. (cited on Page xiii, 15, 17, 19, 20, 21, 22, 23, 24, 26, and 31)

[4] Liu F. (2016) A Thorough Description Of How Wall Functions Are Implemented In OpenFOAM. Chalmers University of Technology. (cited on Page xiii, 24, 25, 41, and 84)

[5] Weller H. G. (1993) The Development of a New Flame Area Combustion Model Using Conditional Averaging. Ph.D. Thesis, Imperial College of Science Technology and Medicine. (cited on Page xiii, 27, and 38)

[6] Greenshields C. J. (2018) OpenFOAM. The OpenFOAM Foundation. (cited on Page xiii, xix, 12, 13, 14, 25, 32, 33, 34, 35, 36, 37, 38, 39, and 41)

[7] Holzinger G. (2015) OpenFOAM - A little User-Manual. CD-Laboratory - Particulate Flow Modelling Johannes Kepler University, Linz, Austria. (cited on Page xiii, xix, 10, 11, 25, 30, 32, 33, 34, 35, 36, 37, 38, 41, and 84)

[8] Cowards H.F. and Jones G.W. (1952) Limits of Flammability of Gases and Vapors. (cited on Page xix, 10, 12, and 43)

[9] Gülder Ö. L. Correlations of Laminar Combustion Data for Alternative S.I Enfine Fuels. SAE Technical Paper 841000, 198. (cited on Page xix, 16, and 38)

[10] J. Hopken T., Maric and Mooney K. (2014) The OpenFoam Technology Primer. 1th ed., Sourceflux. (cited on Page xix, 10, 32, 33, 34, 35, 36, 37, 38, 39, and 41)

[11] J. R. Bakke D., Bjerketvedt and Wingerden K. V. (1992) Gas Explosion Handbook. GexCon. (cited on Page 7)

[12] Clanet C. and Searby G. On the "Tulip Flame" Phenomenon. Combustion and Flame, 2180: 225-238. (cited on Page 8, 54, 59, 62, 64, 65, and 140)

[13] Xiao H.   (2016) Experimental and Numerical Study of Dynamics of Premixed Hydrogen-Air Flames Propagating in Ducts. PhD Thesis, University of Science and Technology of China.   (cited on Page 8)

[14] Yasari E. (2013) Extension of OpenFOAM Library for RANS Simulation of Premixed Turbulent Combustion. Master Thesis, Chalmers University of Technology.   (cited on Page 8, 11, 31, and 39)

[15] Sempionato G. H.   (2015) Estudo de Chama Pré-Misturada Estratifica Usando Modelo de Enrugamento de Superficie de Chama com Limite de Extincao. Ph.D. Thesis, Instituto Nacional de Pesquisas Espaciais.   (cited on Page 8 and 39)

[16] Williams F. A. (1985) Combustion Theory. 2th ed.,The Benjamin/Cummings Publishing Company, Inc.   (cited on Page 10, 11, 12, 13, 15, 20, 22, 23, 24, 25, and 85)

[17] Fox R. O. (2003) Computational Models for Turbulent Reacting Flows. 1th ed., Cambrigde University Press.   (cited on Page 10 and 31)

[18] Warnatz J., Maas U., and Dibble R.W.   (2006) Combustion Physical and Chemical Fundamentals, Modeling and Simulation, Experiments, Pollutant Formation. 4th ed., Springer.   (cited on Page 11 and 12)

[19] Zeldovich Y. B. and Frank−Kamenetsky D. A. (1938) Zh. fiz. Khim., Mosk., 12 (1938), p. 100. 6. N.N.   (cited on Page 11)

[20] S. Gordon B. J., McBride and Reno M. A.   (1993) Coefficients for Calculating Thermodynamic and Transport Properties of Individual Species. National Aeronautics and Space Administration.   (cited on Page 12)

[21] Stull D. R. and H. Propher. (1971) Janaf Thermochemical Tables. Unites States Deparment of Commerce.   (cited on Page 12)

[22] W. E. Stewart R. B., Bird and Lightfoot E. N.   (2002) Transport-Phenomena. 2th ed., John Wiley & Sons, Inc.   (cited on Page 13, 14, 28, 29, and 30)

[23] Felden A. (2015) Cantera Tutorials - Introduction Cantera.   (cited on Page 13, 15, and 17)

[24] J. L. Ziegler S. P. M., Bane and Shepherd J. E. (2010) Development of One-Step Chemistry Models for Flame and Ignition Simulation. Graduate Aerospace Laboratories California Institute of Technology.   (cited on Page 14 and 26)

[25] Peters N.   (1992) Fifteen Lectures on Laminar and Turbulent Combustion N . Peters Ercoftac Summer School Aachen, RWTH Aachen.   (cited on Page 15)

[26] Clarke A. and Hargrave G. K.   (2009) Measurements of laminar premixed methane – air flame thickness at ambient conditions. Mechanical Engineering Science, 223: 1969-1973.   (cited on Page 17 and 18)

[27] Bradley D. and Andrews G. E. (1972) Determination of Burning Velocities: A Critical Review. Combustion and Flame, 18: 133-153.   (cited on Page)

[28] Yamaoka I. and Tsuji H. (1984) Determination of burring velocity using counterflow flames. The Combustion Institute, pp 1883–1892.   (cited on Page 17 and 18)

[29] Luca C. (2015) CFD Modeling of Turbulent Premixed Combustion in Spark-Ignition Engineer. PhD Thesis, Politecnico di Milano Departmen.   (cited on Page 17)

[30] Gaathaug A. V. (2008) Flame propagation in a transparent pipe with a single obstruction. Telemark University College.   (cited on Page 18)

[31] C. O. Paschereit J. A., Gray and Moeck J. P. (2015) An Experimental Study of Different Obstacle Types for Flame Acceleration and DDT. Springer, Active Flow and Combustion Control 2014, pp 265-279.   (cited on Page 18)

[32] Darrieus G. (1944) Propagation d'un Front de Flamme: Assai de Theorie des Vitesses Anomales de Deflagration par developpement Spontane de la Turbulence. Combustion and Flame, 73: 77-85.   (cited on Page 18)

[33] Landau L.D. (1946) On the Theory of Slow Combustion.International conference of applied mechanics, 6th, Paris.   (cited on Page 18)

[34] F. Moukalled and Mangani L. (2016) The Finite Volume Method in Computational Fluid Dynamics - An Advanced Introduction with OpenFOAM® and Matlab®. 1th ed., Springer.   (cited on Page 19, 20, 28, 29, 30, 31, 32, 36, 37, and 84)

[35] Patankar S. V. (1980) Numerical Heat Transfer And Fluid Flow. 1th ed, Taylor & Francis.   (cited on Page 19, 20, and 28)

[36] Schlichting H. (1979) Bounday Layer Theory. 7th ed, Springer.   (cited on Page 19 and 24)

[37] Hinze J. O. (1975) Turbulence. 2th ed, McGRAW-HILL.   (cited on Page 19)

[38] Zimont V. L. (1979) Theory of turbulent combustion of a homogeneous fuel mixture at high Reynolds numbers. Springer, 15: 305–311. *Plenum Publishing Corporation.* (cited on Page 20)

[39] K.G. Vollmer F., Ettner and Sattelmayer T. (2014) Numerical Simulation of the Deflagration-to-Detonation Transition in Inhomogeneous Mixtures. Hindawi, Journal of Combustion, Vol. 2014, Article ID 686347.   (cited on Page 20)

[40] Bonart H. (2012) Implementation and Validation of a Solver for Direct Numerical Simulations of Turbulent Reacting Flows in OpenFOAM . Bachelor Thesis, Karlsruhe Institute of Technology.   (cited on Page 20)

[41] Davidson L. (2016) Fluid mechanics , turbulent flow and turbulence modeling. Chalmers University of Technology.   (cited on Page 20, 40, and 41)

[42] Shchetinkov E. S. (1965) The physics of the combustion of gases. 2th ed., Clearing-house for Federal Scientific and Technical Information.   (cited on Page 20 and 21)

[43] Peters N. (1997) Turbulent Combustion. RWTH Aachen.   (cited on Page 21, 22, 23, and 26)

[44] Spalding D. B. (1976) Development of the Eddy-Break-Up model of turbulent combustion. 16th Symposium International on Combustion, The Combustion Institute, pp 1657-1663.   (cited on Page 26)

[45] Kristoffersen K. (2004) Gas explosions in process pipes. PhD. Thesis, Telemark University College.   (cited on Page 26)

[46] Holzmann T. (2106) Mathematics, numerics, derivations and openfoam. The Basics for Numerical Simulations.   (cited on Page 28, 29, 30, 31, 36, and 84)

[47] Wilcox D. C. (1994) Turbulence modeling for CFD. DCW Industries.   (cited on Page 28 and 31)

[48] Laney C. B. (1998) Computational Gasdynamics. 1th ed, Cambrigde University Press.   (cited on Page 29)

[49] Jasak H. (1996) Error Analysis and Estimation for the Finite Volume Method with Applications to Fluid Flows. PhD Thesis, University of London.   (cited on Page 29 and 32)

[50] Ferziger J.H. and Peric M. (2002) Computarional Methods for Fluid Dynamics. 3th ed., Springer.   (cited on Page 29, 30, 36, and 37)

[51] Saad Y. (2003) Iterative Methods for Sparse Linear Systems Second Edition Yousef Saad. 2th ed, Society for Industrial and Applied Mathematics.   (cited on Page 37)

[52] Behrens T. (2009) OpenFOAM's basic solvers for linear systems of equations - Solvers, preconditioners, smoothers. Technical University of Denmark.   (cited on Page 37)

[53] Pope S. B. (1991) The PDF Method for Turbulent Combustion. Cornell University.   (cited on Page 39)

[54] The Open Source Code Team. (2017) OpenFOAM - The Open Source CFD Toolbox.   (cited on Page 39)

[55] Villiers E. (2006) The Potential of Large Eddy Simulation for the Modeling of Wall Bounded Flows Eugene de Villiers. PhD Thesis, University of London.   (cited on Page 41)

[56] T. Iliescu L. C., Berselli and William J. (2005) Mathematics of Large Eddy Simulation of Turbulent Flows. 1th ed, Springer.   (cited on Page 41)

[57] C. Willert S. Wereley M., Raffel and Kompenhans J. (2007) Particle Image Velocimetry A Practical Guide. 2th ed., Springer. (cited on Page 43, 45, and 47)

[58] Photron. Fastcam Mini UX 100 - Hardware Manual. Revision 1.01 EN, Photron. (cited on Page 45)

[59] Titanium Dioxide. MSDS. Nr. 1907 2006 (REACH). Available from www.carlroth.com (acessed: 2016). (cited on Page 47)

[60] Pinto J. C. and Schwaab M. (2007) Análise de Dados Experimentais I. Fundamentos de Estatística e Estimação de Parâmetros. 1th ed, E-papers. (cited on Page 47)

[61] Ferreira T. and Rasband W. ImageJ User Guide. 2012. (cited on Page 48 and 65)

[62] S. Liu C. Shu Y. Ding Q., Wang and Liu Z. (2017) Influence of Different Types of Obstacles on the Propagation of Premixed Methane-Air Flames in a Half-Open Tube. Energy, 10(11):1908. (cited on Page 8, 49, 77, and 78)

[63] Mittal M. (2017) Explosion pressure measurement of methane-air mixtures in different sizes of confinement. Journal of Loss Prevention in the Process Industries, 46: 200-208. (cited on Page 49 and 64)

[64] J. Zanganeh B. Moghtaderi S., Kundu. (2016) A review on understanding explosions from methane-air mixture. Journal of Loss Prevention in the Process Industries, 40: 507-523. (cited on Page 49 and 64)

[65] L. Bai-quan Z. Chuan-jie J. Bing-you S. Yu-min G., Chang and Hao Y. (2016) Effect of filling ratio on premixed methane/air explosion in an open-end pipe. International Journal of Spray and Combustion Dynamics, 8(2) 112–118. (cited on Page 49)

[66] Y. Zhang X., Chen and Zhang Y. (2012) Effect of CH4–Air Ratios on Gas Explosion Flame Microstructure and Propagation Behaviors. Energies, 5: 4132-4146. (cited on Page 50)

[67] M. Gieras and R. Klemens. (2009) Experimental studies of explosion of methane-air mixtures in a constant volume chamber.Combust. Sci. and Tech, 181: 641-653. . (cited on Page 50)

[68] R. M. Kasmani S. Z., Sulaimana and Mustafaa A. (2016) Experimental Study on Flame Propagation in a Straight Pipe. Jurnal Teknologi, 78: 8-3. (cited on Page 50)

[69] B. Lin Y., Hong and Zhu C. (2016) Premixed methane/air gas deflagration simulations in closed-end and open-end tubes. International journal of spray and combustion dynamics, 8(4). (cited on Page 50)

[70] Z. Jafar J. A., Mohammed and Behdad M. (2017) Deflagration of premixed methane–air in a largescale detonation tube. Process Safety and Environmental Protection, 109: 374-386. (cited on Page 50 and 68)

[71] Chapman W.R. and Wheeler R.V. (1926) The propagation of flame in mixtures of methane and airPart IVThe effect of restrictions in the path of the flame.Journal of the Chemical Society, pp 2139-2147. (cited on Page 77)

[72] R. Knystautas J. H., Lee and Chan C. K. (1984) Turbulent flame propagation in obstacles-filled tubes. Twentieth Symposium (International) on Combustion - The Combustion Institute, pp 1663-1672. (cited on Page 77)

[73] Puigt G. and Deniau H. (2011) CFD e-Learning Mesh and Discretization., Centre Européen de Recherche et de Formation Avancée en Calcul Scientifique, M: 1-45. (cited on Page 81)

[74] Z. U. A. Warsi J. F., Thompson and Mastin C. W. (1985) Numerical grid generation. 1th ed, North-Holland. (cited on Page 81)

Address: Albert Vater Strasse 87, 39108 Magdeburg Germany – Tel: +49 0176 43306110

Email: vitorgabriel.eng@hotmail.com

Ambiente Seguro Engineering

Ambiente Seguro is a company create by four students after the master in HSE engineering. The company consisted of two chemical engineers and two environmental and agronomist engineers, all the members were HSE engineers too. The company acts application and consultancy of process safety, risk analyses evaluation, fire fighting fixed system, soil contamination evaluation, water treatment projects and occupational hygiene an safety standards.

Petrobras, Cenpes

PETROBRAS or Petróleo Brasileiro S.A. is a semi-public Brazilian multinational energy corporation headquartered in Rio de Janeiro, Brazil. It is the largest company in the Southern Hemisphere by market capitalization and the largest in Latin America measured by 2011 revenues.

Magdeburg 18/04/2019 _____

Vitor gabriel silva

(*Online version of this resume*)